5-2022

# Optimizing Aqueous Processing of Nickel-Rich Cathode Material in Ultra-Thick Lithium-Ion Batteries

Alexander J. Kukay
*University of Tennessee, Knoxville*, akukay1@vols.utk.edu

To the Graduate Council:

I am submitting herewith a dissertation written by Alexander J. Kukay entitled "Optimizing Aqueous Processing of Nickel-Rich Cathode Material in Ultra-Thick Lithium-Ion Batteries." I have examined the final electronic copy of this dissertation for form and content and recommend that it be accepted in partial fulfillment of the requirements for the degree of Doctor of Philosophy, with a major in Energy Science and Engineering.

Jianlin Li, Major Professor

We have read this dissertation and recommend its acceptance:

David L. Wood III, Thomas A. Zawodzinski, Joshua Sangoro

Accepted for the Council:

Dixie L. Thompson

Vice Provost and Dean of the Graduate School

(Original signatures are on file with official student records.)

# Optimizing Aqueous Processing of Nickel-Rich Cathode Material in Ultra-Thick Lithium-Ion Batteries

**A Dissertation Presented for the**
**Doctor of Philosophy**
**Degree**
**The University of Tennessee, Knoxville**

**Alexander J. Kukay**
**May 2022**

# DEDICATION

I dedicate this work to my family, for all their support in all of its forms.

Thank you, I am immeasurably indebted to all of you.

# ACKNOWLEDGEMENTS

I must first thank my parents and their constant support during my academic career. Their support has meant the world. I would also like to specifically thank Mary Gomoll, Theresa Kidder, and Andrea Hearden, for recognizing and fostering an appreciation for science long before I could recognize it in myself. For this I am eternally grateful. I also thank the entirety of the Department of Physics and Astronomy at the University of Wisconsin-Eau Claire. Without the support and encouragement I received during my undergraduate studies and beyond from whom I now consider dear friends, I certainly would not have found myself here. I would also like to thank Allie Burns for all of the assistance she has provided throughout this process, her help cannot be understated.

I want to express my appreciation for the members of my committee as they have provided a substantial amount of guidance during my time at ORNL. Specifically, I would like to thank Dr. David L. Wood III and Dr. Jianlin Li for their flexibility and understanding throughout a global pandemic and a lengthy and disruptive laboratory renovation. Many scientists who have passed through the BMF at ORNL also deserve my sincere thanks. These include Dr. Rose E. Ruther, Dr. Zhijia Du, Dr. Kevin Hays, Dr. Marissa Wood, Dr. Lamuel David, Dr. Chengyu Mao, Dr. Yangping Sheng, Dr. Seong Jin An, Dr. Claus Daniel, Dr. Ritu Sahore, Dr. Linxiao Geng, Dr. Erin Creel, Dr. W. Blake Hawley, Dr. Mengya Li, Kelsey Livingston, Andrew Todd, Dr. Charl Jafta, Dr. Yaocai Bai, Dr. Georgios Polyzos, Emily Bott, Dr. Anand Parejiya, and Dr. Dhrupad Parikh. Their

encouragement and friendship have been paramount, thank you. I would also like to add a special thank you to Jason R. Kukay for last minute chemical engineering crash course.

Most importantly, I must thank the love of my life, Angie Walker, for her constant support and companionship as we completed our degrees together. I can only fail to express in words how important you are to me and how special these past few years have been. Without your love and support the following material would not be possible. Thank you from the bottom of my heart for sharing this experience, and so many more, with me. I am truly humbled.

# ABSTRACT

Lithium-ion batteries (LIBs) have been an instrumental technology since their commercialization in the 1990s. Although much progress has been made in terms of cost and efficiency of production, several challenges remain. Notably, as LIB technology continues to be applied to the transportation sector for electrified mobility in the form of electric vehicles, the question of production ethics and environmental sustainability becomes paramount. The aim of this dissertation is to address some of these concerns in the form of cathode processing techniques.

This dissertation focuses on optimization of aqueous processing applied to cathode active materials. First, a study demonstrating the feasibility of aqueous processing for ultra-thick nickel-rich cathode active material via phosphoric acid addition shows both mechanical and electrochemical improvements in aqueous processed full cells. This study is then expanded upon by pursuing structured cathode designs for improved high-rate discharge capacity in ultra-thick cathodes. An improved cathode structure is identified and shown to not only be mechanically robust but also improve the material utilization and ionic resistance of the electrode. Next, drying mechanics of aqueous cathodes are investigated in a comparative study focused on the first stage of coating drying. A 10X increase in drying rate is identified and benefits are discussed. Finally, polymer electrolytes and the potential of benign processing applied to solid-state LIBs is explored. Mechanical and electrochemical performance to baseline compositions is investigated and discussed.

# TABLE OF CONTENTS

# LIST OF TABLES

# LIST OF FIGURES

# INTRODUCTION

## Background

Lithium-ion batteries (LIBs) have become a crucial component of everyday tasks and have become an integral part of energy storage since their market introduction. [1] Improvements in technology and materials have allowed for many formats and targeted applications of LIBs in any number of industries. However, technology surrounding LIBs still has considerable room to improve. [2] From both production and application perspectives, LIBs are far from optimized and can benefit from process optimization as well as improved materials chemistry.

One of the most crucial applications of current LIB technology is within the transportation sector, specifically electrification of mobility. Transitioning from petroleum-based fuels for vehicles to electric cars is currently in progress but still has a considerable gap between current state of the art and widespread consumer adoption. With all new (2021 model year) electric cars having an average range of less than 250 miles (combined) yet costing an average of $54,758, the economic viability of these vehicles must improve in order to increase market adoption. [3] Considering the median household income in the United State in 2020 was $67,521, the price tag of a luxury electric automobile is far beyond the purchase power of the average American. [4] Making strides to reduce both the cost of electrified mobility as well as provide longer range to meet the concerns of range anxiety in new customers, alternative strategies are required.

With increased emphasis on automotive applications and support from the current Presidential Administration, the state of the art of lithium-ion secondary batteries is not sufficient to reach the ambitious goals laid out by President Biden in his climate agenda. However, with appropriate focus LIBs can play a key role in reducing dependance on fossil fuels and lead to a much more environmentally friendly transportation sector. [5] In order to advance the climate agenda by transitioning to electric vehicles, LIB technology must become safer, more cost effective, and closer in range performance to internal combustion engines (ICE) they are meant to replace. The manufacturing process also must be improved to reduce the global warming potential (GWP) as it has been estimated that production of an EV produces roughly double the GWP of a comparable ICE, eliminating the potential climate benefit of transitioning away from fossil fuels. [6]

Four main areas of interest are identified as problems to address in current LIB production and potential solutions are provided. These four areas of interest are energy density of the battery pack, materials and production cost, environmental impact of production, and operational safety. These issues are centered around the drive to increase energy density while simultaneously decreasing production cost. Elevating the environmental concerns associated with LIB production is also a topic of interest and provided additional justification for various project goals. These issues are approached via multiple in-depth investigations that are presented as chapters in this document.

**Improving Energy Density**

Over the past 13 years the energy density and associated cost LIB packs has fallen from over $1000/kWh with energy density of only 55 Wh/L to $197/kWh with energy density of 250 Wh/L. This 5X reduction in cost paired with an almost 5X increase in energy density improved the viability of commercially available electric vehicles that have the potential to replace ICEs without the need for policy incentives. However, as the DoE has provided an ultimate energy density target of >350 Wh/L and cost target of $60/kWh, there is a substantial amount of optimization to be done. [7]

One way to increase energy density while simultaneously reducing cost is to remove inactive components from the cell assembly. LIB cells are comprised of a container to house the internal chemistry, substrates commonly referred to as current collectors that support the electrode material, a separator that prevents physical and electrical contact between the electrodes, and electrolyte that provides ionic mobility throughout each electrode. Furthermore, each electrode is a composite that includes the active material, typically graphite for the anode material and a layered transition metal oxide for the cathode, a conductive additive to enhance electronic conduction throughout the electrode, and a polymetric binder that keeps the electrode both mechanical intact and able to withstand some degree of deformation. This mechanical expansion and contraction is experienced during lithiation and de-lithiation associated with ion transport between the electrodes. Among all of the listed components of a LIB, only one material in each electrode is considered active, and the rest of the materials are used to enhance the

performance or allow the function of the cell as a whole. Increasing the energy density of the cell focuses on increasing this ratio of active to inactive materials.

One way of increasing the ratio of active material to inactive material practically involves increasing the thickness of each electrode while maintaining the same percentage of active material. This then increases the theoretical capacity per electrode layer and reduces the total number of layers needed to achieve the desired cell capacity. As the number or layers is reduced, the number of current collectors and separators is also reduced. As the current collector and separator do not contribute to the overall capacity of the cell, the energy density is increased without having to make chemical or material improvements.

Although this technique is straightforward, there are real limitations as the available capacity of an electrode decreases with thickness due to mass transport limitations and thick electrode tend to suffer from inhomogeneous binder distribution developed during drying. Optimizing this technique is the major focus of Chapters 3 and 4. Introducing first a chemical additive to achieve a mechanically stable ultra-thick electrode, followed by implementing a structured design in an attempt to increase active material utilization by optimizing the lithium-ion diffusion pathway.

## Materials and Production Cost

Cost of LIB packs has decreased substantially since their market introduction and are now the energy storage option of choice for most applications. The cost of the cell however is still too high for economically viable electric vehicles that are capable of replacing the majority of ICE vehicles on the road today or forecast to be on the road in the near future. As nations continue to develop the need for mobility is only increasing and the demand for both ICEs and EVs is projected to increase dramatically. [8, 9] Batteries are the main reason for EVs added expense when compared to their ICE counterparts, thus the need for cost reduction is clear. [9] By investigating lower cost materials and production techniques, the overall cost of the cell can be reduced. Namely by moving from the typical solvent currently used in industrial settings, NMP, toward benign solvents such as water, the estimated cost reduction is substantial as the material cost is lowered, the drying time and energy requirements are reduced, and the need for solvent capture is eliminated. [10] This technique is highly optimized for anode processing but has encountered challenges when applied to nickel-rich cathodes due to excess lithium driving the slurry pH beyond the stability window for aluminum. Investigated in Chapter 1 is the benefits and challenges of aqueous processing as applied to cathodes. Presented in Chapter 3 is a technique involving addition of a mild acid as a pH modifier to abate the corrosion reaction observed during cathode aqueous processing. Solvent effect on drying time and resulting binder distribution is investigated in Chapter 5.

**Environmental Impact**

Along with operational safety, environmental impact is driving advancements in LIB technology toward a more sustainable and equitable outlook. A large focus within the battery manufacturing industry is elimination of toxic or harmful constituents. As such, development of replacements for a major processing solvent, N-methyl-2-pyrrolidone (NMP), have driven the practice of aqueous processing within the battery field. Replacing NMP, which is a controlled volatile organic compound (VOC) with water as a processing solvent has the potential to improve the environmental efficacy as well as reduce processing costs for new battery materials. [11, 12] Although aqueous processing has been successful in negative electrode processing, applying this technique to positive electrode manufacturing has proven to be a difficult task due to interfacial stability issues between the cathode active material and water. [13-16] Elimination of NMP based production processes can also help achieve the Department of Energy (DoE) Vehicle Technologies Office (VTO) cost target of $60/kWh by reducing material and drying cost. [7, 10, 12]

With a forecast surge in battery production, one major aspect that must be considered is efficient and environmentally friendly production practices, epically when considering the geographical locations of major battery production operations. [9, 17] Of particular interest is procurement of raw materials as there exists a finite amount of critical materials such as lithium and cobalt. If the projected increase from 750 million to 2 billion vehicles by 2050 is accurate, the implications this massive increase in demand for mobility will have on raw

materials is drastic. [8] In order to avoid shifting the problem of greenhouse gas (GHG) generation in the current mobility sector from use phase to production phase, the materials used as well as the current manufacturing processes must see significant improvement.

Various life cycle assessment (LCA) studies have been published with the goal of identifying manufacturing and use optimization opportunities. [17-19] As each study explores the total impact of an electrochemical cell, one shared conclusion is the lack of primary data sources in the materials production process that hinders a full characterization and comparison of different cell configurations. [18] Even with lacking primary data, it is clear from various LCA reports that improvements must be made with respect to both materials cost and processing efficiency if electric vehicles are to replace ICEs and produce a positive climate impact.

Environmental and material costs concerns are discussed further in Chapter 1 where arguments for aqueous processing are developed and advancements in the field are summarized. This first chapter is meant to inform Chapters 3, 4 and 5 which investigate the mechanical and electrochemical implications of utilizing NMP free processing techniques for electrode production.

**Improving the State of the Art**

The state of the art of LIBs continues to evolve and as such it has become clear the direction of future investment will heavily favor solid state electrolytes in order to reduce risks associated with liquid electrolytes. As liquid electrolytes have drawn increased scrutiny for their potential to cause fire events up failure, solid state technology has seen a resurgence, focusing on both solid garnet type electrolytes as well as flexible polymer formulations. An in-depth discussion on the future of solid-state electrolytes and their production and application to electric vehicles is provided in Chapter 6 and an investigation into aqueous processing and composition optimization for polymer type electrolytes is given in Chapter 7. These chapters are intended to provide a foundation for future work while promoting the use of renewable and environmentally benign materials.

# CHAPTER I
# REVIEW ON AQUEOUS PROCESSING

## ABSTRACT

Aqueous processing of electrode material has the potential to reduce cost and decrease environmental impact of current lithium-ion battery (LIB) manufacturing techniques. Replacing expensive and volatile binder solvents, such as N-methyl-2-pyrrolidone (NMP), with aqueous processing utilizing deionized (DI) water not only reduces material cost but also reduces processing and capital equipment costs by eliminating the need for solvent capture and recovery. Processing of anode slurries using DI water as the solvent have been widely successful and are now common in industrial settings. Aqueous processing of cathode slurries however has posed greater challenges mainly due to lithium leaching from active materials and subsequent corrosion of the current collector. Successful benchtop or pilot scale aqueous processing with some nickel-based cathode materials has been demonstrated, but industrial implementation remains elusive. This work is focused on the motivations and advancements of aqueous based processing and the associated benefits for both equipment cost and environmental stewardship.

## Importance of Aqueous Processing

Lithium-ion batteries (LIBs) have experienced a wealth of innovation since their commercialization in the 1990's. From development of novel materials to optimization of manufacturing processes, the LIB has improved substantially over the past few decades. This massive improvement has allowed the technology to become an integral part of daily life and a viable solution to various energy related crisis. [1] As energy demands increase and environmental concerns become more critical, LIBs are an excellent alternative to fossil fuel consumption, especially when applied in vehicle technology. The Department of Energy (DoE) Vehicle Technologies Office has set cost and energy density targets, currently $60/kWh and >350 Wh/kg respectively. [7] Meeting these targets will require major advances in materials and manufacturing techniques. Meeting the goals set by the DoE would result in a vehicle that would be cost competitive with an internal combustion engine (ICE) counterpart and provide a range similar to that of an ICE. [20] With materials cost comprising 70 – 80% of overall cell cost, realizing this DoE goal will require utilizing more cost effective and higher energy materials as well as developing production techniques that streamline cell processing. [21, 22] This review seeks to outline major challenges and advancements in the field of lithium-ion battery production centered around aqueous processing techniques.

Advancements have already been made in numerous areas, including development of higher energy, ethically sourced active materials such as $LiNi_xMn_yCo_zO_2$, $x \geq 0.8, z \leq 0.1$ (NMC 811) and optimization of the preliminary charging protocol, referred to as formation

cycling, to reduce the amount of time and associated energy costs of preparing batteries for market. [23] Employing active materials with a higher practical capacity and larger electrochemical operation range result in a more energy dense, cost-effective battery. The added benefit of reducing the amount of cobalt used results in a more ethical battery by reducing the adverse humanitarian effects cobalt is associated with. Cobalt free materials are also under consideration but as of yet still experience reduction at high voltage that limits their practicality. [24] Steps such as the addition of silicon to graphite anodes have also increased the energy density of the resulting cell by optimizing the mixture of high theoretical capacity, yet mechanically problematic, silicon to relatively low theoretical capacity graphite. Silicon provides a very desirable theoretical capacity in excess of 3579 mAh/g, but full lithiation of the material leads to a 280% increase in volume, resulting in poor capacity retention due to structural damage from cycling. [25, 26]

Of these many techniques and material that have been pursued in the drive to develop more environmentally responsible and cost-effective techniques, aqueous processing has become an area of increased research interest, in part due to its environmental benefits. [1, 12, 27] Aqueous processing involves removing the toxic volatile organic compound (VOC) typically used in electrode processing, N-methyl-2-pyrrolidone (NMP), using deionized water (DI water) as a solvent in its place. NMP is used in order to disperse the common electrode binder Polyvinylidene fluoride (PVDF), which is not soluble in water, but provides exceptional mechanical and electrochemical performance. PVDF is electrochemically stable within the potential window of LIBs and has good mechanical

properties, facilitating the expansion and contraction of the electrode during cycling. [28] However PVDF is a fluorine containing compound that could potentially generate LiF upon reaction with lithiated graphite, an endothermic reaction that could contribute to thermal runaway. [29-32] Even with the proven performance of NMP and PVDF, the cost and environmental benefits of aqueous processing make the endeavor an attractive alternative.

Replacing the solvent is not trivial as solvent and binder have a pronounced impact on the entire electrode production process. From changes in the dispersion rheology and stability, to chemical reactions driven by active material instability, solvent choice impacts the electrode production process deeply. Accordingly, determining a suitable binder composition for aqueous electrodes has attracted a large amount of attention in recent years. [16, 26, 33-36] In the case of graphite anodes, many of these problems have been solved, resulting in successful industrial implementation.

Aqueous processing of electrode materials is also beneficial to the emerging field of battery waste recycling. [37] As the market share of LIBs increases, so does the waste potential. Effective recycling techniques can reduce overall waste and defray new material cost by reusing spent electrode material. Typical recycling process require an organic solvent, NMP or N, N-dimethylformamide (DMF) to dissolve the PVDF and recover active material. Both NMP and DMF are now restricted substances due to their toxic nature and potential to cause reproductive harm. [11, 38, 39] Both of these solvents can be avoided by

utilizing DI water as the solvent and avoiding PVDF as a binding material. This could potentially create a more attractive recycling market and result in an increase in the reuse of critical battery materials.

## Electrode Processing Steps

Electrode processing has become a large focus of LIB production as much of the cost associated with the ultimate battery pack is generated during the materials processing step. [40] The field of electrode manufacturing has been highly active, seeking to optimize each step in the overall process. [41] Studies have addressed topics from temperature of slurry mixing, to coating speed and technique, and mixing method and component addition. [2, 42-46] Introduced here are the typical processing steps involved in the production of LIB electrodes and their associated importance from a performance and cost viewpoint.

### *Material Preparation and Mixing*

The typical process for producing commercial LIBs begins with mixing of active material, conductive additives, binders, solvent, and sometimes includes additives for specific purposes. [14, 47-50] After each component is thoroughly mixed, the homogenous mixture is commonly referred to as a slurry. Slurry mixing protocol and composition varies widely depending on a variety of factors, but generally involves a lengthy mixing process and a

degassing period to remove air bubbles before preceding to coating. Examples of electrode mixing typically vary by scale, ranging from benchtop agitators and sonicators to industrially sized planetary mixers. As a result, the cost associated with mixing is highly dependent on the mixing method and equipment. NMP based slurries are typically comprised of less than 45% solids in order to maintain acceptable coatability, aqueous dispersion can contain an solid contents in excess of 60%. [51] The mixing method of choice therefore must accommodate the added agglomeration potential that accompanies this increase in solids material.

***Electrode Coating***

The most common coating technique adopted by industry is slot-die coating. Slot die coating utilizes a moveable coating head and rotor that extrudes a consistent bead of slurry onto a moving substrate, creating a continuous uniform sheet. [52] This process is easily adopted to operate in a roll-to-roll regime and by varying the pump speed, line speed, and coating gap, a wide variety of slurries are compatible with this technique. This technique has a multitude of advantages such as easy scalability and ability to be accurately modeled by solving the two dimensional Navier-Stokes equation. [53, 54] Although the coating system has clear advantages, there do exist limitations. In order to produce a uniform and consistent electrode, the slurry used must conform to some basic requirements. The dispersion must balance forces from an applied vacuum, drag of the current collector, and pressure of the feed in order to reside within the *coatability window*. [46, 52] Along with

these fluid forces, the speed of the current collector, coating velocity, as well as the distance from the current collector to the slot die head, coating gap, are critical factors in the quality of the coating. As a result, the physics and fluid mechanics of slot die coating are heavily studied with the ultimate goal of coating the most solids dense slurry possible while avoiding defects such as rivulets, ribbons, or streaks. [46, 52]

Other techniques such as doctor blade coatings are common for research and benchtop scale electrode production as the required amount of material is considerably lower. Ink jet and additive manufacturing inspired deposition techniques have also been proposed, but are not the focus of the current work as they have yet to be demonstrated as industrially viable or cost competitive with slot-die coating. [55-57]

***Drying and Calendering***

After coating, the substrate and newly coated slurry are then dried, typically in an enclosed oven operating at elevated temperature. In a roll-to-roll regime, this is often a component of the greater slot-die coater itself. At this stage it may be necessary to recapture solvent, for example NMP if it has been used as the primary solvent. [58] The drying process is one of the more costly and energy intensive processes involved in LIB production and subsequently garners a large amount of research interest. [10, 59] An in-depth explanation of challenges associated with electrode drying is presented in a future section. After drying the coating is then referred to as an electrode. Porosity, or more generally tortuosity, have

proven to be important factors in electrochemical performance of many electrode architectures, and accordingly electrodes are commonly subjected to an additional calendering step to optimize these parameters. [60-64] Electrodes are calendered by applying a force normal to the current collector in a controlled manner, thus compacting the electrode structure to the defined amount of void space. This void space facilitates the electrolyte and subsequent charge transfer and ion diffusion throughout the electrode.

### *Cell Assembly and Formation Cycling*

After calendering, electrodes are punched to the desired geometry and subjected to secondary drying before final assembly to remove any excess moisture that may react with the organic electrolyte upon cycling. [65] Depending on the geometry, affixing tabs to the cell varies, but generally some form of tab attachment occurs in order to provide a sealed electrical connection. Commonly tabs of compatible metals are ultrasonically welded in order to provide intimate contact without risk of mechanical damage. Conventional lithium-ion cells that utilize a liquid electrolyte are assembled with a separator material between opposing electrodes, this material is a porous polymer highly engineered for the application. This separator material has been the focus of past research and as a result is highly optimized for ionic transfer while eliminating electrical conduction between the opposing electrodes. [1, 63, 66]

Cells are then filled with electrolyte before vacuum sealing the system. Depending on the formulation and manufacturer, differing protocols may be employed, but generally some form of formation cycling is required to establish a stable solid electrolyte interphase (SEI) before the cells are ready for commercial use. Formation cycling alone accounts for anywhere from 10 – 100 hours, meaning a large footprint and energy demand are needed to manufacture cells commercially. [67] Formation cycling has been shown to add substantial cost to the overall battery system through increased lab space and time-consuming cycling protocols, consequently research focused on reducing this processing step is abundant. [23, 68-70]

## Cost Savings from Drying Equipment

Transitioning rom the typical solvent NMP to aqueous based methods not only provide an economic benefit associated with the material cost, but also can enable economically favorable drying parameters and techniques. Materials cost savings is driven primarily by the reduction in need for capital equipment and solvent recovery cost but is also directly attributed to the lower price of the replacement materials. NMP is more than an order of magnitude more expensive than water, \$1.25 $L^{-1}$ for NMP compared to \$0.015 $L^{-1}$ for DI water. [12] This cost reduction is also present when considering replacement binder materials, many of the replacement materials are cheaper than the industry standard PVDF. For example, the cost of PVDF is approximately \$20 $kg^{-1}$ as compared to CMC, a potential replacement binder, which costs approximately \$2-3 $kg^{-1}$, an order of magnitude cost

reduction. [33, 71] Savings associated with drying parameters can also be realized due to the differences in vapor pressure and boiling point, 1.0 mm Hg at 40 °C and 204.3 °C for NMP and 55.3 mm Hg and 100 °C for water respectively, the energy input and associated with drying can be reduced by 25.7%. [10] Other studies have shown a 2X reduction in drying cost can be expected by implementing aqueous processing, if a production capability of 100,000 10 kWh battery packs is achieved. [10] However, since drying only accounts for an estimated 8-9% of total pack cost in this scenario, the major source of cost reduction resides in capital equipment costs. Without the requirement to recover NMP during the drying process, the complex solvent recovery system can be omitted, resulting in $3-6 M in equipment cost savings. [10] Cost savings could also be realized in the form of siting and permitting cost reduction due to elimination of VOCs. [10, 72]

## Need for New Binding Materials

Removal of NMP in favor of aqueous processing requires finding a new binder to use in electrode production as PVDF is not water soluble but only soluble in some select organic solvents. [73] Binders are an integral part of electrode composition and must be carefully considered as they play a key role in battery performance. [74] Potential binders must satisfy multiple criteria in order to be an effective and viable alternative. First a binder must satisfy the basic requirement of adhering the active and inactive materials to the current collector and creating a continuous electrode, adhesion and cohesion respectively. [27, 41, 71] The binder must also accommodate the electrodes expansion and contraction cycles

during the electrochemical transfer or lithium-ions and therefore be mechanical robust under various strain conditions. This expansion can be in excess of a 10% volumetric change in the electrode (standard graphite anode) and in some cases much greater (280% for a graphite/silicon composite anode). [33, 75] Along with being mechanically stable throughout repeated charge/discharge cycles, the binder must also be stable throughout the entire electrochemical range of the cell (typically 0 V to 5 V $Li/Li^+$) and also stable against the other materials in the cell formulation. [71]

Although a binder generally does not need to be charge conducting, the proportion of binder should be minimized especially if the material is insulating in nature. Some efforts have been made recently to use the binder not only as a means of maintaining the electrode structure, but to also improve conductivity throughout the electrode by contributing to ion transport. [76] A good candidate for a new binder material should also avoid environmentally hazardous components, such as fluorine, in order to eliminate hazard control or environmental safety concerns. A number of candidate binders have been researched as suitable replacements for industry standard PVDF, including styrene butadiene rubber (SBR), carboxymethyl cellulose (CMC), xanthan gum, poly-acrylic acid (and its derivatives), as well as others. [26, 33, 71, 75] An overview of recent developments concerning electrode binders are given for both anode and cathode formulations.

***Anode Compositions***

Graphite and silicon remain the preferred electrode materials for anodes due to their relative abundance and attractive gravimetric capacities, 372 mAh/g and 3579 mAh/g respectively. [74, 75] Although lithium metal anodes are of great interest, the numerous challenges presented by a full metal anode limit their use and practicality and thus are not within the scope of this work. [77-83] PVDF has long been the ideal binder for use with graphite as the interaction between PVDF crystals and the carbon surface in the form of a strong C – F bond result in high electrode durability while still being able to accommodate small volumetric changes during cycling. [74, 84] With the inclusion of silicon as an anode active material, PVDF is no longer an ideal binder candidate as the lithium-silicon alloying reaction produces $Li_{15}Si_4$, resulting in upwards of 280% electrode expansion and subsequent electrode fracturing. [26, 75] This poses an issue even for small percentages of silicon in graphite anodes. In response, binders with high carboxylic acid or hydroxyl groups have been investigated as these can lead to surface modification of graphite that increases the number of available binding sites. [85, 86]

Such binders include PAA and LiPAA. Hays and coworkers presented a direct comparison of PAA and LiPAA processed in NMP and water respectively. They found PAA processed with NMP leads to ~3.5X more residual water in the anode as compared to LiPAA processed in water. [75] The authors point to the fact that PAA is a superabsorbent of water, subjecting electrodes with PAA to elevated drying temperatures above 140 ℃ lead to

decreased cell performance. Hays and coworkers associate this poor performance with the dehydration of carboxylic acid groups which react with each other to form an anhydride and water. [75] Their work continues to show the advantages of LiPAA compared to PAA in silicon containing graphite anodes. This is largely due to the thermal and electrochemically stability of LiPAA as compared to PAA, resulting in a better electrochemical and mechanical performance. [75] Poly(3,4-ethylendioxythiophene) has also been investigated as a possible binder material because it is ionically conductive, leading to an expanded conduction network, but is considerably more expensive than other binder options ($8.64/mL). [33]

Out of many promising candidates, sodium substituted CMC has become a widely used binder for aqueous processing techniques due to its ease of production, environmentally benign nature, and superior mechanical and electrochemical stability. [87, 88] CMC is not new to the battery industry, cellulose based materials have long been used in combination with other additives in lead-acid, nickel cadmium, and nickel metal hydride batteries as well as LIBs, although not always as a binder. [87, 89] Notably, CMC has been relied upon to stabilize the naturally hydrophobic graphite particles in aqueous solutions in combination with SBR, a technique that is now common in industry. [89] In a direct comparison to NMP based anodes, CMC processed anodes were able to provide similar performance with a lower weight percentage, 10% PVDF compared to 5% CMC. These anodes did however exhibit a higher first cycle capacity loss, but show diminished capacity fade per cycle, attributed to a fast-forming SEI layer that is generated by the reactivity of

CMC (mainly the present hydroxyl groups) with electrolyte. [90] This reaction results in a uniform and stable SEI layer that slows the continued capacity fade observed in systems with unstable SEI layers resulting in electrolyte consumption. [74, 91] Similar cycling behavior was displayed for samples with 10% PVDF, 5% CMC and 5%/1% SBR/CMC but using SBR alone did not result in a mechanically robust electrode. [26] Other studies put the minimum amount of CMC required at 2 wt%, this investigation did not however provide long term cycling to demonstrate effects from degradation. [87] It was demonstrated that a combination of SBR and CMC not only performed as well as PVDF based electrodes, but the amount of binder required was reduced considerably, thus leading to an increase in energy density. [26] Although both mechanically and electrochemically stable, CMC does present unique challenges that require special consideration during implementation. For example, CMC is more hydrophilic than PVDF and absorbs water during the slurry processing steps. This results in a large fraction of remaining solvent, even after preliminary drying and necessitates a secondary drying step to ensure a sufficiently dry electrode and avoid a reduction in cycle life and hydrofluoric acid production associated with high water content in the electrode. [10] This added drying time could potentially offset any energy reduction realized by transitioning to aqueous processing. It has also been reported that the adhesion strength of CMC is one whole order of magnitude lower that comparable SBR or PVDF binders, leading to concerns about longevity during repeated lithiation and de-lithiation expansion cycles. [92]

In order to improve adhesion of CMC based binders, SBR or the acrylate JSR binders can be added in conjunction with CMC to form a composite binder, a practice which has seen great success for anodes (SBR) and cathodes (JSR). A more detailed discussion on the merits and challenges of adding JSR is provided in the next subsection.

***Cathode Compositions***

Investigations into binder replacements for positive electrodes are not as prominent as negative electrode investigations due to existing challenges for positive electrode aqueous processing outlined in a future section. As the field of positive electrode processing has grown, it has leveraged many the lessons learned from negative electrode processing and has had the benefit of being able to utilize materials developed for graphite anodes with slight modifications. The most prominent example of such is the utilization of CMC binder for positive electrodes with the addition of JSR TRD202A (JSR) to form a composite binder capable of withstanding the high voltage applications of new nickel rich materials (in excess of 4.6 V). [14, 15, 93] JSR has the added benefit of improving mechanical adhesion and cohesion and performs a similar function in the cathode as SBR does in the anode. [94] Direct comparison to PVDF based cells show improved electrochemical performance in NMC based cathodes while reducing the binder percentage from 8 wt% for PVDF to only 3-6 wt% for CMC JSR composite binder. [94] In a similar study, the JSR CMC composite binder was shown to lead to improved long-term cycling stability as compared to the typical PVDF. [93] Although JSR has proven to improve the mechanical

and electrical properties of aqueous processed cathodes, it is a fluorinated acrylic latex and has the unfortunate consequence of adding fluorine back into the electrode system leading to a complicated recycling process and potential contamination in the event of a cell rupture. Compared to similarly fluorinated PVDF, JSR does show improved thermal stability suggesting it may be safer in the event of a fire event. [94]

As the practice of aqueous processing of positive electrodes grows, the continued investigations into novel binders will become more numerous. Until that time, the use of CMC and JSR composite binders will likely continue to be the standard practice as it provides numerous benefits with minimal downside.

## Electrode Drying and Binder Migration

Along with challenges in binder selection, electrode drying mechanics not only have an impact on the formation of the porous electrode network but can also impact the binder distribution and subsequently the mechanical properties of the electrode. Electrode drying is not only a critical step in LIB production from an economic standpoint but has also been shown to directly affect the mechanical and electrochemical properties of the resulting cell. [10, 95-101] Drying parameters can have a large impact on the resulting distribution of active material, conductive additive, and polymetric binder as the solvent is removed from the electrode structure. As typical electrode thickness is on the order of hundreds of microns thick but upwards of hundreds of square centimeters or above in area, they can be

accurately treated as thin films and are appropriately modeled as such. [102] Drying can be modeled via two distinct drying regimes. First, the larger active material particles consolidate as the solvent is removed and begin to form the eventual electrode structure. As the particles consolidate, they eventually reach a maximum density and thus are no longer able to move, this stage is commonly referred to as *film shrinkage*. Once enough solvent has been removed such that the porous electrode network is mostly established, the second phase of drying begins, *pore emptying*. This stage involved excess solvent being removed from the pores formed in the previous stage. This includes not only the through pores that have been developed, but also the closed pores that have trapped solvent. [101] This second stage accounts for the bulk of the drying time and energy input throughout the drying process and consequently, is an area of interest for cost optimization. [2, 10]

As the *film shrinkage* and *pore emptying* stages of drying proceed, all of the constituent particles experience competing forces from sedimentation, diffusion, and thermal Brownian motion. As the larger active material particles begin to settle and form the pore structure of the resulting electrode, the smaller conductive additive and polymetric binder particles experience forces from evaporation at the film surface and Brownian diffusion resulting in a competition between diffusion and capillary action within the electrode structure. If the drying rate is sufficiently high, the capillary action driven by surface evaporation dominates the thermal diffusion forces and results in a concentration gradient for the binder and conductive additive. This resulting binder gradient is key to the eventual electrode performance from both a mechanical and electrochemical standpoint. A non-

uniform distribution of binder throughout the electrodes directly leads to adhesion issues as well as conduction issues due to the insulating nature of commonly used electrode binders. [100]

Not only is binder migration a function of drying conditions but is also dependent on solvent. Even with the important role of solvent and drying in electrode production evident, there is little research addressing the combination of factors directly. A significant amount of research has explored electrode drying in depth and multiple models have been developed to aid in the optimization of solvent removal from both anode and cathode formulations. [35, 59, 101-105] However, these investigations rarely consider the differences and advantages of solvent replacement with regard to electrode drying and binder distribution. As aqueous processing for graphite anodes has become more common, multiple studies address investigation and optimization of aqueous processed graphite anodes, however few studies involve aqueous processed cathode material. [15, 92, 99, 101, 106, 107] Fewer yet are studies that directly compare NMP and DI water and the optimal drying parameters for each solvent.

As previously discussed, the optimization of drying parameters also has concrete economic advantages. [10, 12, 72] If these advantages can be realized, the overall cell production process can be simplified, and the overall battery pack cost can be reduced.

## Current Collector Corrosion and Active Material Instability

Although anode chemistries have proven to be commercially viable with aqueous processing techniques, cathode chemistries have not shared the promising outlook. Some cathode materials, particularly LMNO and NMC based materials, have demonstrated corrosion at the current collector interface and subsequently poor adhesion. This reaction is driven by excess lithium within the active material leaching into solution via a well described proton exchange reaction giving in Equation 1-Equation 4. [13-15] This reaction results in lithium hydroxide and lithium carbonate being present in the slurry resulting in increased slurry pH above 11. Not only is aluminum, the preferred choice of positive electrode current collector, only stable at pH between 4.5 and 8.5, the lack of stability with the aluminum oxide layer results in a corrosion reaction at the interface which generates hydrogen gas. [28, 34] This gas accumulates in the form of bubbles and eventually releases from the current collector and travels the thickness of the electrode to reach the electrode surface. This gaseous transport both disrupts the electrode structure during the drying process and impacts the binding between the drying slurry and current collector. [108, 109] In addition to the lack of adhesion, surface cracking resulting in un-useable electrodes have been widely reported and are a side effect of the hydrogen gas generation. [15]

Equation 1: $$\boldsymbol{Li^{+} + H_2O \rightleftharpoons LiOH + H^{+}}$$

Equation 2: $$LiOH + CO_2 \rightleftharpoons LiHCO_3$$

Equation 3: $$LiOH + LiHCO_3 + CO_2 \rightleftharpoons H_2O + Li_2CO_3$$

Equation 4: $$Al + OH^- + 3H_2O \rightarrow Al(OH)^-_4[s] + 3/2H_2[g]$$

Surface stability is critical to ensure surface adhesion and mechanical stability during production and long-term cycling. Various techniques have been developed in order to abate or avoid undesired reactions at the current collector interface. These techniques include applying a carbon coating before coating, preventing contact between the alkaline slurry and aluminum surface, adding mild acids, such as phosphoric acid, to slurry to bias the pH back within the stability window of aluminum, and chemically applied coatings that suppress the reaction mechanism by providing a stable buffer layer between the solvent and active material particle. [14, 28, 34, 47, 108, 110-112] Although all of the above-mentioned techniques have been shown to effectively mitigate the corrosion reaction, the incurred cost and technical difficulty of techniques such as atomic layer deposition of a thin carbon coating not only add additional material and processing steps but also introduce an additional interface between the electrode and current collector. These side effects increase the time and cost of production and introduce an additional non-electrochemically active interface between the current collector and electrode, potentially increasing the impedance of the electrode as well as reducing the overall cell energy density. [113, 114]

There is also evidence to suggest some additives can form protective coatings on the active material particle during cycling, acting as a protective barrier from the processing solvent. [28, 47, 114] What remains unclear is the role of these protective coatings in terms of charge transfer resistance between ions in the electrolyte and the active material particles themselves. The stability of these layers are also an important consideration as an unstable cathode interphase layer (CEI) can lead to increased electrolyte consumption and subsequent capacity fade and insufficient discharge capacity at high cycle rates. [115]

The role of the current collector in the corrosion reaction has also been addressed on multiple occasions and it has been shown that replacing the aluminum current collector with a copper counterpart does not entirely solve the cracking issue. This result demonstrates that the current collector is not the only source of cracking, elucidating the role of capillary stress, agglomeration, binder distribution as potential causes of surface cracks. [15] This will be discussed further in the next section. Mitigating the corrosion reaching and subsequent hydrogen gas generation does however eliminate the most sever cracks observed in thick cathodes (5-8 $mAh/cm^2$). [14, 15]

## Surface Tension and Induced Cracking

Aqueous processing, especially with large areal loadings (exceeding 4 mAh/cm2), can lead to crack formations in the electrodes during the drying process. [48] Small surface cracking is commonly observed at the electrode interface and can usually be mended through the

calendering process. For aqueous processed electrodes, there exist both these smaller cracks as well as the potential for large fissure cracks that are not able to be fixed through the calendering process. Although possible for both the anode and cathode, this issue has been extensively documented in positive electrodes. [15, 48] Cracking is mainly attributed to the difference in surface tension of water compared to NMP, resulting in capillary pressure buildup as the electrode is dried. [48, 116, 117] As the solvent evaporates from the electrode network, particle-particle interactions also generate a network of strains that eventually reach a critical strain and result in a crack on the electrode surface. This is driven by the drying process in which a pore network is established and as the solvent is removed from the pores, a meniscus is formed and generates a pressure within the pore network. It is the aggregate pressure comprised of these smaller capillary pressures which result in the release of stress via cracking. With the surface tension of NMP considerably lower than that of water (40.79 mN/m, 20 °C and 72.80 mN/m, 20 °C respectively) much greater capillary pressure can be expected when considering the universal equation developed by Singh and Tirumkudulu, Equation 5. [10, 116] Although this area of research has seen great interest in relation to concrete and soil sciences, it is a relatively new issue in the frame of LIB processing.

Equation 5: $$h_{max} = \left(\frac{GM\phi_{rcp}R^3}{2\gamma}\right)^{\frac{1}{2}}$$

The addition of isopropyl alcohol (IPA), which has a surface tension of 23 mN/m, 20 °C, has been shown to improve electrode integrity when paired with water in aqueous processing of NMC 532. [48] Elimination of cracks in electrodes with loadings as high as 25 mg/cm$^2$ were achieved with a 80/20 wt% ratio of DI/IPA, and subsequent electrochemical analysis has shown the performance of such cells is comparable to NMP processed electrodes with the same loading. [48] The addition of IPA as a co-solvent does not however reduce the lithium leaching exhibited by some nickel rich cathode materials that contribute to surface cracking and poor adhesion. [15] Addition of IPA as a co-solvent has also been shown to dramatically affect the viscosity of a dispersion, due to the development of capillary forces that stem from immiscible nature of the two solvents. [15, 118] Although IPA is miscible in water, lithium salts leach into solution during the mixing process and result in salinized water, which is not miscible with IPA and thus leads to changes in viscosity. [15] Although IPA addition is a promising solution, it fails to address the cracks generated by potential current collector instability as a result of lithium leaching out of the active material particle into solution. Thus, a combination of both acid addition as well as IPA inclusion may be a solution to both issues.

### Surface Energy Effect of Interfacial Stability and Adhesion

As the solvent is changed from NMP to DI water, wettability of the current collector has become a concern. As the surface tension of the water is near double that of NMP and the surface energy of the typical aluminum current collector is quite low, resulting in poor

wetting of the current collector during coating. [22] Corona treatment helps combat poor wetting due to surface tension by increasing the surface energy of the aluminum foil by bombarding the current collector surface with free radicals and thus introducing various polar groups to the surface. [22] Similar to capillary forces leading to cracking in the bulk electrode, surface tension can be problematic at the current collector interface. If the surface energy of the substrate and surface tension of the dispersion, which have the same units of measurement, are too dissimilar the resulting electrode will have poor adhesion and show mechanically poor performance. Corona plasma treatments have typically been used to improve adhesion in polyolefin films but have recently been applied to LIBs with the aim of increasing the wettability and subsequent adhesion of $LiFePO_4$ aqueous electrodes. [22] By treating the aluminum surface through Corona plasma process, the removal of adsorbed hydrocarbons and hydroxylation of the thin $Al_2O_3$ layer result in an increased surface energy. Increasing the surface energy from 47.9 $mJ/m^2$ to the measured surface tension of the aqueous dispersions, 62.9 mN/m, allows the dispersion to properly wet the substrate and results in improved adhesion. [22] Ideally the surface energy of the substrate would be close, if not identical, to the surface energy of the dispersion. If the surface energy of the substrate exceeds that of the dispersion, the result may be increased initial adhesion but a reduction in long term adhesion. This can be described by the adhesion energy (initial adhesion) and interfacial tension (long term adhesion) of the system. For ideal performance adhesion energy would exceed 65 $mJ/m^2$ and interfacial tension would be less than 2 mN/m. [22]

Results have shown that moderate Corona treatment was able to increase electrochemical performance of $LiFePO_4$ electrodes processed in water but increasing the surface energy of the substrate too far beyond that of the dispersion possibly resulted in a thicker $Al_2O_3$ layer and subsequent increase in interfacial resistance. [22] The adhesion of the electrode and subsequent electrochemical performance was highly dependent on treatment energy density, with untreated performing the worst. This technique of course would require optimization for each electrode composition, as each solvent and material component can alter the surface tension of the resulting slurry. This treatment also introduces an additional processing step and attached additional cost. Ideally, corona treatment can be implemented as an in line pre-processing step, but since UV rays are involved, proper safety measures must be observed.

## Improving Recycling Efforts

As LIB technology continues to cement its place in a clean energy future, the need for material should not be ignored. As demand for energy storage capability, especially at large scale, increases, so too does the demand for the component materials common in LIB chemistries. [119, 120] As some of the main constituent materials, lithium, cobalt, and nickel are either difficult to source, ethically marred, or scarce (or a combination of the three) LIB production runs the risk of becoming an ecological or socioeconomic crisis if not approached with caution. [119] The need for raw materials for battery production is only compounded by the typical end of life condition of LIBs in that rather than seeing a

second use, they end up in landfills. [121] As a result, potentially reusable materials are discarded and the demand for material only grows. [122] One highly desired solution for resource scarcity as the field continues to increase in market size is battery recycling. Recycling efforts for various other types of batteries, such as lead acid, are commonplace and have been shown to reduce the overall environmental impact of the technology by limiting the need for raw materials. [123] By redirecting spent battery materials away from landfills and into a potential second use in storage applications, the overall demand for materials and associated cost of materials can be reduced. Applying the same mechanics to LIBs can limit the need for new materials and the associated ecological damage caused by surface mining. Whether via materials recovery and use in secondary production, or use for a secondary application, such as excess energy storage for renewables, battery recycling is becoming a critical factor in the use, and disposal, of LIBs. [124]

Battery recycling typically involves either *pyrometallurgy* or *hydrometallurgy* or a combination of the two techniques. [119] In pyrometallurgy, increased temperatures are used to recover materials of interest through a smelting process. In hydrometallurgy, chemical solutions are used to drive separation and precipitation reactions that result in material recovery after solvent removal. [125] Details of exact processing techniques can be found in various reports. [119, 123-129] In hydrometallurgy in particular, separation of the electrode from the current collector material allows for direct recycling of the aluminum and copper current collectors. [130] In order to separate the electrode from the current collector the polymetric binder must be addressed. As this is commonly PVDF in

commercially produced electrodes, the same organic solvent used to disperse the binder can also be used to remove it, typically this solvent is NMP. [120, 129, 131-133] Finding alternative solvents for electrode removal is already an open topic in battery recycling and has seen promising results recently. [11] As NMP is also prominent in battery recycling, the use of aqueous compatible binders though solvent replacement has potential cost savings in recycling as well. If electrodes no longer utilize polymetric binders that require organic solvents for separation, not only are there cost savings associated with the separation phase, but the solvent recovery is similarly omitted as it is in the drying phase of electrode production as previously discussed.

The bulk of recycling processes focus on NMP processed electrodes due to the prominence in battery production. The elimination of NMP and consequently the PVDF binder can simplify the recycling processes due to the minimization, or elimination, of fluorine containing compounds. [121] Not only does fluorine pose an environmental risk in hydrometallurgy, but it can also lead to HF production during thermal treatments in pyrometallurgy as well. [121] Both scenarios which contain environmental and health risks. As anode chemistries typically utilize graphite as the active material, the recovery of anode materials is typically not as economically advantageous when compared to resource scarce metals such as lithium, nickel, and cobalt. Consequently, much of the current research in battery recycling is focused on cathode reuse. LIB recycling is not as mature as LIB production because as utilization has grown, the need for material reuse has also grown and is now becoming economically and environmentally important. [124]

LIB recycling is a burgeoning field that will continue to demonstrate the need for responsible material use and end of life disposal. [134] However, since the practice is still relatively new and under development, the cost of recycling LIBs, particular from consumer electronics, is not yet economically viable. [135] As the market demand for raw materials continues to grow, the economics of recycling will only improve as material scarcity becomes a larger factor. [136] The use of aqueous processing techniques not only can solve environmental concerns associated with the production of LIBs, but also has the potential to reduce the cost and environmental tax associated with reuse of LIBs.

## Future Directions

LIBs have solidified their place as one of the most critical technologies currently on the market. Although recent safety questions have seen a dramatic rise in the use and investigation of solid-state battery technology, many lessons learned during the development and use of LIB technology are easily applied to solid-state applications. Continual development of not only aqueous processing in conventional LIB applications, but also shifting to aqueous processing in solid-state battery technology can assist in the development and production in a more cost efficient and more environmentally friendly end product.

# CHAPTER II
# EXPERIMENTAL METHODS AND TECHNIQUES

## Electrochemical Tests

### *Rate Capability*

As LIBs are optimized for use in automotive applications, one important metric is the rate capability of the cell. Rate capability refers to the ability of the cell to deliver capacity at different discharge rates. Available capacity as a function of discharge rate is of particular interest as the practical acceleration rates of electric vehicles are on the order of 1-3 C. Developing cells that perform well at and above these demanding rates is of upmost importance to ensure adequate performance in real world scenarios. To test discharge capacity as a function of discharge rate cells are first initialized with formation cycling. The formation cycles develop a stable solid electrolyte interphase (SEI) layer and ensure limited side reactions as the cell is tested. After three C/10 formation cycles, each cell is charged at C/3 and then discharged at C/5, C/3, C/2, 1C, 2C, 3C, and 5C for three consecutive cycles at each rate. Three additional C/3 charge, C/3 discharge cycles are then performed to test capacity retention. Capacity retention can help determine if damaging side reactions have occurred as a result of increased polarization present at ultra-high discharge rates. This concern is especially prominent for ultra-thick electrodes which have dramatically increased lithium-ion diffusion path lengths and subsequently are more prone to adverse side reactions at such high discharge rates. Discharge rates are varied as the cathode is of particular interest. Without loss of generality, this same technique can be applied by varying the charge rates in order to evaluate the performance of the anode.

Unless specified, the anode response to rate changes is beyond the scope of the included investigations.

### *Cycle Life*

Cycling a cell until failure is important to understand both how long a cell can be expected to deliver optimal performance as well as determining the failure mode of a cell when it has reached end of life. The service life of the cell can be estimated by cycling at reasonable charge and discharge rates (C/3 unless specified) such that the cell is exposed to real power demand conditions without causing unnecessary polarization effects or side reactions experienced during high-rate cycling. Monitoring the capacity fade as the cell ages provides information on how long the cell can be expected to perform and what potential failure modes are involved at the end-of-life stage. This technique can be paired with post-mortem analysis techniques to further understand particular cell failure modes.

### *Electrochemical Impedance Spectroscopy*

Electrochemical Impedance Spectroscopy (EIS) provides data for modeling the cell resistance and response to voltage perturbation. Unless specified, EIS was performed at 100% state of charge (SOC) and each cell was relaxed for two hours to ensure a stable potential throughout testing. Frequency was varied from 300 kHz to 10 mHz and a voltage

perturbation of 10 mV was used in each case. Collected data was then analyzed using a custom python program developed to implement a Trust Region Reflective algorithm to fit the data to a mathematical model. The mathematical model was developed according to electrochemical impedance principles and the data analysis program fit the data by simultaneously solving the real and imaginary components of the model using the same parameters for both components.

### *Galvanostatic Intermittent Titration Technique*

Galvanostatic Intermittent Titration Technique (GITT) was used to determine the solid diffusion coefficient for structured electrode configurations. [137] Each cell was charged at a rate of C/10 for 15 minutes before being relaxed for 4 hours. During the relaxation period the potential was monitored and allowed to reach a stable value. After the 4-hour relaxation, the cell was again charged at C/10 for 15 minutes and this process was repeated until the cutoff voltage of 4.2 V was reached. A total of 40 steps was required to complete one C/10 charge. This process was then repeated for the discharge of the cell. The resulting data was used to calculate the diffusion coefficient of each cell as a function of state of charge. The method used to calculate the solid diffusion coefficient was presented originally by Weppner et. al. which utilizes the relaxation potential and various electrode characteristics to arrive at a result. [138]

***Ionic Conductivity***

Ionic conductivities of solid-state electrolytes were calculated via Equation 6 where $\boldsymbol{l}$ is the electrolyte thickness, $R$ is the charge transfer resistance, and $A$ is the electro-active area of the cell. Electrolytes were assembled into symmetric lithium|electrolyte|lithium coin cells and tested at 65 ℃.

Equation 6: $$\boldsymbol{\sigma = \frac{l}{R \cdot A}}$$

***Dielectric Relaxation Spectroscopy***

Dielectric Relaxation Spectroscopy (DRS) was used to further analyze impedance data obtained from EIS measurements. The permittivity and conductivity as a function of frequency was calculated and the relaxation modes were analyzed. The dc ionic conductivity was also calculated the high frequency power-law dependance of the conductivity analyzed. All DRS measurements were performed at 65 ℃ using symmetric lithium|electrolyte|lithium cell configurations.

### *Stripping and Platting*

Stripping and platting measurements were performed to evaluate the polarization across an electrolyte film at various current densities. Current densities of 5, 10, 20, 50, 100, 200, and 500 $\mu A/cm^2$ were used with 1-hour intervals alternating between positive and negative currents for five positive and five negative phases at each current density. Symmetric lithium|electrolyte|lithium cells were constructed and tested at ℃.

## Mechanical Tests

### *Dispersion Rheology*

An important characteristic of electrode dispersions (slurries) is their rheological behavior, especially when considering industrial scale manufacturing methods. Electrode dispersions can be treated as colloidal suspensions as the particles are much larger than the medium they are suspended in but are still small enough to be impacted by Brownian motion. [42, 139] The particles in the dispersion are subject to a number of forces including hydrodynamic shear forces, Brownian thermal motion, attractive and repulsive electrostatic and electro steric forces due to surface charge or adsorbed species, among others. [139] An ideal dispersion will have adequate high shear viscosity such that it is mixable and can pass through coating equipment, such as a slot-die coater. An ideal dispersion would also have sufficiently high low shear viscosity, such that after it has been

coated onto a current collector, the dispersion maintains edge definition and overall structure, resulting in a lower scrap rate. [42] These two characteristics are easily measured through flow ramp tests using a bob and cup rheometer geometry.

Flow ramp tests ideally begin with a sample conditioning step to initialize each dispersion in a uniform manner. This is especially important when dispersions have a shear memory or are irreversibly affected by shear stress. A simple flow ramp tests begins at low shear rate and gradually increases to a predetermined maximum. During the test, information such as viscosity, shear stress, and shear modulus information is gathered at each interval.

In addition to viscosity information, rheology can also provide information on the quality of the binding network present in the dispersion by measuring the storage and loss modulus of each sample. In order to measure storage and loss modulus, two additional tests must be performed, frequency sweep and amplitude sweep oscillations. Before performing either test, the dispersion should be conditioned as for a flow ramp test.

All rheological tests were performed using a Discovery HR-3 rheometer (TA Instruments) with either a concentric cylinder (bob and cup) geometry or a Peltier plate (parallel plate) geometry attached. The bob length was 42.01 mm and bob diameter was 28.05 mm. The plate radius was 20 mm. All tests were performed at 25 ℃ unless specified and solvent traps were employed where appropriate.

Due to the shear thinning nature of measured samples, a Herschel – Bulkley model was applied to the data and is given in Equation 7. Here $\tau$, $\tau 0$, $\kappa$, $\dot{\gamma}$, and n represent shear stress, yield stress, consistency index, shear rate, and power law index respectively. [42, 139]

Equation 7: $$\tau = \tau 0 + \kappa \dot{\gamma}^n \text{ if } \tau > \tau 0, \dot{\gamma} = 0 \text{ if } \tau \leq \tau 0$$

***Adhesion Tests***

Electrode adhesion is measured by employing a 180° peel test and averaging the force after initial delamination. This force is then normalized to the sample width to obtain overall adhesion. Multiple samples of the same electrode are tested to ensure statistically significant results. A custom punch die and solenoid press are employed to punch 2 cm wide test strips, providing a consistent width for testing. After punching, samples are placed in a vacuum oven at 110 ℃ (Fisher Scientific) overnight for secondary drying to emulate the electrode production process as much as possible. Once dried, the samples are adhered to the test plate using double sided tape (3M VHB Tape) and a force is applied for 60 seconds to ensure adequate mechanical contact. This force varies between 160 N and 500 N depending on the sample, these differences are noted where the occur. The sample is then peeled at 10 mm/min for 30 mm total. The average force after delamination was used to calculate adhesion.

### *Scanning Electron Microscopy*

Scanning electron microscope images of electrodes are collected both in ‘pristine’ and ‘post-mortem’ states. Cross-sectional SEM images of pristine electrodes is used to confirm desired coating geometry, such as bi-layer electrode structuring. Post-mortem cross-sectional SEM images can determine if layer or electrode delamination occurs during cycling. All SEM images were collected using a Zeiss-Merlin SEM and collection parameters are specified where useful.

### *X-Ray Photoelectron Spectroscopy*

Surface chemistry was determined using an X-ray Photoelectron Spectrometer (XPS). Samples were tested ‘as received’ unless otherwise specified. Both wide energy survey scans as well as narrow energy multiplex scans were collected. A Thermo Scientific XPS was used operating with an aluminum Kα x-ray source with a spot size of 400 μm and photon energy of 1486.6 eV. Samples were affixed to double sided carbon tape before being introduced ultra-high vacuum ($10^{-10}$ mbar). Electronically insulating polymers were charge neutralized using an electron flood gun to neutralize surface charge buildup induced by the photoelectric excitation. Where necessary, sample spectra were corrected to the C 1s peak at 284.8 eV. All the XPS spectra were fitted using CasaXPS.

### *Fourier Transform Infrared Spectroscopy*

Fourier Transform Infrared Spectroscopy (FTIR) was used to determine chemical signatures of polymer samples. A Samples were tested from 4000 $cm^{-1}$ to 400 $cm^{-1}$ with 24 sweeps per sample averaged into one spectrum for each sample.

### *Time of Flight Secondary Ion Mass Spectroscopy*

Time of Flight Secondary Ion Mass Spectroscopy (ToF-SIMS, IONTOF) was used to identify chemical distribution throughout electrodes. Positively charged cesium ions were used to bombard the sample surface and collect chemical composition as well as distribution information from the sample.

### *Zeta Potential*

Surface charge was collected via zeta potential measurements performed using a Brookhaven NanoBrook 90 Plus PALS instrument. Samples were prepared by making a $10^{-3}$ mass fraction solution of the material of interest suspended in $10^{-3}$ wt% KNO3. Sample pH was then modulated between 2 and 11 to obtain a set of samples with increasing pH. Typically, 8 samples were produced. After pH modulation samples were left to equilibrate overnight before testing.

### *Brunauer-Emmett-Teller Surface Area and Pore Size Analysis*

In order to properly calculate the diffusion coefficient, the Brunauer-Emmett-Teller (BET) surface area was obtained for various active materials and electrode configurations. The BET surface area was obtained via nitrogen adsorption and analyzed following the guidance of Thommes et al. [140]

### *Sample pH*

Sample pH is an important characteristic as some materials have stability windows that can be exceeded by natural processes occurring during electrode preparation. For example, when processing nickel-rich NMC materials, excess lithium can leach into solution from the active material particles and result in an increased slurry pH if water was used as the solvent. [13] Sample pH was measured via a pH probe (Fisher Scientific) and depending on the nature of the sample, a filtrate approach was used. If a filtrate was required, samples were mixed ultrasonically (VWR) and allowed to settle before being passed through a 0.2 μm PVDF filter (Whatman) attached to a syringe. This filtrate was then measured with the pH probe.

# CHAPTER III
# OPTIMIZATION OF CURRENT COLLECTOR AND CATHODE INTERFACE IN ULTRA-THICK NICKEL RICH SYSTEMS

A version of this chapter was originally published by Alexander J. Kukay, Ritu Sahore, Anand Parejiya, W. Blake Hawley, Jianlin Li, and David L. Wood III:

Alexander J. Kukay, Ritu Sahore, Anand Parejiya, W. Blake Hawley, Jianlin Li, and David L. Wood III. "Aqueous Ni-rich-cathode dispersions processed with phosphoric acid for lithium-ion batteries with ultra-thick electrodes." *Journal of Colloid and Interface Science* 581 (2021): 635-643.

My contributions to this paper as lead author were 1) performing a literature search to support the importance and relevance of the investigated topic, 2) developing the test matrix of interest, 3) preparing and testing the samples, 4) performing analysis and drawing conclusions from the data. Research support was provided by Ritu Sahore, Anand Parejiya, and W. Blake Hawley on various machines and techniques. Jianlin Li and David L. Wood III provided analytical support as well as assistance in project development and revision.

## Abstract

Lithium-ion battery (LIB) production can benefit both economically and environmentally from aqueous processing. Although these electrodes have the potential to surpass electrodes conventionally processed with N-methyl-2-pyrrolidone (NMP) in terms of performance, significant issues still exist with respect to ultra-thick cathodes (>>4 mAh/cm$^2$ areal capacities). A major concern for these types of electrodes with high-nickel active material stems from lithium leaching from active material, which drives the pH of the dispersion in excess of 12 and subsequently corrodes the current collector interface. As this corrosion reaction proceeds, hydrogen generation at the interface creates bubbles which cause severe cracking in the dried electrode surface. When areal loadings are increased, this effect becomes more pronounced and is detrimental to both mechanical and electrochemical properties of these electrodes. Herein, a technique for mitigating corrosion at the current collector by adjusting the pH of the dispersion with the addition of phosphoric acid is investigated. Phosphoric acid was added in 0.5 wt% increments between 0.0 and 1.5 wt%, and effects on rheology, adhesion, corrosion, and electrochemical performance were investigated. A technique is reported for producing aqueous processed cathodes with areal loadings of 6–8 mAh/cm$^2$ with reduced surface cracking and superior high-rate discharge capacity (i.e., high-power performance) for this class of cathode loadings.

## Background and Relevance

Lithium-ion batteries (LIBs) have transformed the way energy is stored and led to numerous technological developments in the past few decades. LIBs have been widely used for decades in portable electronic devices but still face cost and performance issues when implemented in vehicle and grid storage applications. [40, 141, 142] Although LIBs have been tremendously impactful in recent decades, there is substantial room for improvement. [2] Cost associated with material, labor, overhead, and processing comprise over 80% of total production cost leaving substantial room for cost reduction through new materials and processing techniques. [1, 40, 141] Cathode processing and material costs comprise over 70% of the total cell cost, making the cathode a good candidate for improvement through new materials and processing methods. [1, 40]

Ni-rich layered transition metal oxides are promising candidates for high energy density, low-cobalt active materials that reduce the need for ethically questionable and relatively scarce cobalt. [40] Examples of such candidates are $LiNi_xMn_yCo_zO_2$, $x \geq 0.8$, $z \leq 0.1$ (i.e. NMC 811), which has a practically achievable capacity of 190 mAh/g (theoretical specific capacity of 270–275 mAh/g). [13, 143] As an additional cost reduction measure, cathodes can in some cases be processed using water as a solvent, referred to as ‘‘aqueous processing”. Using water as a solvent eliminates the need for other solvent options, most notably, N-methyl-2- pyrrolidone (NMP). NMP processing is considerably more expensive compared to aqueous processing due to NMP being classified as a volatile organic

compound (VOC), requiring elaborate capture schemes during drying protocols [10]. Aqueous processed electrodes can forego this costly consideration all together, reducing the solvent cost from >$2.25/L for bulk NMP to $0.015/L for deionized water. [141] In addition, utilizing water soluble binders in aqueous processing can ease the binder removal during battery recycle and reduces the environmental impact of the whole battery manufacturing and recycling process. [37]

Aqueous processing has seen great success for anodes but has faced substantial challenges for high-energy cathodes such as $LiNi_{0.6}Mn_{0.2}Co_{0.2}O_2$ (NMC 622), $LiNi_{0.8}Mn_{0.1}Co_{0.1}O_2$ (NMC 811), and $LiNi_{0.8}Co_{0.15}Al_{0.05}O_2$ (NCA) in part due to Li leaching from active materials. However, the low-energy, more water stable (olivine) $LiFePO_4$ (LFP) active material has been successfully commercialized as an aqueous cathode technology, especially in China. [141] Development on this technology started in about 2010 and aimed to reduce processing and material cost through elimination of expensive and environmentally unfriendly binders and solvents. Eliminating costs associated with the materials and mandatory recovery of solvent have been shown to reduce overall battery pack cost by 1–3%. [10] Although aqueous processing maintains potential for substantial cost savings, the replacement of solvent introduced interfacial and surface chemistry issues, notably in $LiFePO_4$ systems. [22, 141, 144, 145] Differences in surface tension of NMP (41.0 mN/m at 25 ℃) and DI water (72.8 mN/m at 25 ℃) result in undesirable wetting and, subsequently, inadequate cycling performance. [22] Agglomeration can occur as a result of interactions between colloidal particles and attractive van der Waals forces. [141]

Minimization of agglomeration due to a dominant van der Waals force is possible by increasing the repulsive Coulomb force, typically by addition of a dispersant to alter the surface chemistry of a particle. [141, 146-149]

When applying aqueous processing to higher energy active materials such as NMC 622, NMC 811, and NCA, another issue arose where transition metal leaching from the layered oxide structures caused via a cation exchange mechanism ($Li^+/H^+$) altered the dispersion pH, leading to a basic dispersion. [150] As high-nickel materials are pursued for higher specific capacities, this Li leaching effect is exacerbated, leading to a highly basic dispersion that corrodes the aluminum current collector during coating. [13, 15, 110] This corrosion subsequently leads to hydrogen gas evolution and formation of bubbles within the cathode dispersion. [15] When dried, these bubbles are responsible for large cracks observed throughout the electrode surface. Such large cracks reduce the cohesion between electrode constituents such that the calendering and punching steps of cell assembly become destructive to the electrode. Reducing the pH of the cathode dispersion during preparation can suppress the corrosive interaction and eliminate hydrogen gas generation, and subsequently eliminate crack formation. If an additive is included in preparation of the dispersion, it is imperative that its benefits largely outweigh any side effects. Past approaches have included coatings applied to the current collector or active material. Although successful, these coatings are costly, introduce a new processing step, and have the potential to reduce the overall electronic conductivity of the electrode. [47, 110, 151]

Another strategy to combat the corrosion phenomenon at the current collector due to transition metal leaching and basic dispersion properties is controlling pH. Previously, hydrochloric acid and polyacrylic acid have been applied in controlling pH of cathode dispersion to improve dispersion homogeneity and mitigate corrosion on Al foil. [150, 152] Herein, phosphoric acid (PA) was added to cathode slurries during preparation in 0.5 wt%, 1.0 wt%, and 1.5 wt% amounts. The purpose of this addition was to increase dissociated protons in the cathode dispersion and drive the pH back to a more neutral value, within the passivation range of the aluminum current collector. Phosphoric acid was chosen because it is inexpensive and readily available. Previous work has shown PA to be compatible with LIB systems but have not investigated the use in thick electrodes, where corrosion takes on a much large role. [15, 47] Properties of the cathode dispersion and mechanical properties of the electrode were quantified as a function of acid content. Additionally, full pouch cells were constructed and electrochemically tested to determine the effects of added acid on cycling performance.

## Materials and Methods

### *Electrode and Pouch Cell Preparation*

All cathode dispersions were prepared using deionized water (purified to 18 MΩ cm using a Milli-Q Direct 8 purifier) and combining 90 wt% NMC 811 (Targray) 5 wt% carbon black (Denka Li-100) and 5 wt% composite binder. The composite binder was comprised

of 1:4 ratio of carboxymethylcellulose (CMC, Acros Organics) and acrylic emulsion binder (JSR TRD202A). Phosphoric acid (Sigma Aldrich) was added in amounts of 0.5 wt%, 1 wt%, and 1.5 wt% after all binding materials were properly dispersed, ensuring an established binder network. Cathode dispersions were mixed using a high-shear rotor stator mixer (NETZSCH Premier Technologies Model 50) such that each component was thoroughly mixed in separate steps, each dispersion had a solids loading of 55%. Resulting dispersions were either used in rheological tests or coated into electrode material. The dispersions were coated into electrodes were coated using a doctor blade with a fixed gap of 500 μm and 750 μm for 6 mAh/cm$^2$ (31.6 mg/cm$^2$) and 8 mAh/ cm$^2$ (42.1 mg/cm$^2$) loadings, respectively. Each cathode dispersion was coated onto an aluminum current collector (MTI Corporation) and allowed to dry.

Anode dispersions were prepared with a final composition of 93 wt% graphite (Superior Graphite 1520-T), 2 wt% carbon black conductive additive (Super C65) and 5 wt% polyvinylidene fluoride (PVDF) binder (9300, Kureha) dispersed in NMP. The anode dispersions were coated with a pilot slot-die coater (Frontier Industrial Technology) using a double-pass method where either 3.3 mAh/ cm$^2$ per pass or 4.4. mAh/cm$^2$ per pass was deposited for total areal capacities of 6.6 mAh/cm$^2$ (18.9 mg/cm$^2$) or 8.8 mAh/cm$^2$ (25.1 mg/cm$^2$), respectively, yielding an electrode capacity balance of N/P = 1.1. The anode dispersion for the first coating pass contained 10 wt% oxalic acid with respect to the binder composition to aid in electrode adhesion. The first pass was fully dried in the oven prior to depositing the second pass to achieve the desired total areal loadings. After calendaring to

30% porosity, all electrodes were placed in a vacuum oven (Fisher Scientific) overnight for secondary drying at 120 ℃.

Single-layer pouch cells with a cathode area of 47.2 $cm^2$ were constructed in a dry room with 0.1–0.2% relative humidity. All cells used a single layer of Celgard 2325 separator material and 1.2 M $LiPF_6$ dissolved in ethylene carbonate (EC) and ethyl methyl carbonate (EMC) in a 3:7 wt ratio as the electrolyte. A fill factor of 1.5 (the ratio of the volume of electrolyte to the total cell pore volume including anode, cathode, and separator porosity [109]) was used when adding electrolyte to each cell. After assembly, cells were cycled at C/10 (1C = 190 mA/g of NMC811) for three formation cycles before undergoing rate capability testing, which consisted of charging at C/3 before discharging at C/5, C/3, C/2, 1C, 2C, 3C, and 5C. Each discharge rate was repeated twice for a total of three cycles at each rate. Upon completion of rate capability testing, each cell was cycled at C/3 charge and C/3 discharge to determine the extent of recovery from high-rate cycling. These rates were then averaged across three cells for each acid concentration for statistical purposes.

***Dispersion Rheology***

After dispersion preparation, 20 mL of each cathode suspension was immediately transferred to a rheometer (Discovery HR-3, TA Instruments) for shear-controlled testing. In addition to 0.0, 0.5, 1.0, and 1.5 wt% solutions, 0.75 and 1.25 wt% solutions were also prepared and tested to confirm an inflection point observed in the data. All samples were

subjected to a pre-shear conditioning step at 5 $s^{-1}$ for 1 min to ensure consistent initial conditions. For all tests, a concentric cylinder geometry (bob and cup) was used with bob length of 42.01 mm and bob diameter of 28.05 mm. Flow ramp testing from shear rates 0.1 $s^{-1}$ to 3000 $s^{-1}$ was used to determine both low-shear viscosity as well as high-shear viscosity.

***Corrosion and pH***

Dilute dispersions of NMC 811 and DI water were added in the same ratios as for a cathode dispersion and mixed ultrasonically (VWR) for 15 min. Appropriate amounts of PA were then added to the solution and mixing continued for an additional 15 min. Conductive additive and binder materials were omitted from these solutions because the pH change is driven primarily by the $Li^+/H^+$ exchange and is not greatly affected by these materials. [13, 150] After mixing was completed, the solutions were rested in order to allow the NMC powder to separate out of solution. After 45 min of rest- ing, the solutions were filtered using a 0.2 μm PVDF syringe filter (Whatman). After filtering, each sample pH was acquired using a pH probe (Fisher Scientific).

Corrosion sample solutions were prepared using the same method as pH measurement samples. Once each solution was prepared, strips of aluminum current collector were added to each solution and agitated for 15 min in an ultrasonic mixer. The sample strips were then rinsed thoroughly with DI water and allowed to dry. Care was taken to not contact the

sample surface as even small amounts of contact can damage the sample surface. [108] Samples were then analyzed via an optical microscope (Keyence) and a binary threshold was used to determine the extent of corrosion in each image.

### *Adhesion Tests*

Adhesion testing was performed via 180° peel tests (Mecmesin Friction Peel Tear). Peel samples were produced from each dispersion via doctor blade coating using a 200 μm wet gap and allowed to dry prior to calendaring each electrode to a fixed 50 μm gap. These samples were then placed in a vacuum oven (Fisher Scientific) overnight for secondary drying prior to being punched into 2 cm strips for peel testing. These samples were then fixed to the peel testing platen using double sided tape (3M VHB Tape) and 160 N of force was applied to the sample for 60 s to ensure intimate contact. Finally, the samples were peeled at 10 mm/min for a total length of 30 mm. Average force after delamination was then normalized to the width of the sample and used to calculate adhesion of the material.

## Results and Discussion

### *Cell Formation*

After assembly each cell was charged and discharged at a rate of C/10 to establish a stable solid electrolyte interphase (SEI) layer. Formation of a stable SEI layer is critical to long

term battery performance and capacity retention. [153] Formation cycles were within the expected specific capacity range of 190 mAh/g for NMC 811 as shown in Figure 1. First cycle coulombic efficiency was calculated for each phosphoric acid concentration. All cell groups had average first cycle efficiencies above 93% as shown in Table 1, ascribed to electrolyte consumption during the first charge/discharge cycle. With thick anodes, considerable electrolyte consumption was anticipated and a fill factor of 1.5 was used to ensure an adequate amount of electrolyte remained after SEI formation. Cycle efficiency recovery after the second formation cycle implies lower electrolyte consumption and indicates adequate SEI formation. As cycling continued, changes in electrode volume have the potential to disrupt SEI formation and lead to increased electrolyte consumption. Over the course of the rate capability cycling, minimal additional electrolyte consumption due to SEI formation was anticipated.

***Cycling Performance***

Initial discharge capacity from C/5 cycles is in agreement with the practical specific capacity of NMC 811 (190 mAh/g) as seen in Figure 2. Cells with 6 mAh/cm$^2$ areal loading display stable discharge capacity exceeding 160 mAh/g until a C/3 discharge rate, at which point maximum discharge capacity degrades sharply. This decrease in discharge capacity is likely due to mass transport limitations encountered in thick electrode systems. For cells with 6 mAh/cm$^2$ areal loadings, the maximum discharge capacity actually decreased from acid-free samples to samples with 0.5 wt% phosphoric acid before increasing at both 1.0

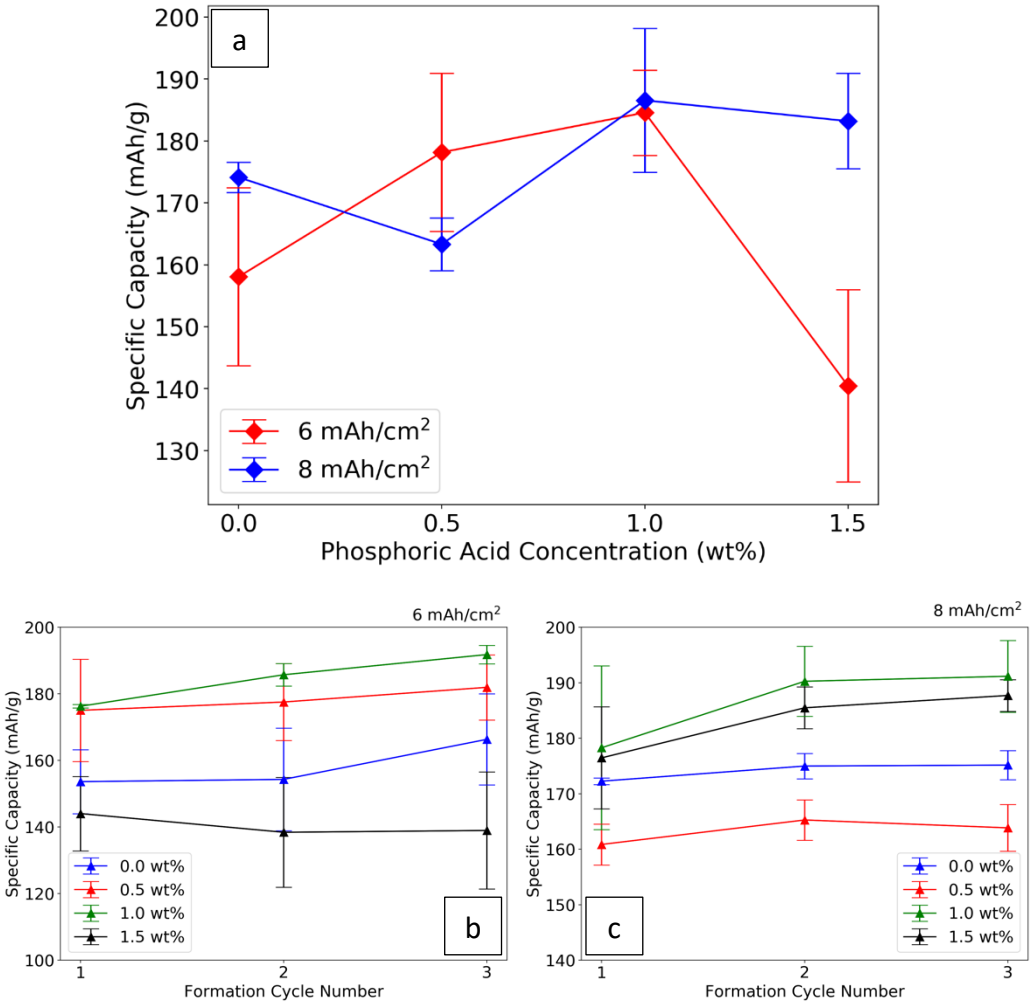


Figure 1. Formation cycling discharge capacity for cells with varying amounts of phosphoric acid, a) average of three cells per concentration, b) average discharge capacity of 6 mAh/cm$^2$ cells used, c) average discharge capacity of 8 mAh/cm$^2$ cells used.

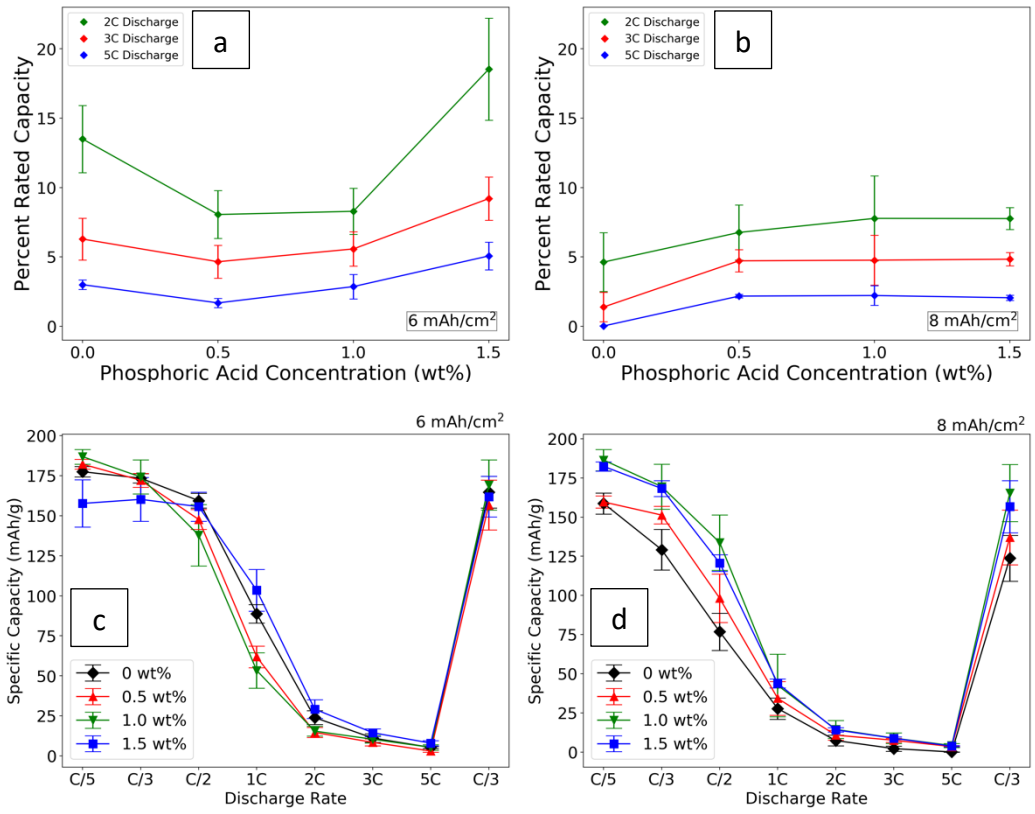


Figure 2. Percent of rated discharge capacity for various phosphoric acid (PA) concentrations for a) 6 mAh/cm2 cathodes and b) 8 mAh/cm2 cathodes; discharge rates of 2C, 3C, and 5C are show in green, red, and blue traces respectively. Rate capability for c) 6 mAh/cm2 cathodes and d) 8 mAh/cm2 cathodes.

Table 1. First cycle efficiency for each phosphoric acid concentration.

| PA Concentration (wt%) | First Cycle Efficiency 6 $mAh/cm^2$ (%) | First Cycle Efficiency 8 $mAh/cm^2$ (%) |
|---|---|---|
| 0.0 | 99.94 | 98.46 |
| 0.5 | 97.89 | 97.95 |
| 1.0 | 96.94 | 96.94 |
| 1.5 | 100.24 | 93.84 |

wt% and 1.5 wt% concentrations. The largest increase compared to control cells occurs at a phosphoric acid concentration of 1.5 wt% where the increases in specific discharge capacity were 5.1 mAh/g, 2.9 mAh/g, and 2.2 mAh/g for discharge rates of 2C, 3C, and 5C respectively.

Similar increases in specific discharge capacity were observed for cells with an areal loading of 8 mAh/cm2 with all samples displaying increased discharge capacity when any amount of phosphoric acid is present. From control samples to cells containing 0.5 wt% phosphoric acid, specific discharge capacity increased by 2.1 mAh/g, 3.3 mAh/g, and 1.2 mAh/g for discharge rates of 2C, 3C and 5C respectively. At an acid concentration of 1.0 wt%, the specific discharge capacity at a discharge rate of 2C increases an additional 1.1 mAh/g to a total of 7.8 mAh/g whereas specific discharge capacities remain steady at discharge rates of 3C and 5C for higher phosphoric acid concentrations. Interestingly, discharge capacity initially decreases with acid concentration for 6 $mAh/cm^2$ cells. The exact mechanism for this decrease requires more investigation, but as the acid concentration increases past 0.5 wt % capacity not only recovers but exceeds initial values. After rate capability testing was completed, each cell performed three recovery cycles at a charge rate of C/3 and discharge rate of C/3 to determine the extent of recovered capacity. Recovered capacity exceeded 91% for all cell subsets. This substantial recovery suggests that the reduction in discharge capacity at high rates was not due to structural degradation, but rather mass transport limitations. Increases in specific discharge capacity are likely due

to a $Li_3PO_4$ coating on the NMC particles and subsequent reduction in charge transfer resistance. [47]

***Dispersion Rheology***

Phosphoric acid addition effects both low-shear viscosity (LSV) as well as high-shear viscosity (HSV) as show in Figure 3. A higher LSV can indicate a strong bridging network in the dispersion that is capable of carrying stresses and resisting particle sedimentation. This has a practical effect of sharpening edge contours and reducing thickness variation throughout the coating, which can reduce the scrap rate for new material. [42, 154, 155] HSV describes how a dispersion would flow under practical coating conditions, where it is important to obtain consistent and even coatings. Shear rates of 0.1 $s^{-1}$ and 340 $s^{-1}$ were used to calculate LSV and HSV respectively. [42]

As phosphoric acid concentration increases from 0 wt% to 1.0 wt % the LSV increases monotonically from 28.3 Pa s to 44.7 Pa s before decreasing monotonically to 25.8 Pa s as the phosphoric acid concentration is increased to 1.5 wt%. A similar trend is observed for HSV; the viscosity increases from 0.75 Pa s to a maximum of 0.89 Pa s at 0.75 wt% phosphoric acid before falling to 0.74 Pa s at 1.5 wt% phosphoric acid concentration. This difference in viscosity is due the combination of Brownian, gravitational, and hydrodynamic forces that affect the particles in the slurries. For micron sized particles,

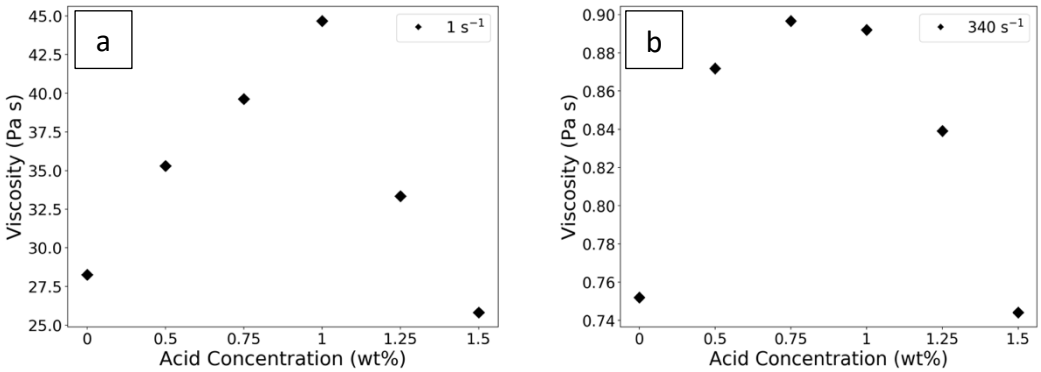


Figure 3. Dispersion viscosity for varying concentrations of phosphoric acid under a) low shear conditions and b) high shear conditions. Low shear viscosity describes how the dispersion will behave while drying whereas high shear viscosity describes how the dispersion will behave during the coating process.

such as NMC 811 ($D_{50}$ of 12 μm), the gravitational forces dominate at low shear rates. As shear rates increase, the involved hydrodynamic forces also increase and a protective surface layer that forms on the active material surface provides an additional surface force that has a larger impact at higher shear rates. [156]

All samples exhibited shear thinning behavior as shown in Figure 4 and can therefore be described as generalized Newtonian fluids [139]. At higher shear rates, the ratio of stress to shear rate decreases and the shear limit follows a power law, thus analysis using the Herschel-Bulkley (H-B) equation is appropriate. This equation is a power law relation described in Equation 7 where $\tau$, $\tau_0$, $\kappa$, $\dot{\gamma}$, and n represent shear stress, yield stress (stress required to initiate flow), consistency index, shear rate, and power law index respectively [42, 139, 145]. When n = 1, this function reduces to the classical Bingham plastic equation; additionally, if n = 1 and s 0 = 0, Newtonian behavior is observed [42, 139, 145]. The high shear behavior of a dispersion can partly be described by the power law index. For dispersions with n < 1, shear thinning behavior is observed, and if n > 1, shear thickening is observed [139]. Data with a shear rate above 5 $s^{-1}$ were considered in the model and parameters obtained from the H-B modeling are listed in Table 2.

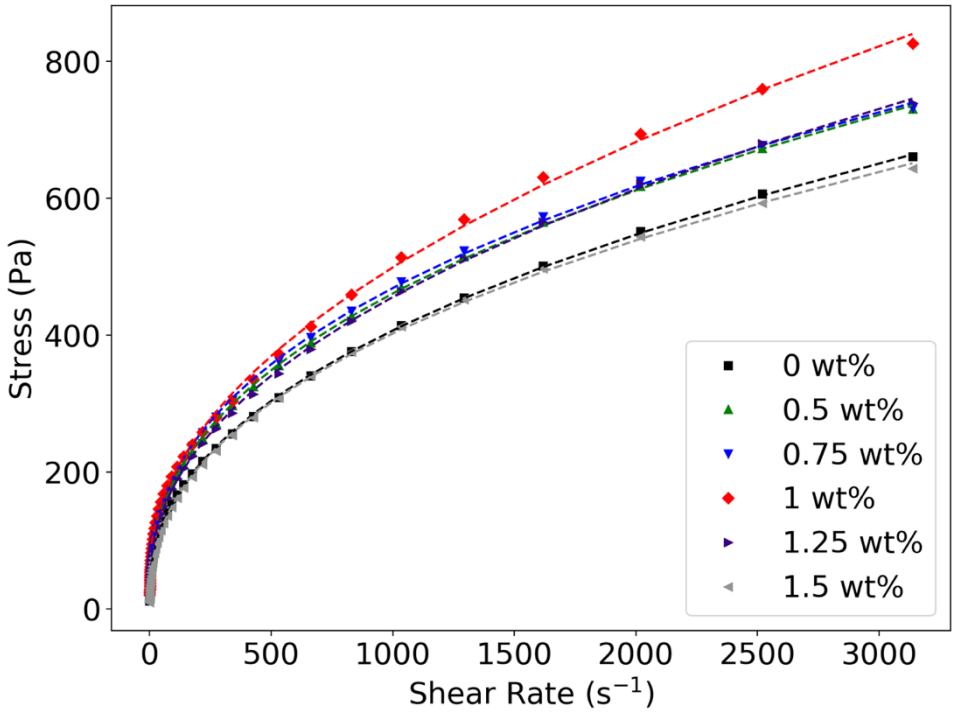


Figure 4. Rheological properties of tested dispersions were fit using the Herschel-Bulkley (H-B) model. Parameters derived from this model are able to describe specific changes that occur within the dispersions.

Table 2. Parameters from Herschel-Bulkley modeling from cathode dispersions.

| PA Concentration (wt%) | Power-Law Index | Consistency Index | Yield Stress (Pa) |
|---|---|---|---|
| 0.0 | 0.44 | 18.03 | 18.65 |
| 0.5 | 0.42 | 23.56 | 20.46 |
| 0.75 | 0.41 | 25.47 | 22.89 |
| 1.0 | 0.50 | 14.18 | 55.45 |
| 1.25 | 0.45 | 18.67 | 28.95 |
| 1.5 | 0.43 | 20.63 | 7.95 |

Changes in yield stress are in agreement with changes in high shear and low shear viscosity as shown in Figure 3 a and b respectively. An increase in yield stress can be explained by an increase in attractive van der Waals forces or reduction of repulsive Coulomb forces, both of which result in increased agglomeration or flocculation. [42, 139, 145] Although yield stress was highest at a phosphoric acid concentration of 1.0 wt%, this is also the concentration that displayed the best electrochemical and mechanical properties, suggesting the additional possibility of agglomerates is worth the increased performance. The power law indices were between 0.41 and 0.50, showing minimal change to the shear thinning behavior of these dispersions. Additionally, with power law index fit parameters of $n < 1$, the characterization of these dispersions as shear thinning is confirmed.

***Corrosion and pH***

The pH of each filtrate is plotted over a time interval of 60 min in Figure 5. The basic nature of the NMC 811 filtrate leads to corrosion of the current collector through a lithium leaching reaction in which excess lithium and surface impurities from the active mate- rial leaches into solution and drives the equilibrium value outside of the stability window for aluminum. [13, 15, 28, 34] As previously reported the reaction follows from reactions

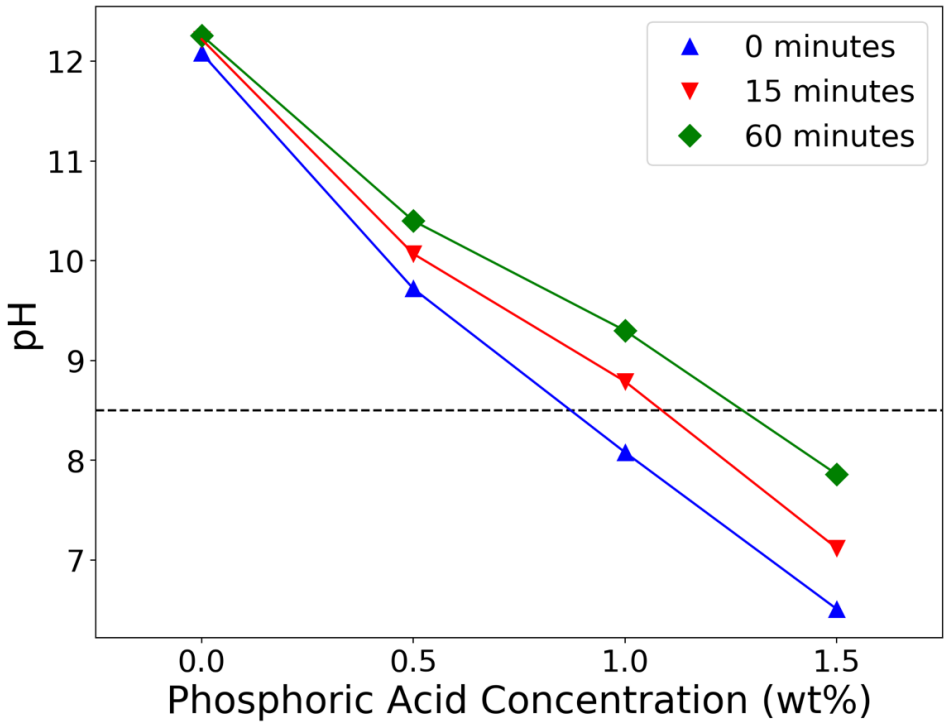


Figure 5. Resulting pH measurements over a period of 60 min for NMC and phosphoric acid dilute dispersions. Initial pH of solutions containing 1.0 wt% phosphoric acid is within the stability window of aluminum but as the Li leaching process continues, the pH rises beyond the stability threshold. Solutions with 1.5 wt% phosphoric acid remained within stability window for the entire test period.

Equation 1-Equation **3**, in which the lithium reacts with the deionized water solvent and produces lithium hydroxide which reacts completely with the available carbon dioxide in the atmosphere to produce lithium carbonate. [13] This lithium carbonate is stable in aqueous solution but the excess of $OH^-$ from the reactions leads to increased pH. [13] The introduction of phosphoric acid does not interfere with the lithium leaching and following reactions, but rather returns pH of the cathode dispersion to the stability window of aluminum of 4.5 to 8.5. [28, 34] Corrosion of the aluminum surface occurs in alkaline conditions, in this case resulting from lithium leaching from NMC 811. If the pH increases beyond 8.5, the aluminum is reduced via reaction Equation 4. [15, 50, 157] Formation of the hydroxide product on the current collector surface can result in reduced interfacial stability and increased interfacial resistance. [109] Images of the corroded current collectors were collected with a light microscope (Keyence) and image analysis was performed via Python image thresholding script seen in Figure 6. Each image was subjected to a 42% intensity threshold, differentiating the light areas of non-corroded current collector and the darker corroded areas. This simple differentiation allows for an estimate of the percentage of the corroded area as show in Figure 6. After thresholding, the effect of acid addition on the corrosion of the current collector becomes clear. The total corroded area was reduced 64% from no acid addition to 0.5 wt% acid content. Adding 1 wt% of phosphoric acid eliminates the corrosion entirely and is comparable to pristine samples. Further increasing the acid content seems to reintroduce surface contamination that may or may not be due to corrosion. Although the spotting is not as indicative as

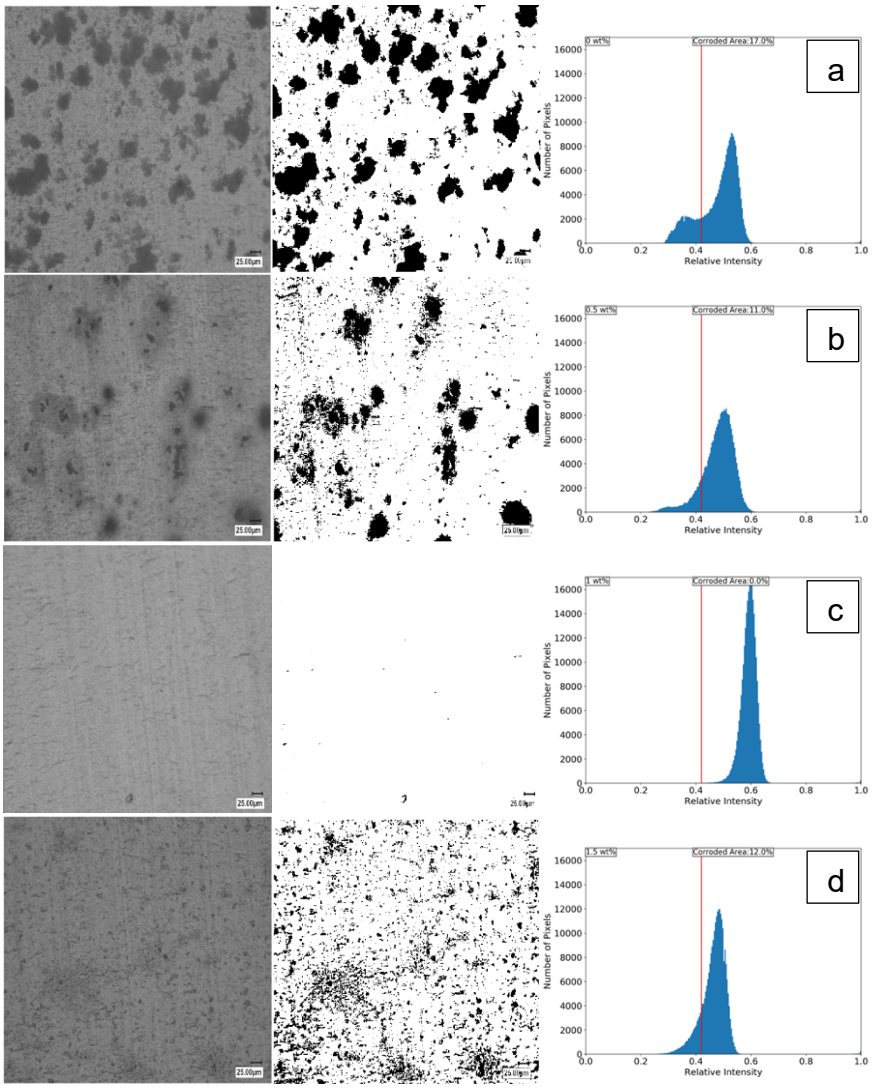


Figure 6. Images obtained from a light microscope in grayscale before processing and after a 42% binary thresholding program was applied to the original image. Corrosion is shown in black regions and uncorroded portions are in white. Histograms depicting the total corroded area for each phosphoric acid concentration are shown for each acid concentration. Acid concentrations of 0 wt%, 0.5 wt%, 1 wt%, and 1.5 wt% are shown in subsets a, b, c, and d respectively.

corrosion as the 0 wt% or 0.5 wt% samples, it still may impact the adhesion and possibly electrochemical performance regardless of composition.

### *Adhesion Tests*

Electrode adhesion is essential when assembling a lithium-ion battery because various manufacturing steps, such as calendering and winding impart stresses on the material. [16] Inadequate adhesion can result in complete delamination of the electrode either during handling or as a result of expansion and contraction experienced during cycling. Reducing the surface corrosion would ideally increase the adhesion by mitigating the hydroxide groups and gas generation that occur at the interface. As shown in Figure 7, the average adhesion is actually superior with no acid content. When acid is introduced, the average adhesion is reduced by approximately 42% at 0.5 wt% acid content. This reduction is attributed to the reduction of available surface area due to the lack of corrosion. Although the corrosion process produces hydrogen gas which results in cracking at the electrode surface, the current collector also increases the available surface area for infiltration of the dispersion, resulting in increased adhesion. [15] The increase in adhesion from 0.5 wt% phosphoric acid to 1 wt% phosphoric acid suggests the hydroxide species that are formed in the corrosion reaction also play a role in overall adhesion but are not as impactful as the available surface area.

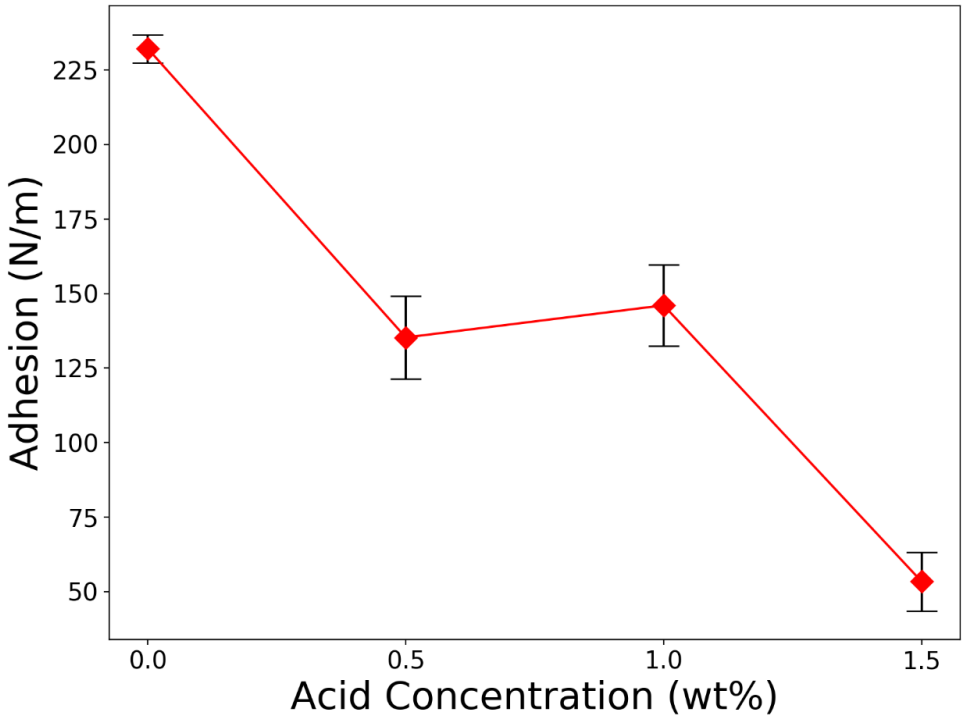


Figure 7. Electrode adhesion normalized to width of test strip. Electrode material was calendared in a fixed gap and punched into 2 cm wide strips for peel testing. A 160 N force was applied to each sample for 60 s before testing to ensure adequate adhesion.

## Conclusion

The addition of phosphoric acid during the dispersion preparation process was investigated in aqueous thick cathodes with the nickel-rich active material NMC 811. With the addition of acid, the corrosion that is typically seen in such systems was reduced at all concentrations and in some cases, completely mitigated. As a result of reduced corrosion and surface pitting, the adhesion of the electrode to the current collector was reduced considerably, but the appearance of surface cracking was eliminated. This suggests the high adhesion in the control samples is due to infiltration of the dispersion into pits caused by the corrosion reaction and the addition of acid eliminated these sites. As corrosion was mitigated, cycling performance improved in cells with thick cathodes suggesting the reduction surface corrosion led to improved mass transport and reduced charge transfer resistance within the electrode. Interestingly, the addition of phosphoric acid altered the rheological properties of electrode slurries, likely due to the domination of gravitational forces and changes to the surface chemistry of the active material particles. Through addition of phosphoric acid, the overall discharge capacity of thick electrode cells was increased, and high-rate discharge capacity was improved with optimal results observed at 1.0 wt%.

# CHAPTER IV
# STRUCTURED CATHODE ARCHITECTURES IN ULTRA-THICK LITHIUM-ION BATTERIES

A version of this chapter will be submitted for publication by Alexander J. Kukay, Kelsey Livingston, W. Blake Hawley, Charl Jafta, David L. Wood III, and Jianlin Li:

My contributions to this paper as lead author were 1) performing a literature search to support the topic of investigation and provided background for the project, 2) development of test matrix and protocols 3) sample testing and preparation, 4) data analysis and subsequent conclusions. Research support was provided by W. Blake Hawley and Charl Jafta. Kelsey Livingston assisted by operating the slot-die coated used to produce various electrodes. Jianlin Li and David L. Wood III provided analytical support as well as assistance in project development and revision.

## Abstract

Ultra-thick (8 mAh/cm$^2$) aqueous processed cathodes can play an important role in achieving environmentally responsible, high energy density lithium-ion batteries (LIBs). Thicker electrodes allow for a higher energy density and reduce the number of inactive components per cell, such as current collector and separator material. However, as electrode thickness increases, lithium-ion diffusion limitations effect usable capacity and hinder high-rate performance in full cells. One method of increasing electrode utilization through thick electrodes is to use a structured cathode approach to shorten the lithium-ion diffusion pathway or increase interaction surface area. Here, different particle sizes are investigated in bilayer systems to improve the lithium-ion diffusion pathways in the cathode and result in a cell with overall improved performance. Two particle sizes of $LiNi_xMn_yCo_zO_2$, $x \geq 0.8$, $z \leq 0.1$ (NMC 811) with average particle sizes ($d_{50}$) of 12 μm and 4 μm respectively are evaluated and used to produce cells with areal capacities of 8 mAh/cm$^2$ utilizing aqueous processing techniques. Cells are then subjected to rate capability, long term cycling, galvanostatic intermittent titration technique, and electrochemical impedance spectroscopy (EIS) protocols to evaluate the effects of particle size on electrochemical performance. Mechanical tests are also performed on each electrode to determine the impact of multilayer coatings on the final electrode structure. Identified is an optimal combination of particle size distribution that promotes high-rate discharge capacity without increasing the ionic resistance of the cathode. The ionic resistance is also identified as the main contributor to reduced high-rate discharge capacity, highlighting the importance of the pore network and tortuosity within the electrode

structure. Electrodes are also shown to be mechanically robust with little evidence of the bi-layer structure leading to any mechanical or electrochemical penalty. The viscoelastic qualities of each particle size are also investigated and show a strong dependance on surface area.

## Introduction

High energy density LIBs with fast charge and discharge capabilities are key to realizing affordable electric vehicles that exhibit a similar range compared to their internal combustion engine (ICE) counterparts. In order to meet the Department of Energy, Vehicle Technologies Office and United States Advanced Battery Consortium targets of $60/kWh and >350 Wh/kg at the cell level, considerable barriers must be overcome, especially if the batteries are processed via aqueous means. [7] An effective way to increase energy density at the cell level is to increase electrode thickness. [158] By doubling the electrode areal capacity from the current standard of 4 $mAh/cm^2$ to 8 $mAh/cm^2$, the number of separators and current collectors are reduced by half thereby eliminating weight and cost of inactive components. [12, 41, 159] This in effect increases the energy density of the cell while simultaneously reducing cost associated with components that do not contribute to useable capacity. [160] However, such thick electrodes are not trivial to process with aqueous methods and increasing the energy density via thicker electrodes risks decreasing power density. [161] Power density can easily be decreased with increasing electrode thickness as the lithium-ion diffusion is a non-linear process which becomes more important as length is increased. [162] As such, increasing the areal capacity beyond 8 $mAh/cm^2$ has been shown to lead to diminishing returns in electrochemical and mechanical performance due to both lithium-ion diffusion limitations and reduced electrode integrity. [160] In addition, between corrosion at the current collector and subsequent hydrogen gas generation and surface tension related cracking, aqueous processed ultra-thick electrodes

have their own associated mechanical challenges. [14, 15, 48] Regardless of the challenges, ultra-thick electrodes are seen as an effective method for increasing the energy density of a cell and multi-layer coatings allow for tailored electrode compositions for specific applications. [12, 163]

Along with increasing electrode thickness and subsequently energy density, utilizing aqueous processing techniques is an effective technique for both reducing processing costs and reducing environmental impact during electrode processing. [10, 12, 14] Aqueous processing of nickel rich materials such as NMC 811 has been shown to be effective and ultra-thick electrodes (8 $mAh/cm^2$). This was previously demonstrated through the addition of a small amount (0.5 wt%) of phosphoric acid combating the pH rise from lithium leaching, which drives a lithium proton exchange reaction to form LiOH and increases slurry pH. [13] The addition of phosphoric acid keeps the slurry pH within the stability window of aluminum and avoids corrosion and subsequent hydrogen gas generation which is detrimental to the resulting mechanical stability of the electrode. [13-15, 28, 34] The addition of phosphoric acid to nickel-rich active material has also been shown to form a protective coating on active material particles that improve cycle stability by limiting leaching of lithium from the active material during slurry processing. [156]

Increased electrode thickness poses an electrochemical limitation, as the thickness increases, so does the importance of lithium-ion transport limitations within the structured pore network. [63] Unlike in thin electrodes where lithium-ion diffusion in the electrolyte

can be largely neglected, the large increase in lithium-ion diffusion path length of ultra-thick electrodes means the diffusion limitations become significant. [163-165] Reducing the particle size can shorten the lithium-ion diffusion length in the solid phase and also increase the surface area, which is the active site for lithium-ion exchange between the solid and liquid phases. [48, 166] However, smaller particle size may result in increased tortuosity and longer liquid diffusion length in porous electrodes, evidence of this increased resistance is provided in this work.

Altering the electrode architecture has long been a topic of interest in battery manufacturing and optimization and has been shown to lead to significant changes in battery performance. [167] Understanding the physical mechanisms behind the altered parameters is also important as the true mechanisms can be quite complex. [168] Although some studies have addressed the porosity and thickness of electrodes and their subsequent performance, there is little empirical information concerning how altering the electrode structure via particle size variation effects the performance of ultra-thick cathodes. [163, 169-171] Several other electrode structuring techniques have been suggested and various attempts have been reported. Such techniques include variation of porosity, magnetic structuring, freeze tape casting, 3D printing, and laser ablation in order to obtain a desired electrode design. [60, 111, 172-174] However, those techniques have yet been demonstrated at scale. [41]

An empirical investigation involving discrete layers of the same $TiO_2$ with differing morphologies showed beneficial electrochemical properties when compared to a heterogenous composition. [175] Further reports of varying particle size have also been promising, but they have been limited to coin cell configurations rather than pouch cell format, or low electrode areal loadings. [175, 176] Wood et al conducted a rigorous investigation into particle size effects in 3.6 mAh/cm$^2$ N-methyl-2-pyrrolidone (NMP) processed NMC 532 cathodes in full pouch cell format and found that a smaller particle size, in this case 6 μm ($d_{50}$) near the separator and 12 μm ($d_{50}$) near the current collector was able to increase the high rate discharge performance by 2X. [177] Not only does this result confirm the findings from multiple previous studies, it provides a scalable and cost effective way to increase the energy density and high rate performance of a cell with minimal disruption to a roll-to-roll process. In their work the authors conject the lithium-ion diffusion is less constricted near the separator. Therefore, the higher packing density is not restrictive, and the increased surface area is able to increase the active material usage in that region. Meanwhile, the lithium-ion diffusion near the current collector is limited due to the increased lithium-diffusion length, thus a larger particle size leads to a less restrictive packing density and allows the lithium-ions to travel more freely, even though there is less surface area for the ions to interact with. [177]

In this work a similar approach to Wood et al is used as two particle sizes of $LiNi_xMn_yCo_zO_2$, $x \geq 0.8$, $z \leq 0.1$ (NMC 811) 12 μm ($d_{50}$) and 4 μm ($d_{50}$), sourced from the same supplier (Targray) were used to produce slot die coated ultra-thick (8 mAh/cm$^2$) bi-

layer cathodes with distinct particle size distribution. The ultra-thick electrode configurations and aqueous processing approach increase the energy density of the cell while simultaneously implement a more environmentally benign processing technique. The subsequent batteries were tested for improvement in high-rate discharge capacity and cycle life. EIS tests were also performed every cycle for 50 cycles to monitor impedance as the cell ages. The electrode composition with mixed 12 μm and 4 μm NMC near the current collector had the best high-rate discharge capacity likely due to the combination of increased active material surface area for intra-particle lithium-ion diffusion and a less restrictive pore network. Anode compositions were limited to two variations, a baseline all large particle graphite configuration (Superior 1520-T) and a combination small particle graphite (Superior 1506-T) followed by large particle graphite (Superior 1520-T). These two anode configurations were previously identified as being the worst and best performing anode geometries. [177, 178] These configurations were used to further investigate the mechanism proposed by Wood et al and shed light on the mechanism responsible for the observed performance differences. [177] Although the results provided in this work are promising, the challenge of 8 $mAh/cm^2$ aqueous processed LIBs that can deliver adequate power density as well as increased energy density is still ongoing. The inclusion of additional cell configurations can optimize the thickness of each bilayer and should be the focus of future work. A promising result is the identification of ionic resistance within the electrolyte as the main contributor to the performance differences. Also identified is an unstable CEI layer that affects performance as the electro-active area is increased.

## Experimental Methods

### *Pouch Cell Preparation and Assembly*

Single-layer pouch cells with a cathode aerial capacity of 8 mAh/cm$^2$ (50.2 mg/cm$^2$) were produced by coating two 4 mAh/cm$^2$ (25.1 mg/cm$^2$) passes using a pilot scale slot die coater (Frontier Industries), a technique that is readily scalable to industrial applications. An N/P ratio of 1.1 was maintained for all anode-cathode pairs. Bi-layer coatings were used due to drying considerations as binder migration and crack formation becomes a significant problem as coating thickness increases, creating technical challenges for single pass coatings. [48] A baseline composition of 89.83% active material, 4.83% conductive additive, and 4.83% composite binder, 0.5% phosphoric acid was used for each cathode. Nickel-rich NMC 811 (Targray) was used as the active material, in two different particle sizes, 12 μm and 4 μm. In some cases, an alternate composition of 89.5% active material, 4.5% conductive additive, 4.5% composite binder, and 1.5 wt% phosphoric acid was used due to excess corrosion of the current collector and resulting poor adhesion. These electrodes are noted in Table 3. In all cases the processing solvent was DI water purified to 18 MΩ cm using a Milli-Q Direct 8 purifier. Carboxymethylcellulose (CMC, Arcos Organics, MW = 700,000, D.S. = 0.9) and an acrylic emulsion binder (JSR TRD202A, JSRMicro) in a 1:4 weight ratio comprised the composite binder. Carbon black (Denka Li-100) was used as the conductive additive and phosphoric acid (Sigma Aldrich) was used to suppress corrosive effects. [14] For baseline anodes a formulation of 92 wt% graphite

Table 3: Electrode composition for each configuration of interest.

| Coating Name | First Pass Cathode Active Material Size | First Pass Cathode Acid Content | Second Pass Cathode Active Material Size | Second Pass Cathode Acid Content | First Pass Anode Active Material Size | Second Pass Anode Active Material Size |
|---|---|---|---|---|---|---|
| 4 μm | 4 μm | 0.5 wt% | 4 μm | 0.5 wt% | 18 μm | 18 μm |
| 12 μm | 12 μm | 1.5 wt% | 4 μm | 0.5 wt% | 8 μm | 18 μm |
| Mixed | 12 μm 4 μm Mixed | 1.5 wt% | 4 μm | 0.5 wt% | 8 μm | 18 μm |

(Superior), 2 wt% carbon black (C-65, Imerys Graphite & Carbon), 4.8 wt% SBR (Targray), and 1.2 wt% CMC (Arcos Organics, MW = 250,000, D.S. = 0.9) was used. Both anode and cathode slurries were mixed in a planetary mixer (Ross PDM – 1/2). Schematics of the resulting electrodes can be seen in Figure 8.

As coated electrodes were calendered to 30% porosity and subsequently dried in a 110 °C vacuum oven (Fisher Scientific) overnight to eliminate residual water before being assembled into single layer pouch cells. Secondary drying was used to removed residual water reported to be present in aqueous electrodes and which can lead to HF generation. [10, 65] Pouch cells were assembled using Celgard 2325 separator and 1.2 M $LiPF_6$ dissolved in ethylene carbonate (EC) and ethyl methyl carbonate (EMC) in a 3:7 weight ratio electrolyte in a dry room with relative humidity 0.1 – 0.2%. A fill ratio of the volume of electrolyte to total cell pore volume including anode, cathode, and separator porosity of 1.5 was used for each cell. [179] Cells were vacuum sealed and tested under a stack pressure of 38 kPa (5.5 PSI). Three cells were produced for each configuration for statistical purposes.

***Long Term Cycling Performance and High-Rate Discharge Capacity***

Each cell was subjected to three formation cycles at C/10 (1C = 190 mA/g NMC 811) and constant voltage charge at 4.2 V until current dropped to C/20 to develop a stable solid

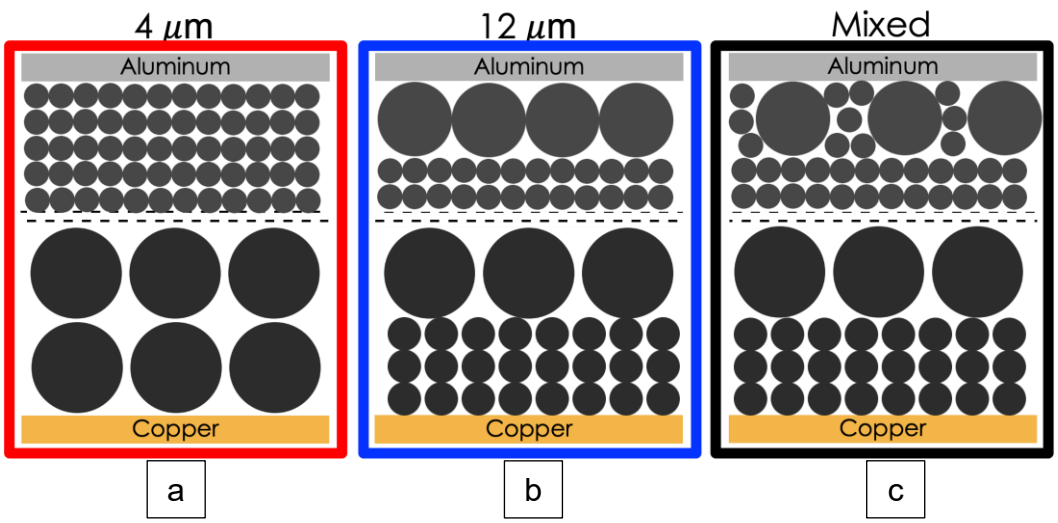


Figure 8. Electrode configurations tested in this study. Each electrode was constructed by coating two 4 mAh/cm$^2$ passes with a pilot scale slot-die coated. The first layer was coated and dried before the second layer was coated on top. The bi-layer technique was used to minimize extreme binder segregation and surface tension induced cracking that has been known to occur in thick electrode systems processed with DI water.

electrolyte interphase (SEI) layer. [69] After formation, cells were cycled at C/3 charge and C/3 discharge until failure. All cells were cycled using a Maccor potentiostat at 30 °C in a controlled environmental chamber (ESPEC).

Another set of triplicates per configuration were evaluated for rate performance Each cell was charged at C/3 and again held at 4.2 V until the current dropped to C/20. Cells were then discharged at C/5, C/3, C/2, 1C, 2C, 3C, 5C for three cycles at each discharge rate. After the rate test was completed, three C/3 recovery cycles were performed to evaluate capacity fade educed during high-rate discharge.

***Electrochemical Impedance Spectroscopy***

Another additional pouch cell per configuration was produced and used for EIS testing. After three C/10 formation cycles, each cell was charged to 4.2 V (100% state of charge) and then allowed to rest for 2 hours before performing an EIS sweep from 300 kHz to 5 mHz with a perturbation of 10 mV using a Biologic VSP battery tester (Biologic USA). After EIS, each cell was then discharged to 3.0 V. This process was repeated every cycle for 50 cycles at C/3 to gain an understanding of how overall impedance increases as the cell continues to age.

### *Symmetric Cells*

Symmetric cathode|cathode cells were constructed to determine the cathode contribution to impedance at both 0% and 50% SOC. Full coin cells were first constructed before undergoing three formation cycles at C/10. Cells were then discharged to either 50% SOC (3.6 V) or 0% SOC (3 V) with a two-hour voltage hold before disassembly. The harvested cathodes were then reconstructed into electronically blocking symmetric cells containing new electrolyte. EIS spectra from 300 kHz to 5 mHz was then collected at 30 °C.

### *Diffusion Coefficient Determination*

Chemical diffusion coefficients for each electrode configuration were calculated via the galvanostatic intermittent titration technique (GITT) developed by Weppner and coworkers [180]. This method is widely used and requires accurate measures of surface area and molar volume, both difficult to obtain. [138] Other models have also been employed but are not the focus of this work and can be found in literature. [181, 182] As the materials used in each configuration were similar, the implicit assumptions in the model may have an impact on the resulting magnitude of the measured value, however these effects are consistent across all samples. As the goal is to compare the samples among each other, these assumptions were deemed to be acceptable. A critical review of the implicit assumptions involved in GITT data collection can be found in literature. [183]

Cells were first charged at a constant rate of C/10 for 15 minutes using a Biologic potentiostat (Biologic USA) before entering a relaxation period of 4 hours with no applied potential. After the relaxation period, the charge processes were repeated again followed by the relaxation step. These steps were repeated until the charge cutoff voltage of 4.2 V was reached, a total of 40 charge events. This technique was then repeated with a negative current to achieve one full charge discharge cycle for each cell configuration.

***Microstructure Determination***

Scanning electron microscopy (SEM, Zeiss-Merlin) imaging was used to confirm the structured electrode microstructure after slot-die coating. Samples were cut using ceramic scissors and mounted edgewise with conductive carbon tape to observe the electrode cross-section.

***Dispersion Rheology***

Small scale dispersions were mixed in 10-minute steps via a high-shear rotor-stator mixer (NETZSCH Premier Technologies Model 50) for a minimum of 40 total minutes to ensure homogenous distribution of each component as the order of addition and mixing technique was previously found to affect binder distribution. [14] First CMC and NMC 811 were mixed, followed by carbon black, JSR emulsion binder, DI water, and finally phosphoric

acid, mixing thoroughly after each addition. After mixing, 20 mL of each dispersion was used for rheological measurements. Rheological properties of each dispersion were evaluated by a rheometer (TA Instruments Discovery HR-3) at 25 °C using a concentric cylinder geometry (bob and cup). Samples were pre-sheared at 5 $s^{-1}$ for 1 minute and relaxed for 30 s before measurement. Separate identically prepared samples were used to further investigate the low shear viscosity behavior of each configuration in more detail.

To further investigate the low shear behavior of each dispersion, oscillatory shear measurements were performed using the same rheometer and geometry used for previous flow ramps tests. Both oscillatory strain and angular frequency were varied in separate tests with a rebuilding procedure between tests to recover the initial dispersion conditions before each test. After an identical slurry preparation procedure and sample conditioning observed for flow ramp testing, angular frequency was held at $\omega$ = 100 rad $s^{-1}$ while varying oscillatory strain from $\gamma$ = 0.01 – 10%. After oscillatory strain sweep, a 10 minute rebuild procedure where angular frequency and oscillatory strain were held at $\omega$ = 100 rad $s^{-1}$ and $\gamma$ = 0.01% respectively in order to recover the storage and loss modulus from initial conditions. Data collected from the rebuild procedure was monitored to ensure the dispersion had adequately recovered from the initial test. After rebuilding, a second test was applied where oscillatory strain was held constant at $\gamma$ = 0.1% and angular frequency was varied from $\omega$ = 100 – 0.1 rad $s^{-1}$. The oscillatory strain chosen for testing was based on critical strain, the point where the measured storage modulus falls below 95% of the measured maximum as discussed in literature. [42]

### *Adhesion Tests*

Adhesion strength between electrodes and current collector was evaluated using a 180-degree peel test (Mecmesin Friction Peel Tear) at 10 mm/min. Adhesion was calculated by normalizing the average force after delamination to the width of the sample strip. A minimum of 3 samples per configuration were included.

## Results and Discussion

### *Dispersion Rheology*

Rheological behavior of the dispersions identifies trends in low and high shear viscosity that affect the coating quality and by analogue the final electrode. Low shear viscosity behavior is directly attributable to the edge formation, while high shear viscosity is critical in determining coating window. [42, 154, 155] As shown in Figure 9 (a) and (b), all dispersions showed shear thinning behavior. Shear stress and viscosity increased with the reduction of particle size and is ascribed to increased surface area which generates increased drag within the dispersion. Because the samples are shear thinning in nature a Herschel-Bulkley (H-B) model was used to fit the data and is presented in Equation 7. [139] Here $\tau$, $\tau 0$, $\kappa$, $\dot{\gamma}$, and n represent shear stress, yield stress, consistency index, shear rate, and power law index respectively. [42, 139] Fit parameters for the applied model are listed in Table 4. When reducing the particle size from 12 μm to 4 μm, the power law

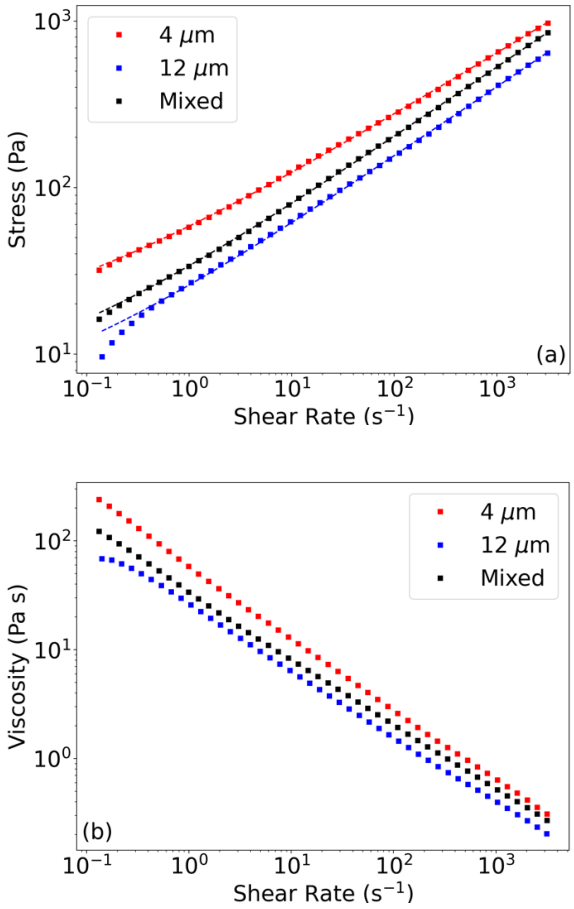


Figure 9. Rheological properties for each particle mixture, a) stress as a function of shear rate and b) viscosity as a function of shear rate.

Table 4: Herschel-Bulkley model fit parameters for each particle size. Similar power-law index values suggest a similar degree of shear thinning in each sample whereas differing consistency index values point toward more particle-particle interactions during the test resulting in increased drag.

| NMC 811 Particle Size | Power-Law Index [$n$] | Yield Stress (Pa) [$\tau_0$] | Consistency Index [$\kappa$] |
|---|---|---|---|
| 4 μm | 0.375 | 11.398 | 47.306 |
| 12 μm | 0.421 | 4.174 | 21.837 |
| Mixed | 0.422 | 5.621 | 28.337 |

index also decreased, suggesting a greater extent of shear thinning. The yield stress for the 4 μm particle size dispersion (red) is almost 3X that of the 12 μm dispersion (blue), likely due to an increase in viscoelastic drag resulting from increased surface area. The large increase in yield stress suggests an increased binding network present in the small particle size sample. [42] Similar power-law index values suggest a similar degree of shear thinning in each sample whereas differing consistency index values point toward more particle-particle interactions during the test resulting in increased drag. Results from the dispersion with mixed particles (black) are between that of the purely 12 μm and purely 4 μm dispersions in agreement with the trend of surface area. Additionally, the viscosity at low shear rate of the mixed dispersion was closer to that of the 12 μm dispersion, suggesting the binder network the mixed dispersion more resembles that of the 12 μm sample.

In order to further investigate the low shear viscosity behavior exhibited by each dispersion, oscillatory shear measurements were taken to identify differences in storage modulus (G') and loss modulus (G''). Low shear viscosity storage and loss modulus tests can show where breakdown of the polymer binder begins to occur and effect the resulting binding network of the resulting electrode. [42] Low shear viscosity is responsible for the edge formation in the resulting electrode and storage modulus is related to the binder network within the electrode. As shown in Figure 10, the dispersion with 4 μm particle size (red) has a storage modulus more than double that of the 12 μm sample (blue). This drastic increase in storage modulus is likely due to increased surface area of the smaller particle size. The storage modulus of the mixed sample (black) was between the two values. Along

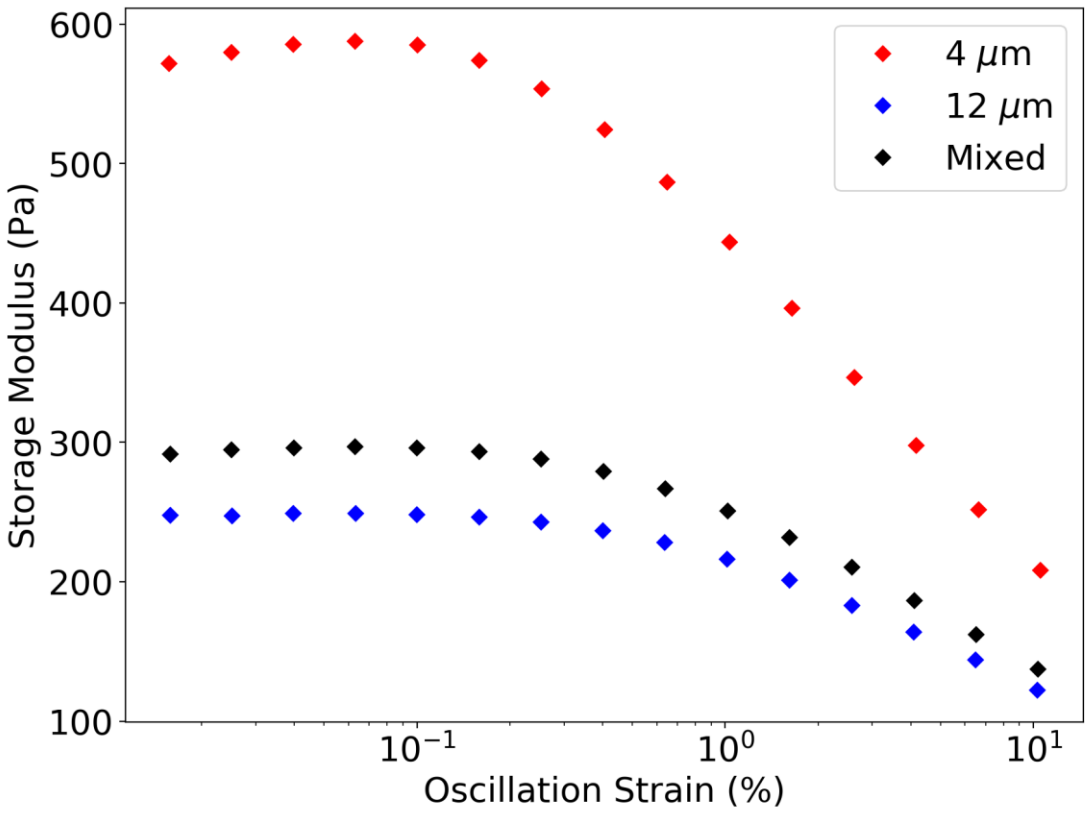


Figure 10. Storage modulus data as a function of oscillation strain. The near 2X increase in storage modulus for the small particle size (red) suggests the binding network is highly distributed within the sample, likely due to the increased surface area for binding site as well as the increased number of particles that act as nodes in the binding network.

with the increased area for interacting with binder particles, this results also suggests the smaller active material particles have similar, if not better, dispersion than the larger particles. This reduced agglomeration potential is further supported when the surface charge is considered. As shown in Figure 11, the smaller active material particle (red) displays a zeta potential of greater magnitude (more negative) than that of the large particle (blue), even when normalized to surface area. This means the smaller particle is more stable in suspension and less likely to agglomerate during mixing. This increased dispersions on surface charge provide evidence of electro-steric stabilization being the dominant force and potentially reduces the sedimentation potential of the 4 μm active material.

Increased storage modulus can lead to a more well-defined electrode edge formation, resulting in a reduced scrap rate as less of the electrode would need to be trimmed after coating. This benefit is partially negated by the increased viscosity of the same 4 μm active material particle as the coating speed may need to be reduced. Previous investigations using NMP based dispersions suggest raising the slurry temperature could counteract this increase in viscosity. [42] This would however introduce extra processing steps and use more energy during manufacturing.

***Adhesion Tests***

The adhesion increased ~50% when small particle active material was present as shown in Figure 12. As previously discussed, the dispersion of the active material particles with

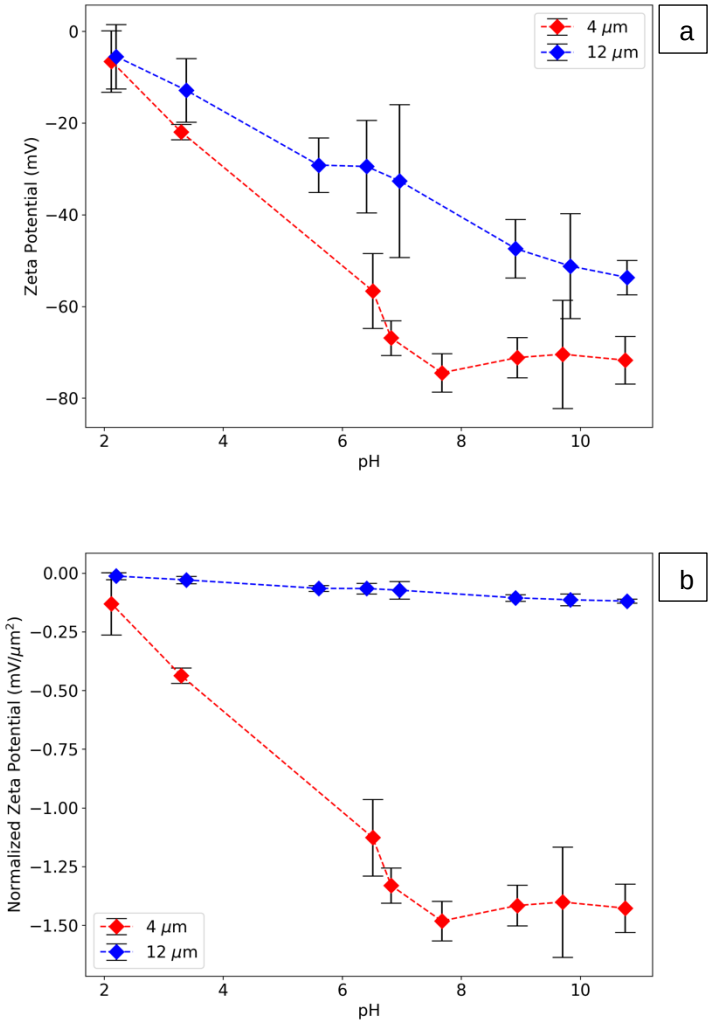


Figure 11. Surface charge for 4 μm (red) and 12 μm (blue) active material particles both a) as measured and b) normalized to the particle surface area.

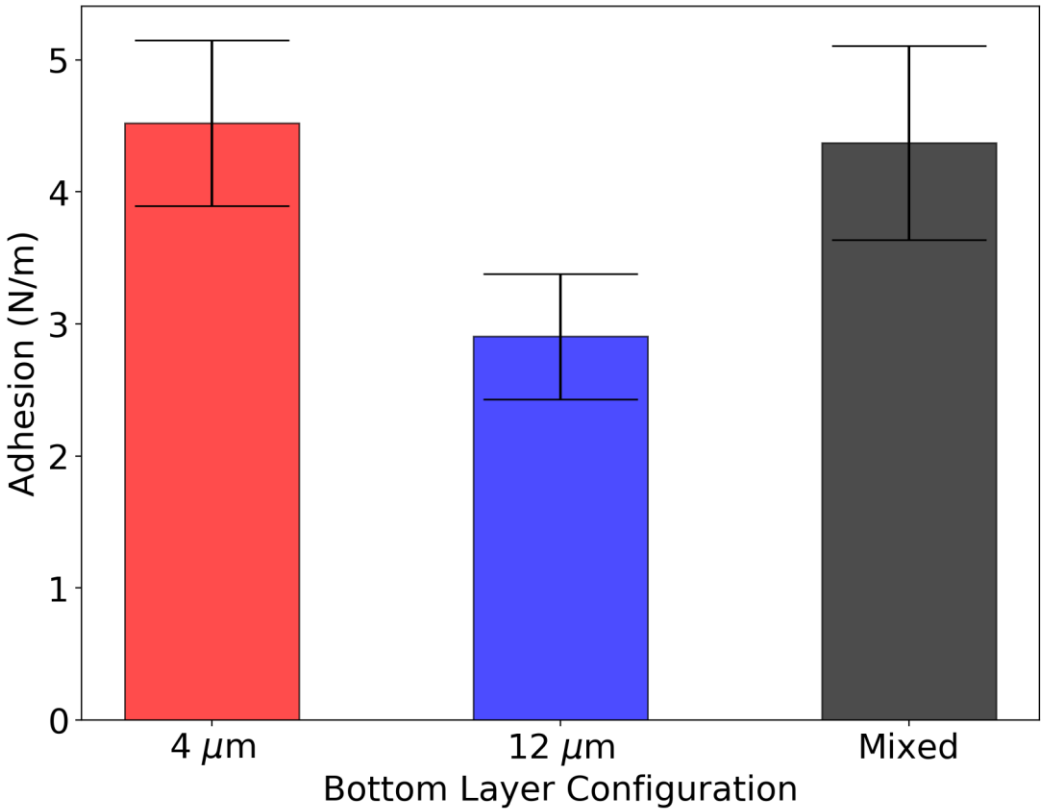


Figure 12. Adhesion strength of the three NMC 811 cathodes.

smaller 4 μm particle size (red) is better than that of the larger 12 μm particles (blue) and thus offers more available surface area for binder attachment. This increased binder distribution on the surface of the particles results in a more rigorous binder network. The contact area between the electrode material and the current collector is also larger due to the surface area increase easily explaining the adhesion increase. As the mixed sample (black) also exhibits a larger adhesion than that of the 12 μm particles the dependance on surface area is reinforced. As 5 wt% composite binder was used for these electrodes, the sufficient adhesion even with increased surface area is in agreement with previous reports of minimum binder amounts as low as 2 wt% and suggests adequate binder exists in all electrode configurations for proper adhesion and cohesion. [87, 94] Furthermore, the bi-layer nature of the electrode cohesion is shown to be greater than that of the adhesion as the electrode material was peel cleanly from the current collector. This implies the interface between the two electrode layers is stable and does not affect the mechanical integrity of the electrode.

***Microstructure Determination***

SEM confirms the desired electrode structure with minimal separation between electrode layers suggesting suitable cohesion between the two electrode layers before cycling. These electrode microstructures can be seen in Figure 13. In all cases, no indication of a discontinuous electrode exists, again suggesting the cathodes are in good mechanical contact and provide sufficient electronic conductivity.

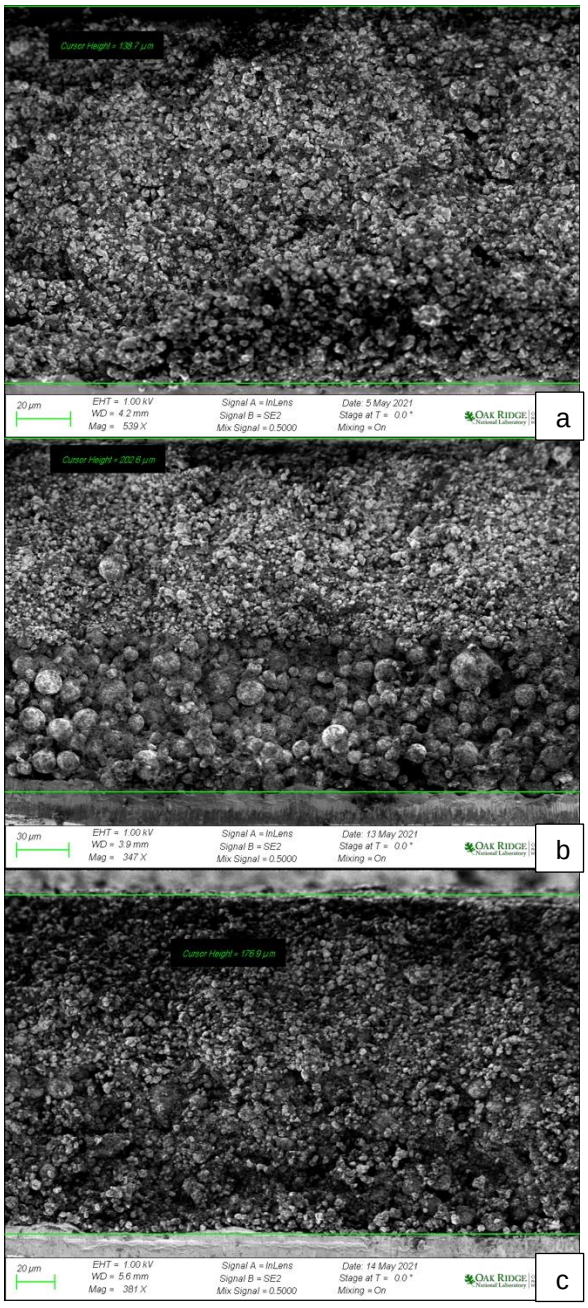


Figure 13. SEM microstructure of each cathode configuration, a) all small configuration, b) large particle size followed by small particle size configuration, and c) mixed particle size followed by small particle size configuration.

### *Long Term Cycling Performance*

Long term cycling of all electrode configurations was poor, and the longest lasting cell only reached ~160 cycles at C/3 charge and C/3 discharge. After 150 cycles the capacity retention for the mixed electrode configuration (black) falls to ~20%, demonstrating severe capacity fade as seen in Figure 14. Rate capability results suggest each electrode configuration should maintain >65% of rated capacity when cycled at C/3, but this performance does not last. This is thought to be caused by electrolyte consumption via adverse side reactions. These side reactions lead to a passivation layer on the active material particle which increase the charge transfer resistance. [47, 115] As the polarization of the cell increases, the capacity of the cell decreases accordingly. The cathode with large active material particles near the current collector (blue) exhibited the best cycle life performance among the group and the cathode with mixed particle sizes near the current collector (black) exhibited the worst performance. The small particle sample (red) exhibited the fastest initial decrease in performance followed by milder long term fade. This is likely due to the increased surface area of the active material present in the mixed sample meaning more surface area for the react with the electrolyte. This provides additional support for the formation of a passivation layer that is the main source of the quick capacity fade and poor cycle life. This capacity fade is also visualized in Figure 15, as the cells age, the capacity vs. voltage plots shows a decrease in available capacity as cell polarization increases as a function of cycle life. This mechanism is further discussed in following sections.

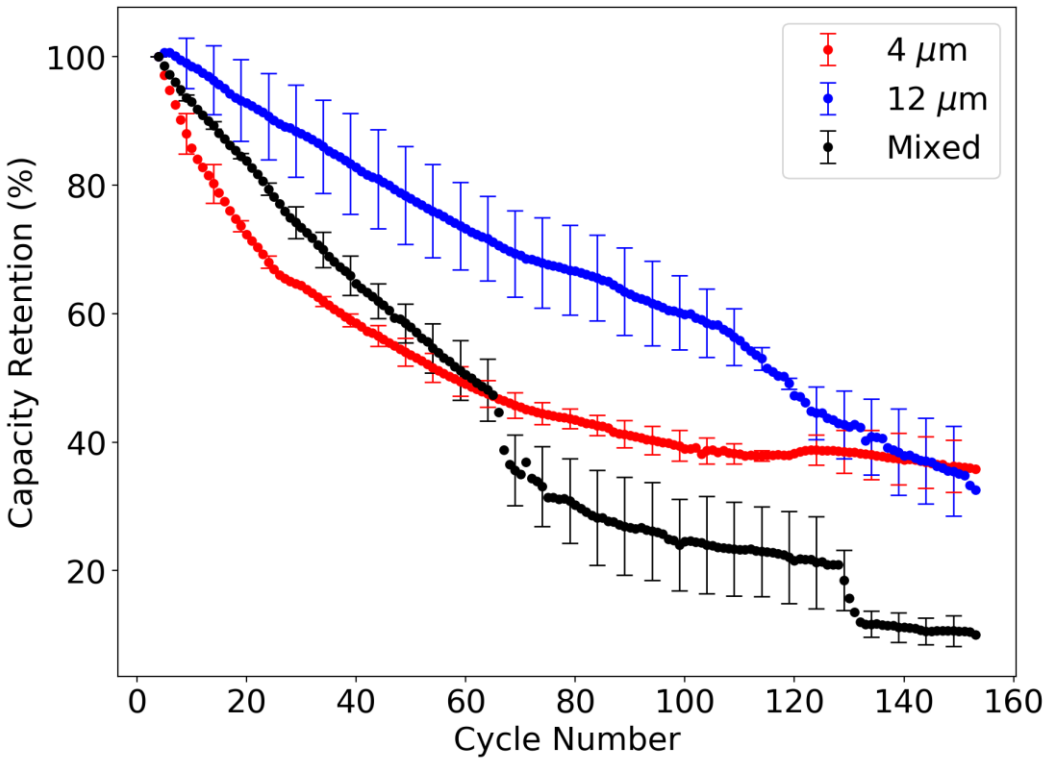


Figure 14: First 150 cycles of long-term cycling at C/3 charge and -C/3 discharge for each cell configuration. Each trend is comprised of three cells and averaged at each cycle. Error bars are provided for every 5th cycle.

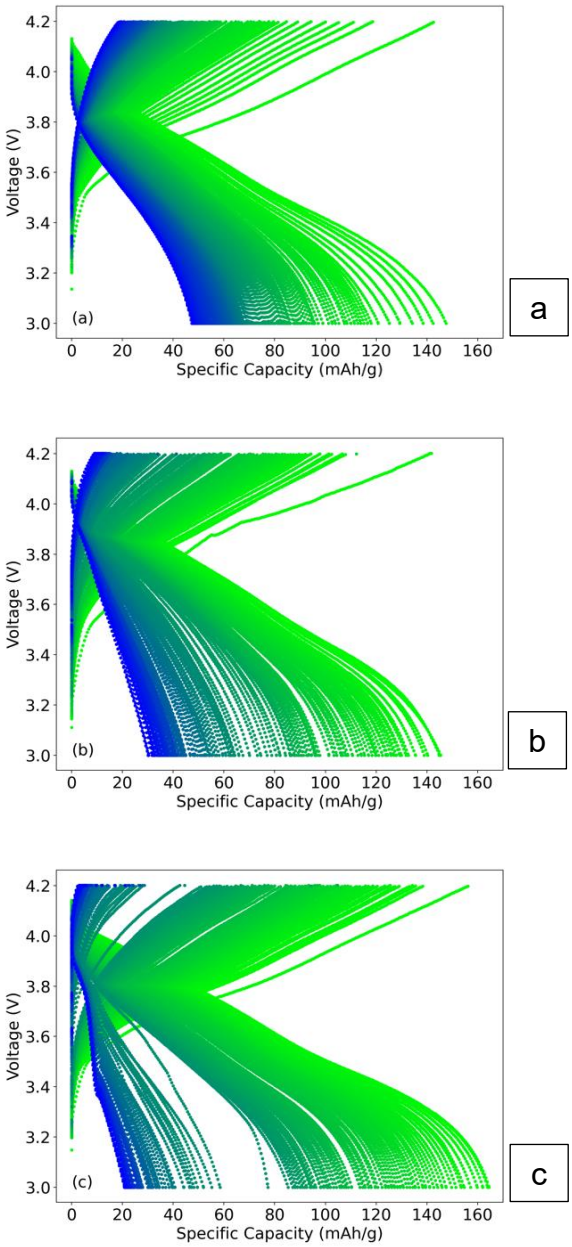


Figure 15. Capacity vs Voltage plots for each configuration during the first 150 cycles of long-term cycling at C/3 charge and -C/3 discharge. Subfigures a), b), and c) represent 4 μm: 4 μm, 12 μm: 4 μm, and Mixed: 4 μm configurations respectively. Cycles progress from light green to blue as the cell ages.

***Electrochemical Impedance Spectroscopy***

Nyquist plots for each full cell configuration are shown in Figure 16 (a-c). In each configuration the mid to low frequency impedance contribution increases and can be attributed to the charge transfer resistance of the cathode. [184-186] At lower frequencies a 45 degree line, attributable to Warburg impedance in the electrode pair, accounts for slow diffusion between electrodes. [185] This diffusion is comparable for all electrode configurations. In each electrode, bulk resistance attributed to the connections, electrolyte, and inactive components such as current collectors, is observed to increase slowly as the cell ages, likely due to electrolyte consumption. The notable difference in each cell configuration is the increase in the mid to low frequency, second semi-circle. This impedance contribution can generally be attributed to cathode charge transfer resistance and increases as the cell ages for all three configurations. This increase provides evidence of a passivation layer that leads to a reduction in kinetics at the active material surface-electrolyte boundary. [115] These increases in charge transfer resistance appear to be related to surface area as the impedance increase is most prominent in Figure 16 (a) for the 4μm:4μm configuration, followed by Figure 16 (c) for the mixed:4μm configuration, and finally Figure 16 (b) for the 12μm:4μm configuration. This is the same order for electrode surface area, lending more evidence to a passivation layer forming on the active material surface, a phenomenon previously reported in literature NMC materials processed with phosphoric acid. [47] Symmetric cathode cells were constructed to further investigate this behavior and are covered in the next section. Although poor cycle life of ultra-thick

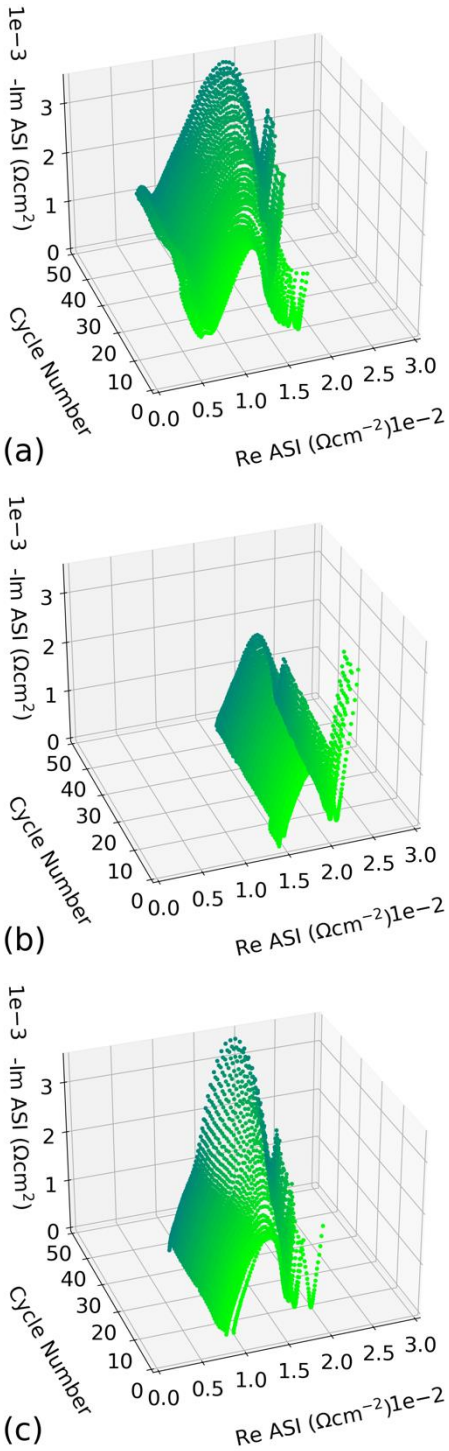


Figure 16. Nyquist plots of each full cell configuration as a function of cycle life a), b) and c) correspond to 4 μm:4 μm, 12 μm:4 μm, and mixed:4 μm respectively.

electrodes is generally attributed to the mass-transport limitations that are inherent to thick electrodes, this result shows that the interaction can be more complex. Although mass-transport limitations are likely a dominant factor, the formation of a passivation layer on the active material surface expedites the capacity fade and should be investigated further.

***High-Rate Discharge Capacity***

After initial acceptable performance for ultra-thick electrodes at lower discharge rates, the useable capacity decreases considerably between discharge rates of C/2 and 1C as seen in Figure 17 and Figure 18. Low discharge capacity at high rates is expected for ultra-thick electrodes and has been previously reported. [158] The general trend of capacity reduction as the discharge rate is increased matches results previously reported from this group for 8 $mAh/cm^2$ aqueous processed batteries. [14] A 50 % (22 mAh/g) increase in discharge capacity at 1C discharge rate is seen by moving from an all small particle configuration (red) to a configuration with a mixed particle size distribution in the first coating layer (black). As the main difference between these cells is the cathode material nearest the current collector, it can be inferred that the differences in ionic resistance and mass-transport ability throughout the electrode is the driving factor. As the discharge rate is increased, the diffusion time and length become increasingly important. The decrease in available capacity from the red to black bars, indicates that there is not enough time for the lithium-ions to travel throughout the electrode at these rates. Interestingly, cathode configuration with only large particles near the current collector (blue), displays a

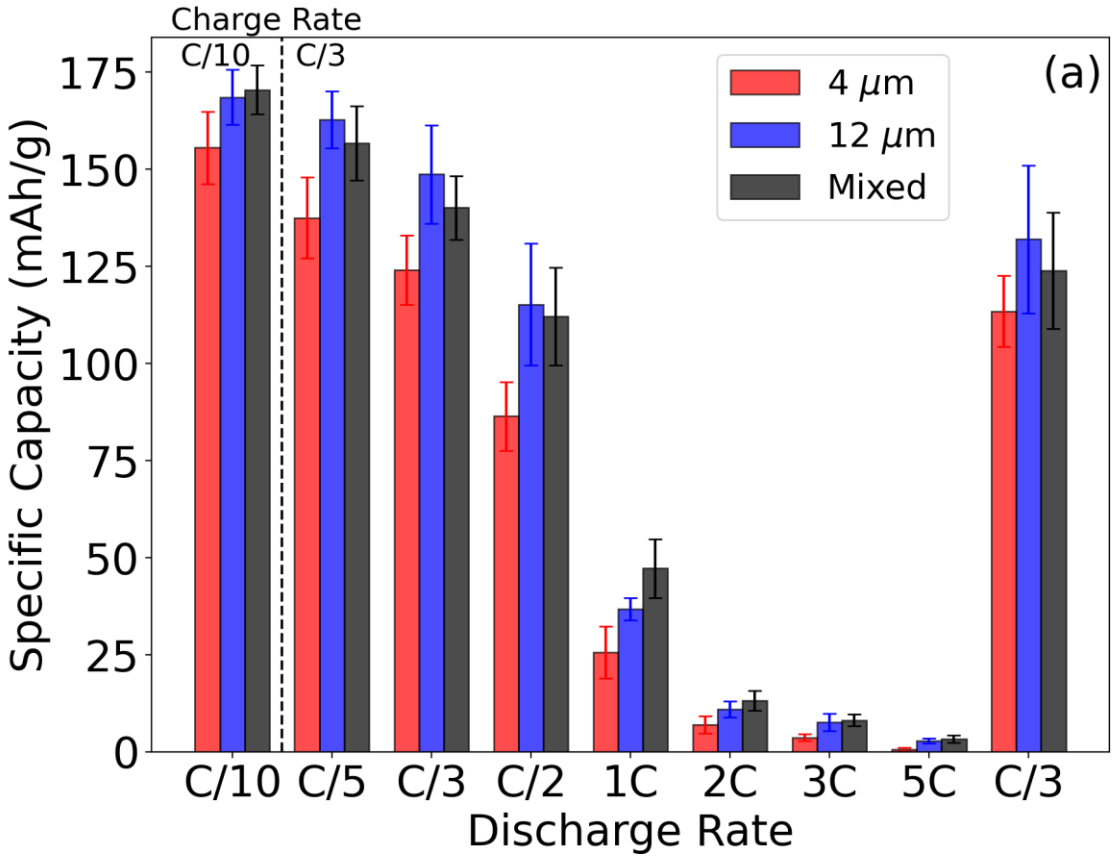


Figure 17. Average maximum discharge capacity of each cell configuration during rate capability testing. Each bar represents three batteries with each battery performing three cycles at each discharge rate for a total of nine individual data points.

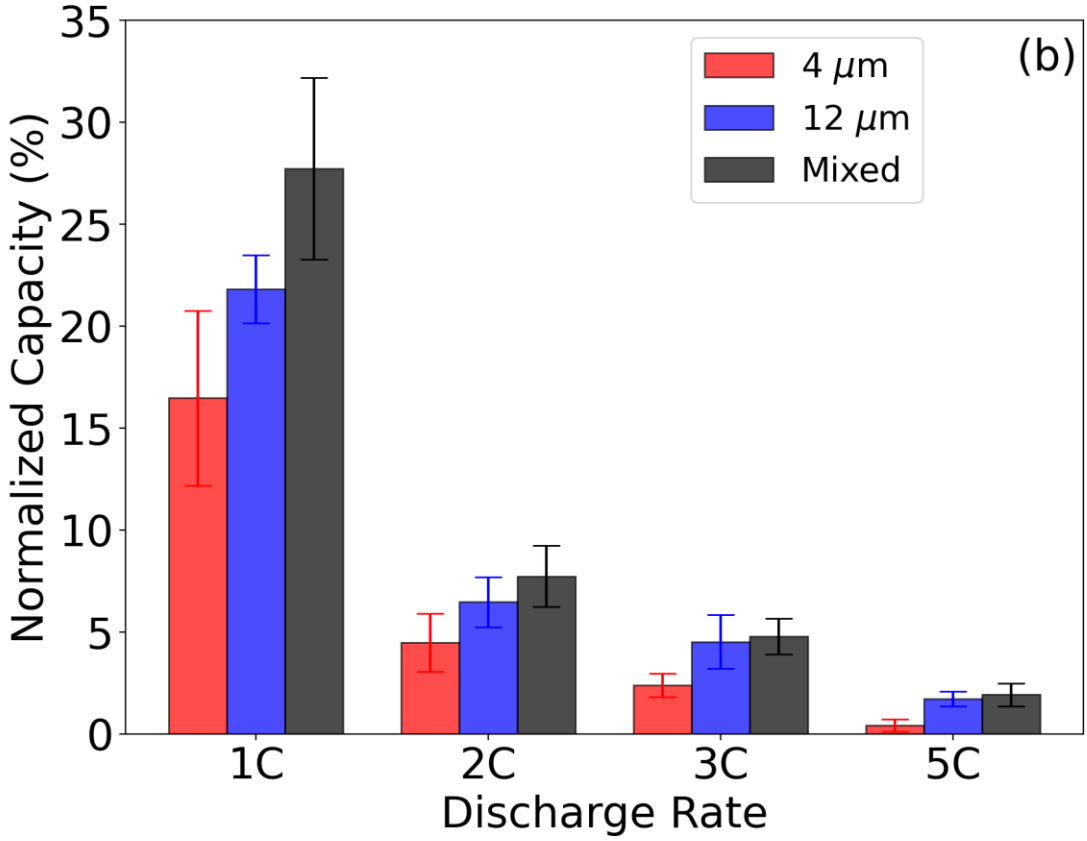


Figure 18. Normalized capacity for each cell configuration from 1C – 5C.

discharge capacity between that of the all small particle (red) and mixed (black) electrodes at most discharge rates. The two configurations are very comparable across the entire range investigated, with the black trend showing more significant improvements at higher discharge rates. This suggests that the less constrictive pore network near the current collector within the large particle sample facilitates quicker ion transport throughout the bottom half of the electrode but as some smaller particles are added, the increased electroactive area can still increase the cell performance without consequence. This also suggests there exists a critical surface area where the added electro-active area is no longer beneficial and the increase in ionic resistance is more significant than the increase in interaction sites.

The decreased high-rate performance exhibited by the cathode with all small (red) is likely due to decreased active material utilization as a result of more constrictive pore networks and the resulting limitation of ion diffusion through the electrode. The lithium-ions are not able to efficiently navigate the pore network and in effect cannot reach the intercalation sites near the current collector. As the particle size decreases, the lithium-ion diffusion length increases and effectively decreases porosity and constricting ionic movement. This effective porosity decrease results in underutilization due to higher polarization and subsequently lower capacity. [162] This again points to the existence of an optimal combination of large and small active material particles in the first coating layer of somewhere between 0 and 50 wt% small particle active material. The best performing sample was the mixed electrode near the current collector and is due to the combination of

moderate lithium-ion diffusion path length and increased active material surface area. The increased intra-particle interaction combined with moderate inter-particle interaction provides a net improvement in discharge performance at high rate. This suggests the performance of the electrode should consider not only the porosity as previously reported, but also the electroactive area which impacts both the porosity/tortuosity as well as the utilization throughout the electrode.

***Symmetric Cells***

Symmetric cells were constructed to determine differences in ionic diffusion primarily associated with the liquid electrolyte in the porous electrode. Two variations of symmetric cells were tested, one with cathodes discharged to 50% SOC (3.6 V) and the other with cathodes fully discharged to 0% SOC (3 V). These two states of charge were used as electrode-based charge transfer contributions can be observed in the 50% SOC cell in electronic blocking configuration (constructed with separator). By constructing an identical cell at 0% SOC, the charge transfer contribution is suppressed, and the ionic resistance can be isolated from the greater signal. Nyquist plots from cells assembled at 50% SOC and 0% SOC are shown in Figure 19 and Figure 20 respectively.

A clear increase in charge transfer resistance associated with the cathode can be seen in Figure 19 as the particle size is decreased. These differences are associated with surface area differences as the cathode with the largest surface area exhibits the largest charge

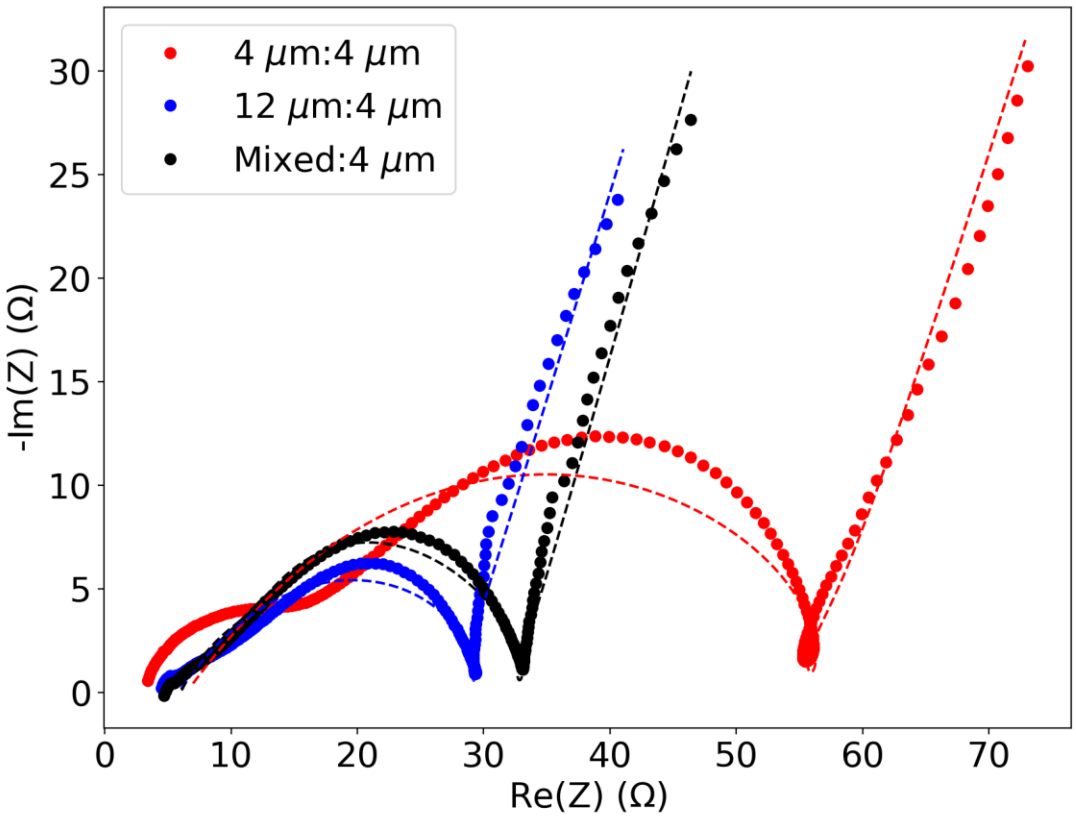


Figure 19: 50% SOC symmetric cathode Nyquist plots for each cathode configuration. The differences in charge transfer resistance as the surface area of each electrode increases provide further evidence of a charge blocking CEI layer on the cathode active material.

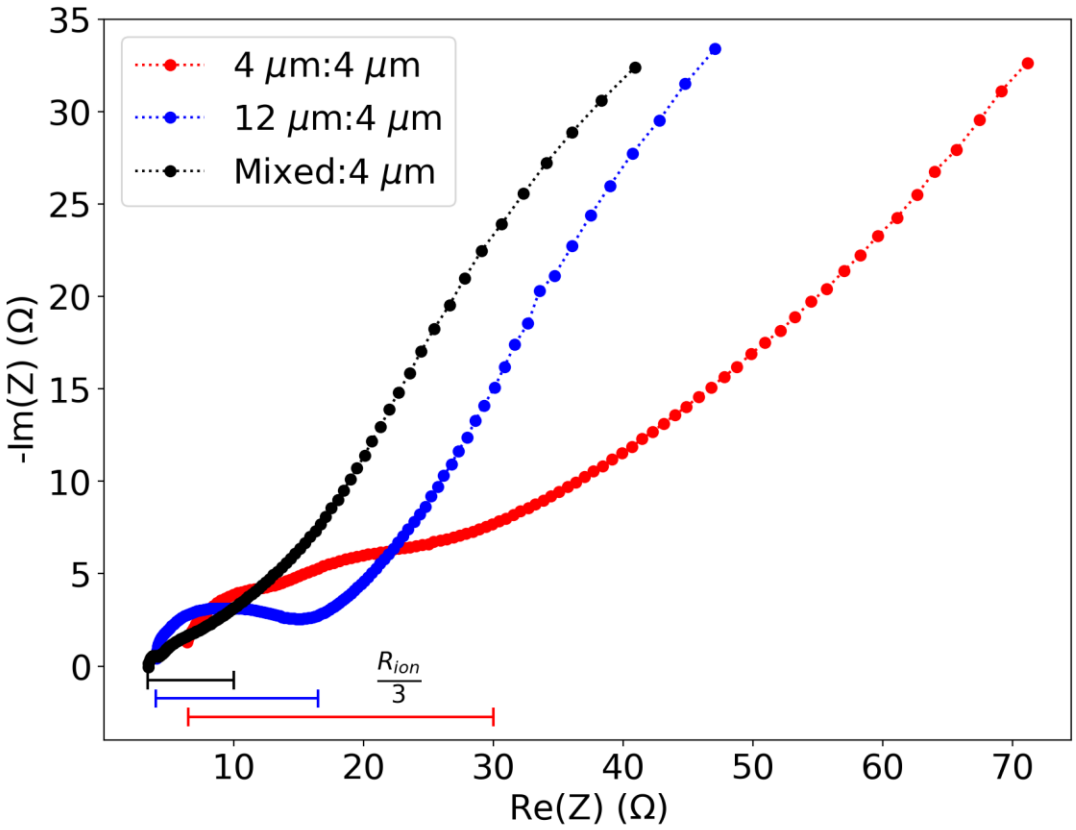


Figure 20: 0% SOC symmetric cathode Nyquist plots for each cathode configuration. The ionic resistance as described in literature is shown in the horizontal bars. [187] The increase in ionic resistance as the particle size decreases suggests the increased packing density results in a more constrictive pore network that result in decreased diffusion throughout the electrode

transfer resistance and the cathode with the smallest surface area exhibits the lowest charge transfer resistance. This result further supports the previous assertation of an unstable CEI developing on the active material particles. Another likely explanation for this increase in resistance is the overall mass-transport limitations that exist in high areal loading electrodes. As the lithium-ions are shuttled, it is more difficult to move throughout the smaller (red) active material pore network. A model cell developed by Chen and coworkers was used to determine the charge transfer resistance of each symmetric cell and the resulting calculated values are shown in Table 5. [185] Notably the charge transfer resistance increases near two-fold (28.35 Ω to 57.37 Ω) from the 12 μm: 4 μm trend (blue) to the 4 μm: 4 μm trend (red), suggesting the coating near the current collector plays a large role in available capacity especially at high cycling rates. This is further evidenced by the mixed:4μm trend (black) exhibiting a charge transfer resistance similar to that of the 12 μm:12 μm trend (33.64 Ω and 28.35 Ω respectively) suggesting a non-linear dependance on surface area, which is a known characteristic of diffusion-based resistance. [162] It is therefore thought the increase in charge transfer resistance observed in Figure 19 is primarily due to liquid phase ionic transport limitations but is also impacted by increased side reactions at the active material surface.

Further, as shown in Figure 20, the ionic resistance associated with each cathode configuration provide similar results. As the cells were discharged to 0% SOC, it can be inferred that little to no charge transfer occurs between the electrolyte and active material in these cells. Therefore, the impedance shown in Figure 20 is that of ionic resistance of

Table 5: Fit parameters for symmetric cathode cells based on a model cell proposed by Chen and coworkers. [185]

| Coating | 4 μm : 4 μm | 12 μm : 4 μm | Mixed : 4 μm |
|---|---|---|---|
| $R_{Solution}$ | 1.03 Ω E-23 | 1.43 Ω E-16 | 1.78 Ω E-25 |
| $R_{Surface\ Film\ 1}$ | 0.68 Ω | 2.61 Ω | 2.82 Ω |
| $C_{Surface\ Film1}$ | 1.44 F | 12.29 F | 3.34 F |
| $R_{Surface\ Film\ 2}$ | 5.80 Ω | 3.24 Ω | 3.19 Ω |
| $C_{Surface\ Film\ 2}$ | 7.26 F | 1.46 F | 6.24 E-3 F |
| $R_{Charge\ Transfer}$ | 57.37 Ω | 28.35 Ω | 33.64 Ω |
| $Q_{Charge\ Transfer}$ | 0.02 F | 4.40 E-3 F | 2.20 E-3 F |
| $\alpha_{Charge\ Transfer}$ | 0.45 | 0.47 | 0.57 |
| $Q_{Diffusion}$ | 1.61 F | 2.03 F | 1.97 F |
| $\alpha_{Diffusion}$ | 0.70 | 0.71 | 0.72 |

the electrolyte. The ionic resistance of the all small active material configuration (red) is considerably larger (2X and 4X) than that of the large and mixed variations (blue and black, respectively). As the charge transfer component is suppressed, these differences are attributable to ionic resistance in the electrolyte and demonstrate the effective diffusion length increase produced by a more constrictive pore network. [187] This is in good agreement with the inference from 50% SOC cells and provides direct evidence of the importance of the liquid diffusion throughout the electrode. Ideally the high frequency limit of a 0% SOC test would be the ionic resistance, however as these cells were discharge and held at 0% SOC, relaxation can occur after the polarization is removed resulting in partial lithiation and a high frequency signal that is not entirely asymptotic. This does not alter the ionic resistance determination as the inflection point is used to differentiate contributions. This provides increased support for the capacity fade at high discharge rates. As the ionic resistance of the electrolyte is a consequence of the pore structure.

***Diffusion Coefficient Determination***

Calculated diffusion coefficients as a function of lithiation (bottom x-axis) as well as state of charge (SOC) (top x-axis) are shown for charging and discharging in Figure 21 (a) and (b) respectively. As the diffusion coefficient varies by approximately an order of magnitude over the lithiation range, Figure 21 (a) and (b) both contain inserts depicting the differences in further detail. After initial changes at low lithiation values, the diffusion coefficients generally decrease as the state of charge increase, implying as the cathode material accepts

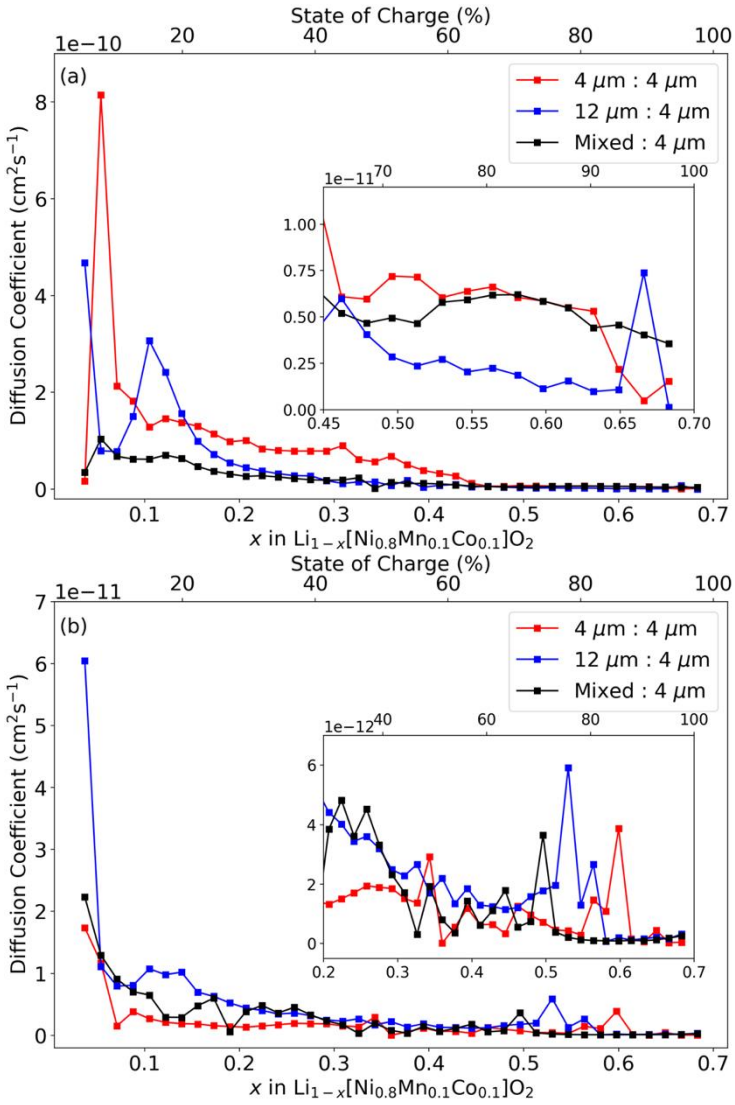


Figure 21. Solid diffusion coefficient for a) charge and b) discharge cycles of each electrode configuration.

more lithium-ions, it becomes increasingly difficult to add more. The values reported here are in agreement with order of magnitude estimations from other studies. [70] As this measurement relies on potential relaxation after charge or discharge, it is indicative of the solid diffusion in and out of the active material particle. Thus, the differences in active material particle size used, either 4 μm:4 μm (red), 12 μm:4 μm (red), or mixed:4 μm (black), does not appear to have a pronounced impact on the solid diffusion of the cathode. This is to be expected as all active material sizes used were branded as the same chemical composition, only with a difference in average particle size. The BET surface area and tap density of each particle size was used as well as calculated molar volume in order to calculate the diffusion coefficient, these values are listed in Table 6. As the solid diffusion behavior seems to be consistent across active material particle sizes, the main contribution to rate performance differences appear to be the increased ionic resistance due to the more constrictive pore network developed with smaller particle sizes. This technique was only measured only the course of one charge discharge cycle and therefore is not minimally affected by the unstable CEI layer identified previously.

## Conclusions

Both the mechanical and electrochemical performance of three electrode configurations produced with two cathode active material particle sizes were investigated. Reported are electrodes that are generally mechanically robust, but with increased adhesion as the contact area between the current collector and the bottom of the cathode material is

Table 6: BET surface area, tap density, and molar volume values used to calculate the diffusion coefficient for each configuration. BET surface area and tap density values were provided by the manufacturer whereas the molar volume was calculated from available molar mass values reported in literature. [188]

| Parameter | 4 μm Particle Size | 12 μm Particle Size |
|---|---|---|
| BET Surface Area | 7600 $cm^2/g$ | 4900 $cm^2/g$ |
| Tap Density | 1.94 $g/cm^3$ | 2.31 $g/cm^3$ |
| Molar Volume | 50.15 $cm^3/mol$ | 42.12 $cm^3/mol$ |

increased. It is thought the increased area lends to more binder/current collector contact. The fact that the adhesion does not drop, suggests a sufficient amount of binder exists such that it is not distributed too thinly across the increased area. By analogue, it implies the binder content for other electrodes could be decreased without sacrificing mechanical performance. Rheological measurements support this notion as the storage modulus of the smaller active material particle dispersion far exceeded that of the larger active material particle. Likely driven by a combination of electro-steric force stabilization and superior dispersion, this could be beneficial for high-speed coating applications so long as the viscosity of the dispersion is not too great.

Electrochemically, the electrodes offered comparable, but poor cycle life in all cases. After further investigation via EIS, it was identified that the aqueous processed cathode material likely develops an unstable CEI layer that results in increased electrolyte consumption. This is only exacerbated as the surface are of the electrode is increased. This in combination with the increased mass-transport limitations shown to exist in these ultra-thick configurations leads to a cycle life that underperforms its NMP based counterpart. High-rate discharge capacities were improved by 50% at 1C with proper tuning of the active material distribution in the cathode. This provides strong evidence that not only does the pore network play a key role, but the available surface area of the electrode is also highly important. Our results suggest the optimal cathode structure should contain both small and large active material particles near the current collector and only small active material particles near the separator. Future investigations should investigate not only additional

ratios of small and large particles but should also investigate the ratio of the layer thicknesses as only one ratio (50%/50%) was investigated here.

Ionic resistance in the electrolyte, and by analogue lithium-ion diffusion throughout the pore network, was identified as the primary sources of capacity loss as the discharge rate was increased. By investigating the impedance with symmetric cells discharge to 0% SOC and suppressing the charge transferer between the electrolyte and active material particle, the increased impedance can be attributed primarily to the liquid phase diffusion. This is supported by independent solid diffusion measurements over a wide range of lithiation. The solid diffusion as a function of particle size does not appear to be a large factor in overall performance of the cells and therefore is incapable of explaining the large performance differences observed in various other measurements.

This investigation identified a promising path forward for aqueous processed ultra-thick cathodes and illustrated the importance of considering not only the lithium-ion diffusion throughout the pore network, but also the electroactive within the cell. Results provided here will inform future investigations into additional cathode configurations seeking to further optimize the mechanical and electrochemical performance of environmentally benign electrodes.

# CHAPTER V
# DRYING PARAMETER OPTIMIZATION AND BINDER MIGRATION DETERMINATION IN CATHODES

A version of this chapter will be submitted for publication by Alexander J. Kukay, Emily Bott, Anton Ievlev, Georgios Polizos, and Jianlin Li:

My contributions to this paper as lead author were 1) performing a literature search to support the topic of investigation and provided background for the project, 2) development of test matrix and protocols 3) sample testing and preparation, 4) data analysis and subsequent conclusions. Research support was provided by Emily Bott and Georgios Polyzos. Anton Ievlev provided ToF-SIMS data and analytical support. Jianlin Li provided analytical support as well as assistance in project development and revision.

## Abstract

Lithium-ion battery (LIB) electrodes are typically produced with N-methyl-2-pyrrolidone, a toxic solvent that is a known carcinogen and reproductive hazard. In response, aqueous processing has been an expanding area of research interest in the field of LIB production. Although aqueous processing has been widely successful in anode processing, serious challenges remain in processing the cathode. In this work the drying mechanics of cathode processed with both solvents is investigated though implementation of a chemical engineering based model to better understand the utilization of heat provided by experimentally determining the heat and mass transfer coefficients as well as electrochemically to determine the impact of drying temperature on cycling performance. Binder distribution is also determined via ToF-SIMS to confirm differences in binder homogeneity as a function of both solvent and drying temperature. Identified is the large difference in the efficiency in which the heat is used as well as an ideal drying temperature for both aqueous and non-aqueous processed cathodes. Also identified is the increased sensitivity to processing temperature for aqueous processed electrodes compared to non-aqueous processed counterparts.

## Introduction

Lithium-ion batteries (LIBs) have become important in various aspects of everyday life and are key to reducing greenhouse gas emissions due to fossil fuel burning vehicles. [37] Although many processing and materials improvements have been implemented since the market adoption of conventional LIBs, electrode drying and the associated physics of particles, are still far from optimized. [189] With the overall environmental impact of LIBs replacing internal combustion engines (ICEs) having become obvious over the past few decades, less discussed is the environmental impact of producing LIBs. The environmental and ethical considerations around production, especially on a large scale, of LIBs targeted for transportation should be paramount. Judicious choice of both material and methods to minimize environmental impact should be prioritized so long as electrochemical performance and mechanical integrity are not compromised. Research has shown global warming potential associated with production of LIBs, and has identified solvent replacement in both the cathode and anode as a an avenue for improving the total environmental impact of LIBs during both production and recycling phases. [18] The common organic solvent of choice for LIBs, N-methyl-2-pyrrolidone (NMP), is toxic, expensive, and in some countries restricted and thus a good candidate for replacement both environmentally and economically. [12, 95] As positive electrode manufacturing has been identified as a disproportionately large contributor to overall environmental impact, this work focuses on optimization of cathode manufacturing, specifically energy input during the energy intensive drying period. [8]

Investigating electrode drying poses a technically difficult endeavor due to the difficulty of measuring dynamic particle motion as well as the existence of a wide range of length scale participating in the diffusive and convective motion. [98, 189] Regardless of the difficulty associated with measuring particle motion, the drying phase of electrode processing has a large impact on final performance. [95, 97-102] During the particulate coating drying process, three main forces must be considered. First evaporation of the solvent from the sample surface drives a consolidation front and results in a continually changing film thickness and consequently, is a dynamic area of interest. [100] Secondly, thermal Brownian diffusion of the particles results in randomly distributed particles and counteracts potential concentration gradients. Third, sedimentation effects are observed when the density of the particulate surpasses that of the solvent. The combination of all three of these forces heavily influence the resulting pore network in particulate coatings, such as porous electrodes used in LIBs and can be visualized in Figure 22. [99, 103]

Throughout the electrode production process, great care is taken to ensure homogenous distribution of material within the dispersion. [102] There is a wealth of research concerning optimization of the mixing processes available in literature and the impact of mixing conditions, times, and techniques on final dispersion behavior. [2, 28, 42, 43, 154, 190] As the importance of a well distributed combination of active material, conductive additive, and polymetric binder is clear, a strong understanding of how the distribution of these materials varies as the solvent is removed is paramount. During this process the

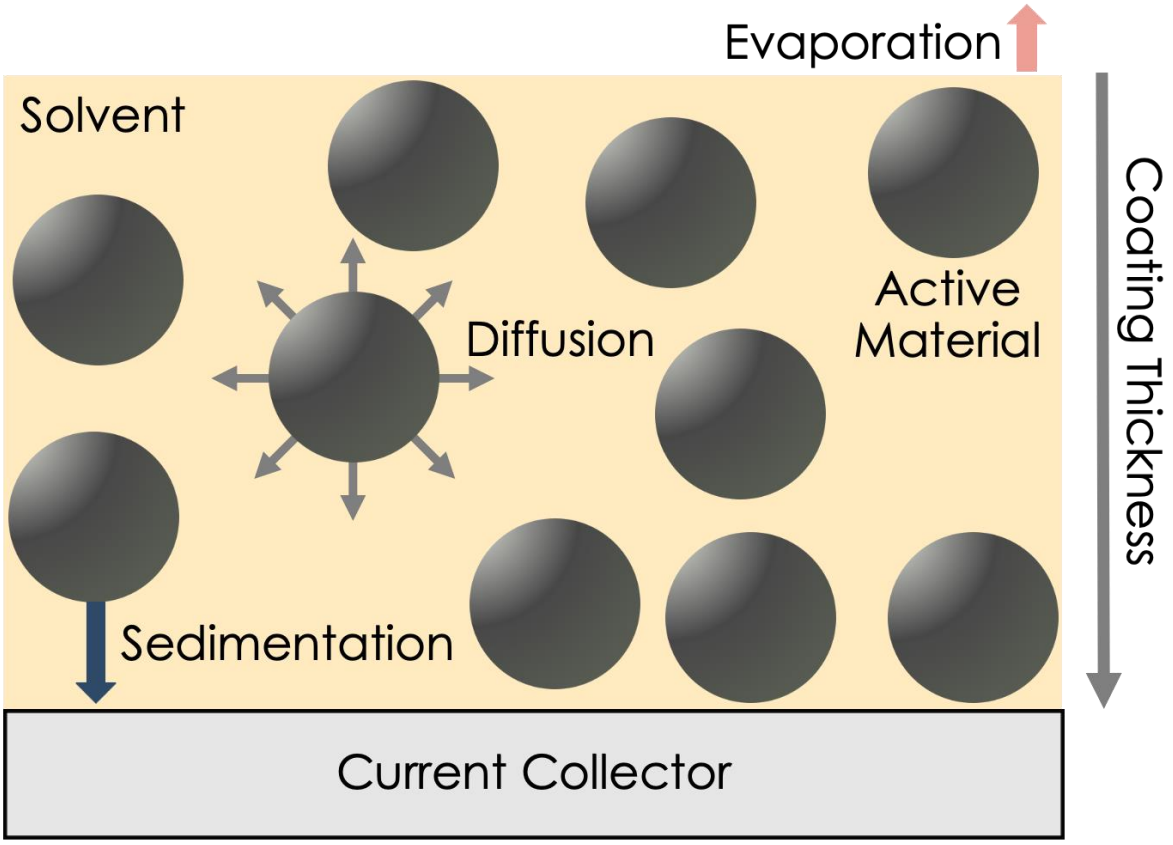


Figure 22: Film shrinkage stage of electrode drying. Diffusion driven by Brownian motion, sedimentation, and evaporation driven capillary action all contribute to final pore geometry and film consolidation. AM represents the large active material particles that eventually create the porous electrode structure.

most important factor is the solvent, as the viscosity and evaporation behavior dominate the redistribution of materials within the electrode during drying. [102]

Typical electrode dispersions are either coated via doctor blade for laboratory scale or slot die coater for pilot and industrial scale. These coatings are typically a thickness on the order of hundreds of microns. In combination with the fact that electrodes are typically on the order of many square centimeters to many square meters in area, they can be accurately treated as thin films from a coating and drying perspective. [102] Accordingly, two main drying phases exist. First the solvent evaporation results in larger particles compacting and forming the basis of the electrode structure, this is commonly referred to as *film shrinkage*. [101] Consolidation continues until the larger active material particles can no longer be compacted by evaporation of solvent. The drying behavior is then more accurately described by a *pore emptying* stage where excess solvent is removed from the previously formed porous electrode, this second stage comprises the bulk of time and energy input during drying. [101, 102] Smaller conductive additive and polymetric binder particles still experience significant mobility at this stage and there is still sufficient solvent in the electrode system. These smaller particles experience transport through the beginnings of the electrode structure via Brownian motion due to the thermal energy of the electrode system as well as capillary action driven by the evaporation at the electrode surface. The transport of binder polymer chains dissolved in solution via diffusion is greater during the initial stage of drying that it is during the final, longer stage of pore emptying. [98, 99, 101]

Along with the mechanical implications of drying parameters, there also exist economic drivers to optimize the drying time and energy input. As the production phase of LIBs accounts for the majority of the overall cost, almost half of that cost results from drying and solvent capture related processes. [72] By optimizing the time and energy required for drying, both capital and energy costs may be decreased, resulting in a more cost-effective processing technique and ultimately a more affordable battery. [10] As the typical solvent NMP and prospective replacement solvent, deionized water (DI) have considerably different vapor pressures, 1.0 mm Hg at 40 ℃ compared to 55.3 mm Hg at 40 ℃, and boiling points 204.3 ℃ and 100 ℃ respectively, the energy required as well as the rate of evaporation during electrode drying vary widely. [10] NMP does however have a lower heat of vaporization than water, 510 kJ/kg, as opposed to 2260 kJ/kg for water, posing an economic advantage in the form of energy input for NMP use. These values are listed in Table 7. This advantage is quickly negated when the toxic nature and legal limitations of NMP are factored in. [11] Solvent replacement for anode chemistries, typically composed of graphite, has seen commercial success and is widely used in current manufacturing methods. Cathode chemistries have not enjoyed the same level of success, largely due to a proton exchange reaction driven by lithium leaching from the active material particles into solution which leads to a highly basic environment. [13, 14] There is an abundance of research activity surrounding aqueous processing of cathode materials, but there are still concrete barriers to be overcome. [13-15, 28, 34, 47, 150, 191]

Table 7: Properties of interest for both DI water and NMP solvents.

| Solvent | Vapor Pressure (mm Hg, 40 ℃) | Boiling Point (℃) | Heat of Vaporization (kJ/kg) |
|---|---|---|---|
| DI | 55.3 | 100.0 | 2260 |
| NMP | 1.0 | 204.3 | 510 |

There have been numerous studies addressing drying parameters, mainly in conventionally processed (NMP processed) anodes. [97-100] However, there is little information concerning cathode drying, especially as a function of solvent used, that is available in the literature. Previous investigations have detailed techniques for determining binder distribution as a function of drying condition and provided some insight on the electrochemical performance differences that are associated with high and low drying rates. [99, 107] Stein and coworkers investigated the impact of multiple drying rates on positive electrodes processed with NMP and found the drying rate, primarily in the beginning stages, has a large impact on final electrode structure. [102] Baunach et al investigated adhesion differences associated with drying temperatures in anodes, concluding adhesion decreased with increasing drying temperature. [96] The authors conclude the reduction in adhesion is due to the increase in binder concentration near the surface of the electrode thus resulting in an inferior binding surface near the current collector. Although general trends concerning binder distribution can be inferred from experiments such as adhesion testing, more difficult to obtain is a clear picture of exact binder distribution from the current collector to the surface of the electrode. To combat this, multiple groups have proposed and demonstrated mathematical models to predict binder distribution. [59, 101, 104]

In order to provide an accurate account of binder distribution throughout the electrode as a function of not only temperature, but in some cases as a function of drying time, several investigations have developed clever experimental procedures aimed at spatially resolved

binder distributions. Hagiwara and coworkers developed a method for freeze drying aqueous based graphite anodes before performing Raman spectroscopy on the samples. Using the ratio of Raman peaks associated with SBR binder and graphite, the demonstrate significant binder migration within the first 120 seconds of drying at 150 ℃. They also confirmed the temperature dependance of the binder migration phenomenon by performing the same experiment at room temperature and observing a much smaller degree of binder migration. [106] Müller and coworkers present a EDX based technique for qualitatively mapping binder distribution in NMP based anodes on both the electrode surface as well as the current collector side of the electrode. [107] Although this technique is limited to the so called “top” and “bottom” views of the electrode, it can also be applied to the cross-section of the electrode with minor modifications to the procedure. This is further explored in a future section. TGA has also been employed by Li and coworkers to analyze thinly sectioned layers of a 1500 μm thick electrode. [95] This technique is limited to ultra-thick electrodes as the removal of thin layers of the electrode poses a steep technical challenge. These are informative investigations, however the comparison between the effects of solvent and drying conditions is still an open area of interest. A primary aim of this work is to quantify the differences in both binder distribution and electrochemical performance as a function of not only drying temperature but also as a function of solvent.

This work aims to expand on the current understanding of drying mechanics in positive LIB electrodes as well as investigate the effects of solvent replacement on drying rate as well as binder distribution. Results from this work will inform the future production

methods of positive LIBs and provide further understanding on the advantages and limitations of aqueous processing of cathode materials.

## Methods and Materials

### *Sample Preparation*

Small scale dispersions were prepared by adding components in steps and mixing thoroughly using a high shear mixer (NETZSCH Premier Technologies Model 50). Before adding additional material, the slurry was checked to ensure homogenous distribution of materials in order to reduce the possibility of agglomerates. Sample compositions were limited to two formulations, one utilizing DI water (purified to 18 MΩ cm using a Milli-Q Direct 8 purifier) as the solvent and the other using the conventional NMP (Sigma Aldrich) as the solvent. Each dispersion had a solids composition of 90 wt% active material (NMC 811, Targray 12 μm), 5 wt% conductive additive (carbon black, Denka Li-100) and 5 wt% binder. Binder selection was dependent on solvent, aqueous processed dispersions utilized a composite binder made from a 1:4 weight ratio of sodium substituted carboxymethyl-cellulose salt (Arcos Organics) and an emulsion binder (JSR TRD-202A) whereas NMP processed samples used PVDF (Solvay) as the binding agent. NMP based samples were prepared with 48 wt% solids content and DI based samples were prepared with 52 wt% solids content in order to adhere to practical solids content conditions observed in production. Samples were placed on a rolling mill between tests to avoid sedimentation.

DI samples also utilized 0.5 wt% phosphoric acid to combat corrosion issues at the current collector interface as previously described in other work from this group. [14] A complete sample test matrix is given in Table 8.

***Drying Curve Acquisition***

Prepared slurries were coated on aluminum foil cut to 7.62 cm x 12.70 cm (3 in x 5 in) areas and coated entirely using a doctor blade set to either 400 μm or 750 μm wet gaps to obtain electrodes with an areal loading of 2.5 mAh/cm$^2$ and 6 mAh/cm$^2$ respectively. The resulting coatings were then placed on a weighing platform suspended from a precision balance (Mettler Toledo) for real time mass collection. As the balance has a maximum operating temperature of 40 ℃, significantly below that of the temperatures of interest in this set of experiments, a suspended weighing platform was required. This was accomplished by using a 6.3 mm accesses hole drilled through the glass support to suspend the weighing platform into a tape caster. This setup was designed to effectively emulate a typical forced-air drying condition that would be present in a slot-die coater. A schematic of this experimental setup is provided in Figure 23. A forced air heater as well as a heated bed were used in tandem to control the temperature of the sample space throughout the test. Three test temperatures were used, 60 ℃, 90 ℃, and 125 ℃. Although higher test temperatures would have been desired, the equipment was limited to 125 ℃, which is representative of commercial drying temperatures. Air flow was limited to 10 cubic feet per minute in order to reduce the variance in the reading due to turbulent air. A python

Table 8: Sample matrix of interest. Samples were prepared as one slurry and were dried at the temperatures and wet gaps shown. Samples were prepared as one slurry to ensure consistent conditions for all drying events.

| Solvent | Drying Temperature (°C) | Coating Wet Gap (μm) |
|---|---|---|
| DI | 60 | 400 |
| DI | 60 | 750 |
| DI | 90 | 400 |
| DI | 90 | 750 |
| DI | 125 | 400 |
| DI | 125 | 750 |
| NMP | 60 | 400 |
| NMP | 60 | 750 |
| NMP | 90 | 400 |
| NMP | 90 | 750 |
| NMP | 125 | 400 |
| NMP | 125 | 750 |

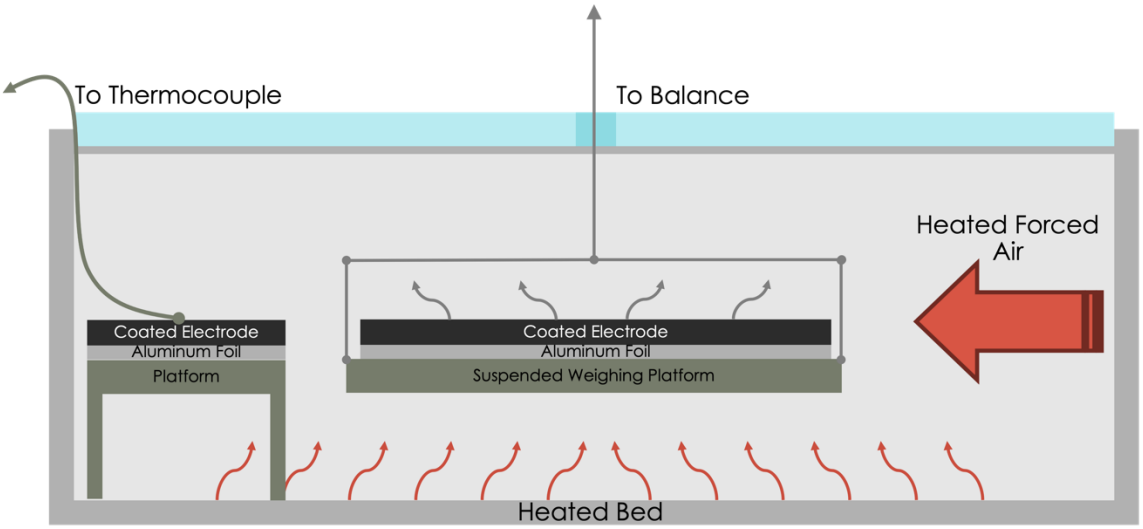


Figure 23: A schematic of the real time mass acquisition during both phases of electrode drying. A forced air heater and bed heater are used to control the ambient temperature in the tape caster and provide a uniform distribution of heat throughout the sample space. The air flow was fixed at 10 cubic feet per minute in order to reduce variance from turbulent air. Both changes in mass and temperature were recorded as a function of time via a laboratory balance and thermocouple.

script was developed to communicate with the balance on one second intervals, recording the mass with each interval. A thermocouple was used to measure the film temperature of each sample during testing. A second sample was coated and placed in close proximity to the weighing platform and the temperature of the second film was measured as to not influence the mass measurements of the initial film. Temperature measurements were collected every second for the duration of the drying period.

***Heat and Mass Transfer Coefficient Model***

Heat and mass transfer coefficients were calculated using a model developed based on chemical engineering principles. [192] First the mass transfer coefficient is calculated using Equation 8.

Equation 8: $$\boldsymbol{M(t) = M_0 - K_g \cdot A \cdot t \cdot (P_V(T) - P_0)}$$

Where $M(t)$ is the measured mass as a function of time, $M_0$ is the initial mass value, $K_g$ represents the mass transfer coefficient, $A$ is the effective area of the sample (assumed to be the volume fraction multiplied by the geometric sample area, $t$ is time, $P_V(T)$ is the solvent vapor pressure calculated using Antoine equation, and $P_0$ is the partial pressure of the solvent in air.

Along with a mass-based mass transfer coefficient, a concentration-based calculation was also used, implementing the Chilton-Colburn J-Factor analogy. This is given by Equation 9.

Equation 9: $$\boldsymbol{K_g \cdot P_V(T) = \frac{K_c \cdot P_V(T)}{R_{NMP} \cdot \mathrm{T}}}$$

Where $R_{NMP}$ is the mass specific gas constant for NMP and the concentration of NMP vapor follows the model of an ideal gas mixture presented in Equation 10.

Equation 10: $$\boldsymbol{\frac{m}{V} = \frac{P_V(T)}{R_{NMP} \cdot \mathrm{T}}}$$

The concentration-based heat transfer coefficient can then be calculated by utilizing the Chilton-Colburn J-Factor analogy shown in Equation 11.

Equation 11: $$\boldsymbol{H_c = K_c \cdot \rho_{air} \cdot C_{p,air} \cdot \left(\frac{Sc}{Pr}\right)^{\frac{2}{3}}}$$

Where $H_c$ is the heat capacity, $C_{p,air}$ is the constant pressure of heat capacity for air, $Sc$ is the Schmidt number, and $Pr$ is the Prandtl number and are calculated via Equation 12.

Equation 12: $$\frac{Sc}{Pr} = \frac{k}{\rho_{air} C_{p,air} D_{AB}}$$

Where $k$ is the thermal conductivity of air and $D_{AB}$ is the diffusivity of a volatile species in air. This value is an order of magnitude estimation and assumes low concentration of NMP in air. In other words, sufficient air flow must be present to satisfy the bounds of the model. This condition is satisfied by the air flow present in the tape caster.

***Cell Assembly and Electrochemical Testing***

Coin cells were constructed for various electrochemical tests. Coin cell format was used over pouch cells due to the space limitation of drying oven. After electrodes were dried according to the test procedure of interest, 14 mm punches were obtained, calendered to ~30% porosity, and placed in a vacuum oven at 110 ℃ overnight for secondary drying to remove excess water and avoid subsequent HF generation during cycling. [10, 65] Half coin cells were then assembled in an argon filled glovebox using 16 mm lithium chips (MTI) as the counter electrode. Cells were assembled with Celgard 2325 punched at 18 mm as the separator material and 1.2 M LiPF6 dissolved in ethylene carbonate (EC) and ethyl methyl carbonate (EMC) in a 3:7 weight ratio as the electrolyte.

To determine the electrochemical effects of drying on the resulting electrodes, rate capability, electrochemical impedance spectroscopy, and cycle life tests were all preformed on half cells constructed for each electrode. Rate capability tests involved cycling half coin

cells first at various discharge rates to observe the impact on available capacity. Cells were first charged at C/3 (1C = 190 mAh/g) for all cycles followed by discharge at C/10, C/5, C/3, C/2, 1C, 2C, 3C, and 5C. Each discharge rate had a minimum of 3 cycles per rate for statistical purposes. A minimum of three cells per configuration were used in each test for a total of nine independent data points per rate. Cycle life testing was performed at C/3 charge and -C/3 discharge for 100 cycles. Again, three cells per configuration were used in order to gain statistically significant results. All rate capability and cycle life testing was performed on a Maccor potentiostat at 30 °C in a controlled environmental chamber (ESPEC). All cells were subjected to three C/10 formation cycles prior to testing to ensure a stable solid electrolyte interphase (SEI) layer was present during testing. [69]

***Binder Distribution via EDX Spectra and ToF-SIMS***

Epoxy mounted cross-sectional samples were also used for ToF-SIMMS (IONTOF) analysis. Samples were first mounted in a two-part epoxy before grinding and polishing the surface to a 3000-grit finish. Samples were then analyzed with a 500 μm window and various dwell times to ensure sufficient signal. Binder content was ascribed to two signals, one being the positive sodium ion as the CMC polymetric binder contains sodium. The second signal used was positive cesium fluorine as both PVDF as well as the JSR acrylate binder contain fluorine. Cesium was the sputtering ion and readily reacts with the present fluorine to form $Cs_2F^+$, which was used as opposed to the $F^-$ ion signal to reduce the overall test time by utilizing only positive ion detection.

## Results and Discussion

### *Heat and Mass Transfer Coefficient Model*

The mass of each coating normalized to the first data point is shown as a function of time in Figure 24 for each configuration and temperature. Listed temperatures are the measured film temperature ($T_s$) and were used as the input of the model described previously. The data is shown as relative mass for presentation purposes and to compare the drying rates among samples, however the rate of change of the mass before normalization was used to calculate the heat and mass transfer coefficients. This was accomplished by taking the numerical first derivative of each data set with a moving window size of 50 points. Care was taken to only use the linear portion of the drying data as the model is only valid for the linear film shrinkage portion of the drying process. Accordingly, a cutoff of 500 seconds was used for each sample for consistency. The DI samples show much faster mass loss as compared to the NMP based electrodes during the first 500 seconds of drying at all temperatures. As the set temperature was increased, the rate of mass loss for all samples increased, regardless of solvent. Figure 24 indicates that the temperature sensitivity for DI based samples is greater than that of the NMP based samples. The DI samples span a range of 18 ℃ (from 32.6 ℃ to 50.0 ℃), whereas NMP based samples span 27 ℃ (41.4 ℃ to 68.0 ℃). The larger increase in film temperature for NMP samples as compared to DI samples while maintaining a lower evaporation rate is easily explained by the sizeable difference in the heat of vaporization between the two materials. Calculated values are

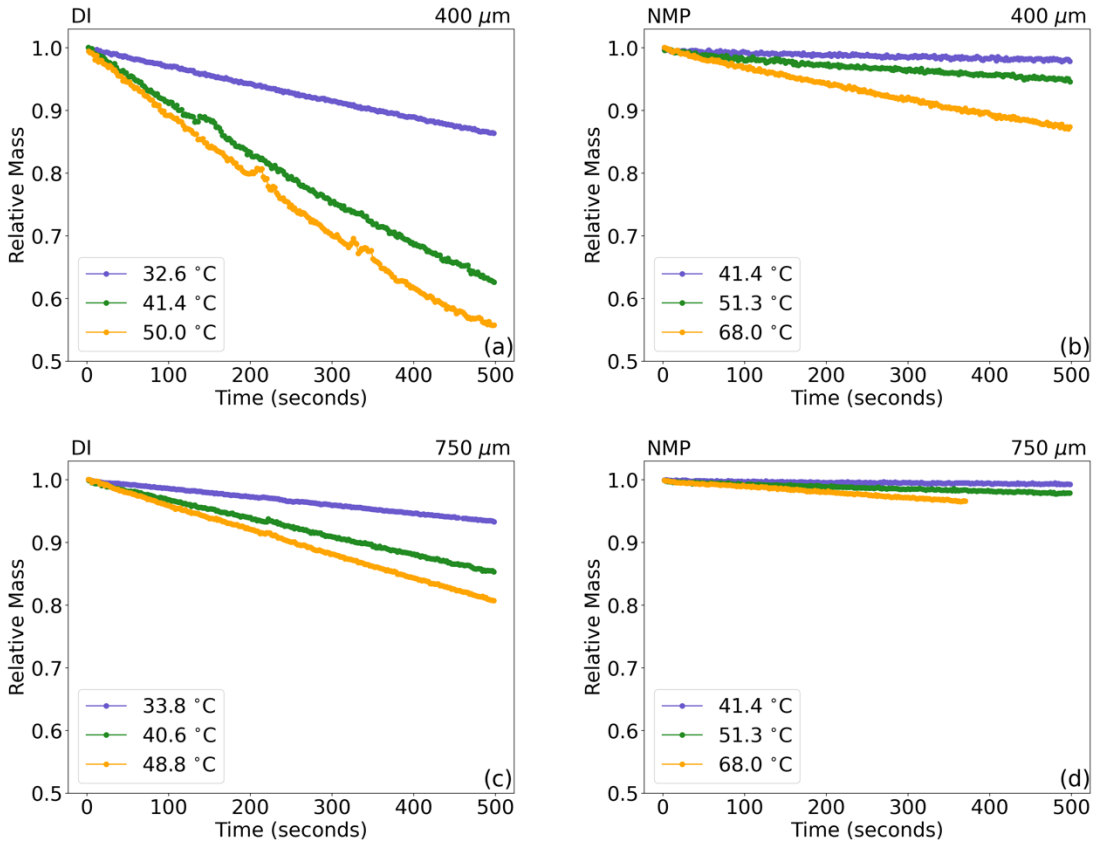


Figure 24. Experimentally measured mass time curves for a) DI 400 μm wet gap, b) NMP 400 μm wet gap, c) DI 750 μm wet gap, and d) NMP 750 μm wet gap. DI based samples exhibit much greater response to change in temperature as compared to the respective NMP sample.

listed in Table 9 and shown graphically in Figure 25. There is also a difference in the film temperature as well as film temperature deviations from the air flow as shown in Figure 26. As the set temperature is increased, it is expected that the film temperature will also increase, this relationship is shown in Figure 26 (a). However, as the temperature is increased the difference between the film temperature and the temperature of the air flow (set temperature) also increases as shown in Figure 26 (b). This difference between the set temperature and film temperature is a result of evaporative cooling and is directly related to the heat of vaporization of the solvent as well as the vapor pressure.

The faster drying rate inferred by the data in Figure 24 is further explored by calculating the heat and mass transfer coefficients for each electrode and these values are shown in Figure 25. By keeping the areas of the coatings constant, a direct comparison of the drying behavior as a function of area is made more convenient and reducing the need impact of edge effects on the analysis. As the temperature is increased the heat and mass transfer coefficients for DI based electrodes increase monotonically, reaching their maximum at the highest set temperature (125 ℃) for both coating thicknesses. The NMP samples also exhibit increases to both the heat and mass transfer coefficients, however the increase is not monotonic and increases only slightly from 90 ℃ to 125 ℃, suggesting diminishing returns as the temperature is increased further. As the heat and mass transfer coefficients are a function of the difference in film temperature and the temperature of the surrounding air, this is an expected result. However, this indicates that increasing the drying temperature for NMP based cathodes does not lead to a significant decrease in drying time.

Table 9: Heat Transfer Coefficient and Total Heat Transfer Rate values for each composition.

| Solvent | Drying Temperature (℃) | Coating Wet Gap (μm) | Heat Transfer Coefficient, $H_c$ (W/m2 K) | Mass Transfer Coefficient, $K_g$ $(gcm^{-2}s^{-1}bar^{-1})$ | Mass Transfer Coefficient, $K_c$ (cm/s) | Total Heat Transfer Rate, -q (W) | Rate of Vaporization, $\dot{m}$ (mg/s) |
|---|---|---|---|---|---|---|---|
| DI | 60 | 400 | 115.1 | 7.10E-03 | 10.0 | 30.6 | 13.5 |
| DI | 60 | 750 | 118.7 | 7.30E-03 | 10.4 | 30.2 | 13.4 |
| DI | 90 | 400 | 155.8 | 9.40E-03 | 13.6 | 73.5 | 32.5 |
| DI | 90 | 750 | 168.6 | 1.02E-02 | 14.7 | 80.8 | 35.8 |
| DI | 125 | 400 | 183.3 | 1.07E-02 | 16.0 | 133.3 | 59.0 |
| DI | 125 | 750 | 215.5 | 1.27E-02 | 18.8 | 159.3 | 70.5 |
| NMP | 60 | 400 | 3.5 | 1.20E-03 | 0.3 | 0.6 | 1.2 |
| NMP | 60 | 750 | 2.6 | 9.00E-04 | 0.2 | 0.5 | 1.0 |
| NMP | 90 | 400 | 5.7 | 1.90E-03 | 0.5 | 2.1 | 4.1 |
| NMP | 90 | 750 | 5.4 | 1.80E-03 | 0.5 | 2.0 | 3.9 |
| NMP | 125 | 400 | 6.1 | 2.00E-03 | 0.6 | 3.4 | 6.7 |
| NMP | 125 | 750 | 5.9 | 1.90E-03 | 0.5 | 3.3 | 6.5 |

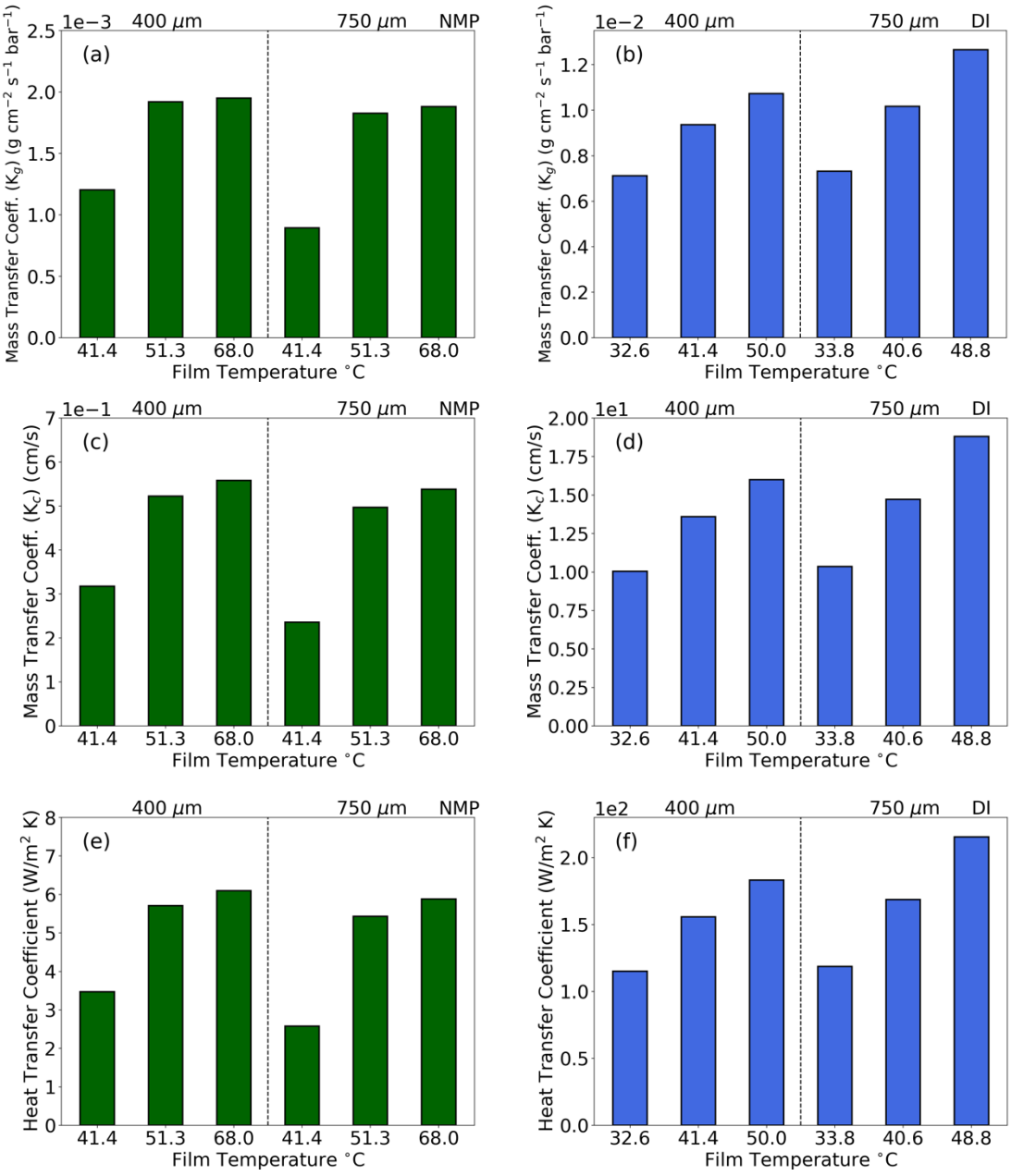


Figure 25. Calculated mass-based mass transfer coefficients ($K_g$) for a) NMP and b) DI based samples as well as concentration-based mass transfer coefficients ($K_C$) for c) NMP and d) DI based samples. Heat transfer coefficients ($H_C$) are given for e) NMP and f) DI samples.

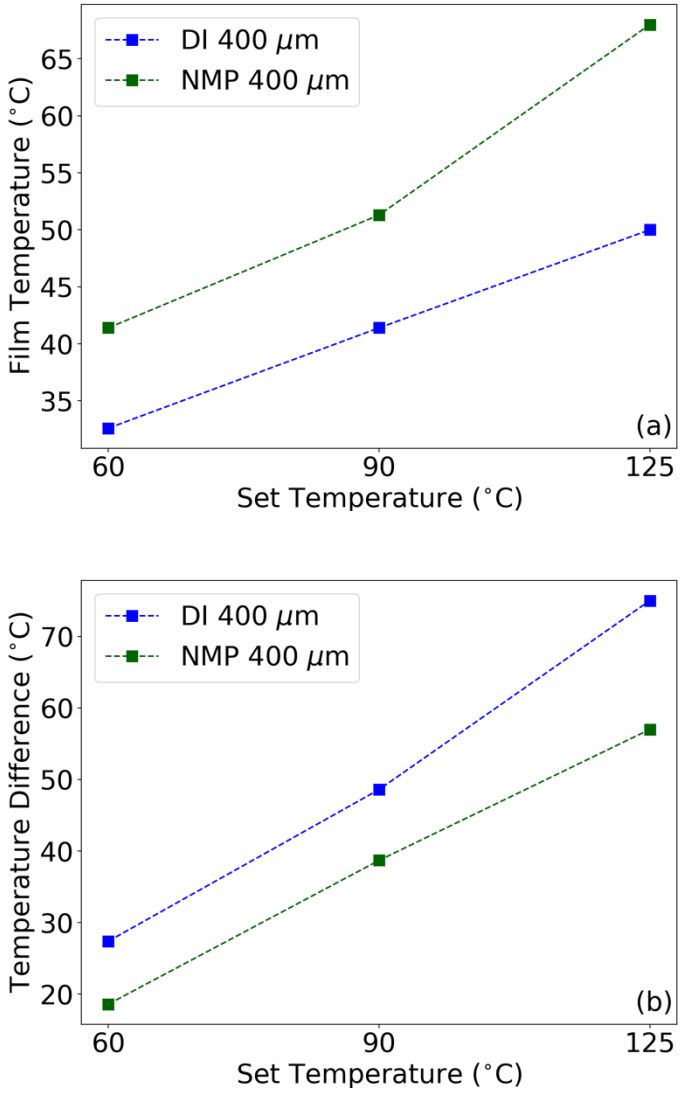


Figure 26. Measured film temperatures at each temperature set point (a) and the differences between the film temperature and set temperature (b) for DI and NMP 400 μm wet gap samples at each set temperature.

Furthermore, the calculated mass transfer coefficients for the DI based electrodes are an entire order of magnitude greater than the NMP based electrodes across all temperatures. This suggests the DI samples utilize the applied heat more efficiently as compared to the NMP samples. The difference in heat transfer coefficients is greater yet at two orders of magnitude larger from NMP to DI across all samples.

To further explore the relationship of drying temperature to the drying efficiency of each electrode the total heat transfer rate per unit area ($q$) in terms of Joules per second was determined via Equation 13 where $T_s$ is the measured film temperature, $T_\infty$ is the temperature of the surround air, $H_C$ is the calculated heat transfer coefficient and $dA_s$ represent the infinitesimal unit area. As the area used was constant across samples this simplifies to Equation 14 where $A_s$ is now the nominal surface area of the electrode. [192] Here a negative sign is introduced to reflect the physical nature of the phenomenon. In this scenario it is beneficial to have a positive value for the total heat transfer rate and thus reflect the total heat transferred to the electrode during the drying process in terms of Joules per second.

Equation 13: $$q = (T_s - T_\infty) \int_{A_s} H_C \cdot dA_s$$

Equation 14: $$-q = -(T_s - T_\infty) \cdot H_C \cdot A_s$$

The total heat transfer rate is shown in Figure 27 and illustrates the energy input as a function of time for each sample. A higher heat transfer rate suggests a more efficient use of the energy input into the system, providing further support for the argument that DI as a solvent uses the heat supplied more efficiently than NMP. Not only is the total heat transfer rate two orders of magnitude greater for DI samples as compared to NMP, the increase from each temperature is more significant. This is most clear when comparing set temperatures of 90 ℃ and 125 ℃. The total heat transfer rate for the NMP samples increases from 2.0 W to 3.3 W, a 60% increase. The percent increase for the corresponding DI samples was from 80.8 W to 159.3 W, a near 100% increase. This provides further support for the increased sensitivity to processing temperature for DI based samples and if exploited correctly, can be used to reduce the overall energy input during electrode drying, one of the most energy intensive manufacturing steps a result that aligns nicely with previous modeling results. [59]

Although values for the heat transfer rate illustrate the efficiency of the drying process for each solvent, going one step further and dividing the total heat transfer rate by the enthalpy of vaporization, $E_{vap.}$, for each material, provides the rate of evaporation ($\dot{m}$) in terms of milligrams per second via Equation 15. This value, while considering an ideal vaporization condition, demonstrates a ~10X increase in drying rate for DI samples over their NMP based counterparts and again illustrates a much greater increase between set temperature for DI based samples as compared to NMP samples as shown in Figure 27. This result provides a concrete number associated with solvent removal that can readily be applied to

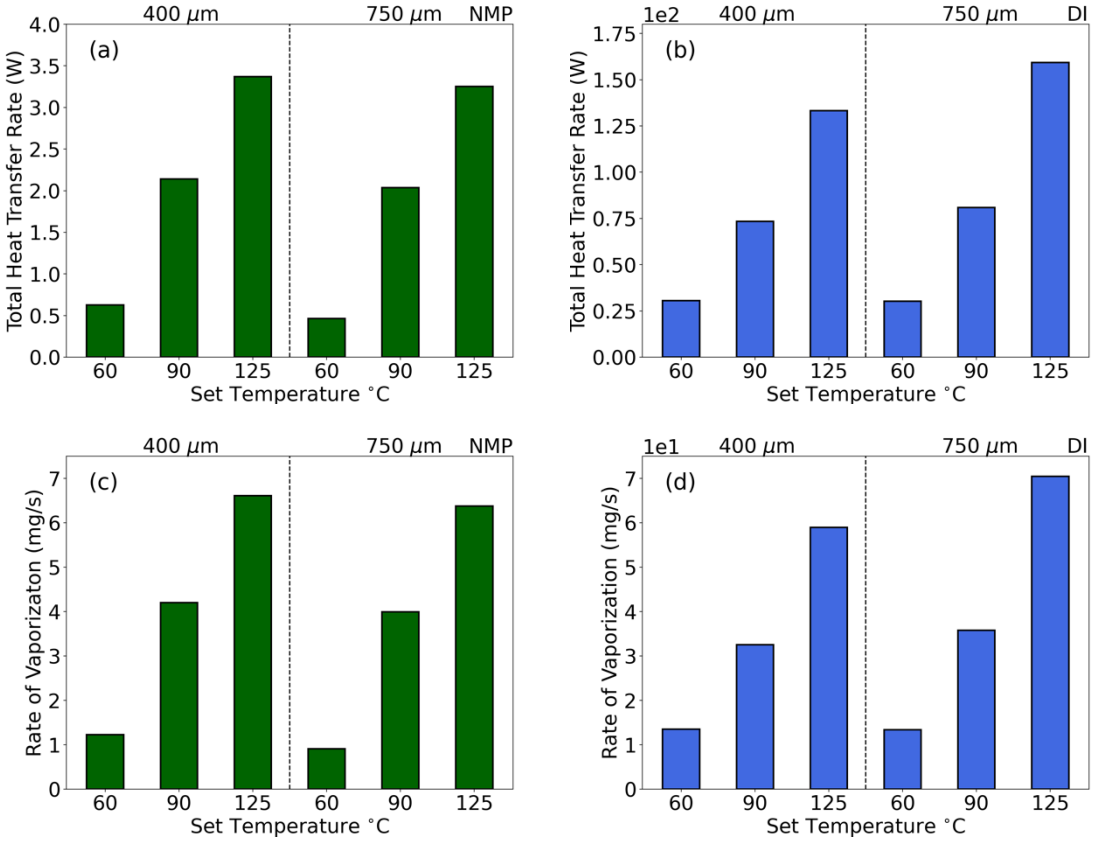


Figure 27. Total heat transfer rate to the a) NMP based electrode and b) DI based electrode (-$q$) and rate of vaporization ($\dot{m}$) for the c) NMP based electrode and d) DI based electrode.

inline manufacturing. Since the solvent mass before drying is a readily available quantity, one would be able to estimate the total time required to dry an electrode and be able to optimize the manufacturing process accordingly.

Equation 15: $$\dot{m} = \frac{-q}{E_{vap.}}$$

Combining the increased drying rate attained in the film shrinkage stage of drying with the ability to increase the solids loading from ~45% for NMP to upwards of 60% for DI water, the total time and energy dedicated to drying the electrode can be reduced by replacing NMP with DI water as the solvent of choice. [51] The cost savings can be further increased when factoring in capital equipment costs. If the total time required to dry an electrode is lower, by analogue, a fixed speed roll-to-roll drying line would be shorter in length, thus reducing both machine cost and reducing the overall footprint required to produce electrodes. Although solid contents in this study were intentionally kept similar to provide similar benchmarks in terms of amount of solvent removed, it is worthy to note that the solid content can be much higher in aqueous dispersion due to lower viscosity, only compounding the results presented here. [51]

***Binder Distribution via ToF-SIMS***

ToF-SIMS elemental maps are provided in Figure 28 and Figure 29 for both DI and NMP processed samples respectively. The binder distribution can be identified through the $Cs_2F^+$

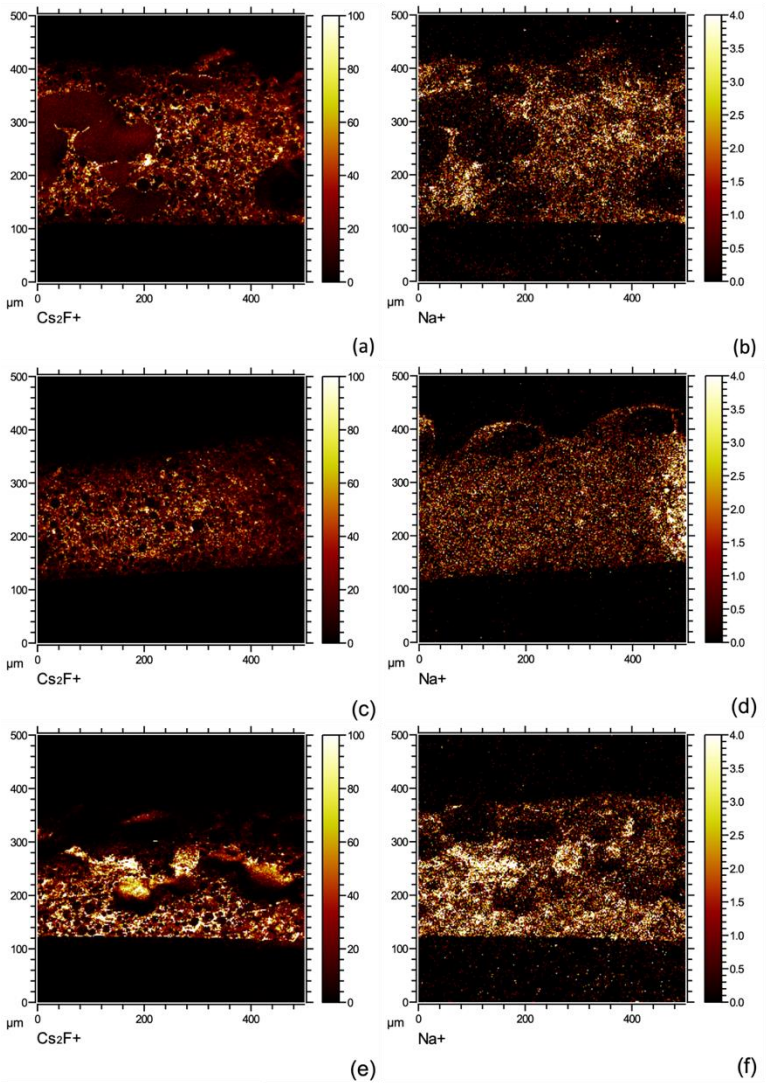


Figure 28. Cross-sectional ToF-SIMS elemental maps of DI processed 750 µm wet gap electrodes. Frames a) and b) are the 60 ℃ fluorine and sodium signals respectively. Frames c) and d) are the 90 ℃ fluorine and sodium signals respectively. Frames e) and f) are the 125 ℃ fluorine and sodium signal respectively.

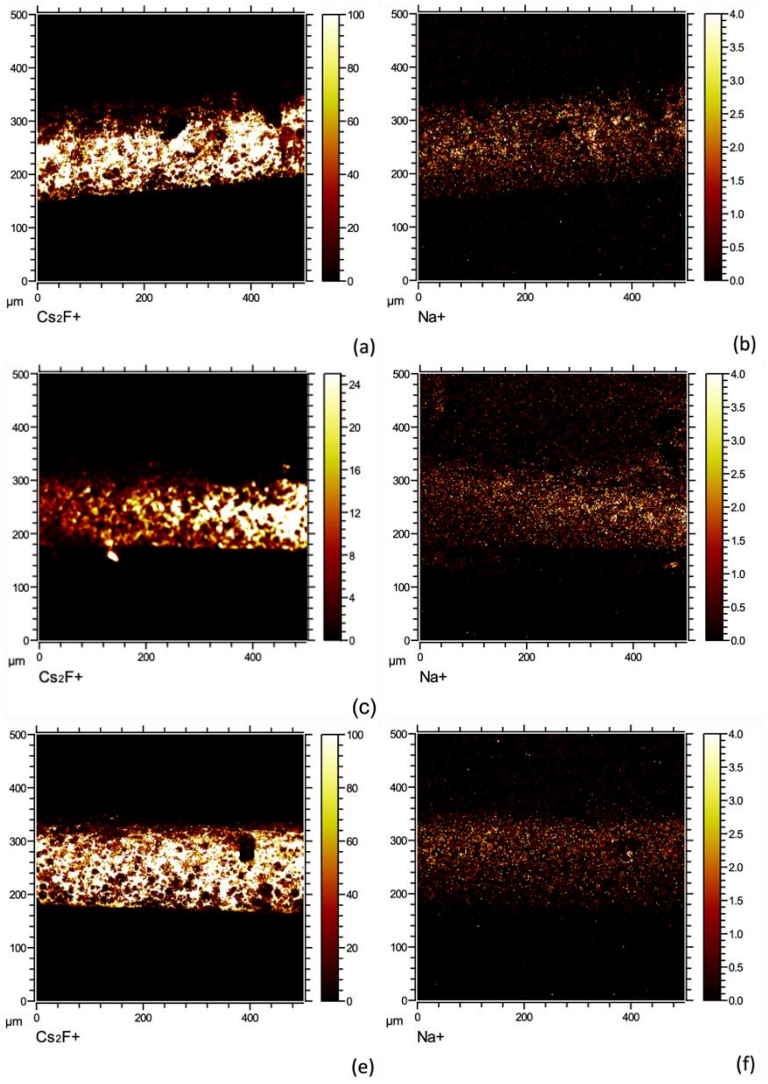


Figure 29. Cross-sectional ToF-SIMS elemental maps of NMP processed 750 µm wet gap electrodes. Frames a) and b) are the 60 ℃ fluorine and sodium signals respectively. Frames c) and d) are the 90 ℃ fluorine and sodium signals respectively. Frames e) and f) are the 125 ℃ fluorine and sodium signal respectively.

ion signal as the binders are the only fluorine source within the electrodes. Sodium ion signals can also be used to detect binder in DI based samples as the CMC binder is the major source of sodium. It is important to note however, the active material particles have been determined to contain sodium surface contamination, leading to a weak sodium signal in all samples. For DI samples, the binder distribution is most homogenous at 90 ℃, providing a potential explanation for increased electrochemical performance observed at high discharge rates, which is discussed in the next section. DI samples dried at 60 ℃ and 125 ℃ both exhibited inhomogeneous binder distributions with the 60 ℃ sample appearing to have pockets of increased binder concentration at random locations and the 125 ℃ sample having increased binder content near the current collector. It is difficult to ascribe the exact mechanism without being able to monitor the development of the electrode during the drying process, but the poor binder distribution in the 60 ℃ DI based sample is likely to impede electrochemical performance. As the only difference between electrode production was the temperature at which the electrodes were dried, the binder distribution is through to be a direct consequence of the drying temperature.

These effects are not though to be related to corrosion effects known to occur at the current collector interface because phosphoric acid was used in slurry preparation and has previously been shown to mitigate corrosive effects in aqueous processed nickel-rich active materials such as NMC 811. [14, 47] Furthermore, there is no evidence of void space in the chemical maps, which would be indicative of the gas generated via the well-known corrosion reaction that takes place at the aluminum current collector. [108, 193] Similarly,

as all electrodes were coated using the same slurry material, the differences in binder distribution cannot be attributed to differing mixing conditions and therefore must be driven primarily by temperature differences. Without *in-situ* monitoring of the binder distribution, the exact mechanism for inadequate binder distribution remains elusive.

NMP samples at each drying temperature display homogenous binder distribution throughout the electrode suggesting the temperature range did not exceed the limit at which binder segregation in NMP processed electrodes begins and suggests a suitable binder distribution is attainable over a wide range of drying temperature for NMP based electrodes. These results also provide additional support to the earlier claim that NMP processed electrodes are less temperature sensitive as compared to their DI processed counterparts. This is beneficial from a processing standpoint as there exists a wider acceptable temperature range for processing, however this also means the overall energy input is not greatly impacted by drying temperature and thus savings will be minimal for NMP processed electrodes.

***Electrochemical Testing***

Rate capability results show NMP based samples outperform DI based samples at most discharge rates as seen in Figure 30 are comparable to previous reports of both aqueous processed and ultra-thick electrodes. [14, 194] For electrodes with 2.5 mAh/cm$^2$ areal loadings (400 μm), the NMP processed cells display a consistently higher discharge

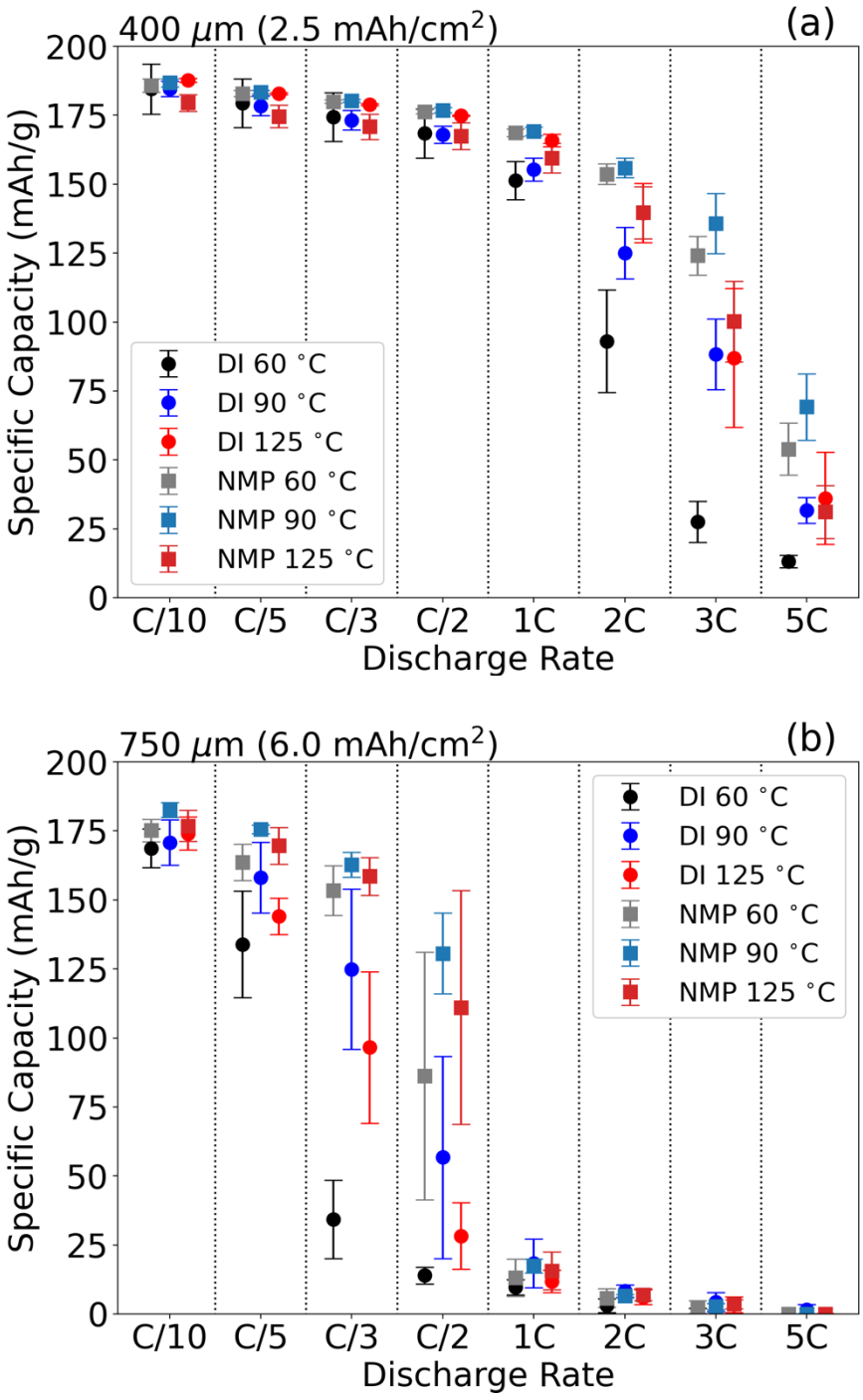


Figure 30. Rate capability results for a) 400 μm and b) 750 μm wet gaps at each drying temperature.

capacity, especially as discharge rates exceed 1C. This is partially ascribed to the addition of phosphoric acid, which has been reported to form $Li_3PO_4$ passivation layer on NMC 811 particles and results in higher charge transfer resistance. [47] It is demonstrated that a moderate drying temperature (90 ℃) produced electrodes with best rate performance regardless solvent selection and areal loading. These differences were most notable for samples produced with DI as the solvent. The specific discharge capacity at 1C increased from 110 mAh/g to over 160 mAh/g for the 2.5 mAh/cm$^2$ DI coating when the drying temperature was increased from 60 ℃ to 90 ℃ as seen in Figure 30 (a). Other temperature driven differences in discharge capacity can also be identified such as the overall increase in discharge capacity for NMP processed electrodes at 90 ℃. This difference is thought to be a result of the superior binder distribution of the 90 NMP electrode as the electrochemical benefit is rather small, in line with the difference in binder distribution for the NMP samples. Although the sample appears to have increased binder homogeneity, the degree to which the distribution is improved is small. This result does suggest a universal ideal drying temperature of 90 ℃, regardless of solvent choice. Naturally this may not be the ideal temperature but is the best performing drying temperature investigated in this study.

Differences in discharge capacity are also heavily impacted by the areal loading of the electrode as shown in Figure 30. Unsurprisingly, as the areal loading is more than doubled from 2.5 mAh/cm$^2$ to 6 mAh/cm$^2$, the discharge capacity decreases precipitously. This large decrease is due to mass transport limitations due to constrictive lithium-ion diffusion

pathways within the electrode. Compounding this constrictive pore network, is the poor binder distribution previously identified by ToF-SIMS chemical mapping. Although the polymetric binder does not participate in the electrochemical reaction directly or to a large extent, it facilitates the reaction by creating a conductive network of carbon black and active material particles. The effects of the poor binder distribution are the same as in the lower areal loading (2.5 mAh/cm$^2$) cells, but the decrease in specific discharge capacity is much more pronounced in the higher areal loading cells.

What is obvious from the presented electrochemical data, is the detrimental effect of ununiform binder distribution on cycling performance, a well-established trend. [97-100] Less obvious is the connection to efficiency and cost savings. As aqueous processing continues to gain momentum for economic and environmental concerns, the identification of a preferred drying condition for such cathodes can lead to overall improvement in cycling performance. Demonstrated at all areal loadings for DI samples is a strong dependance on initial drying temperature. As most of the damage to electrode formation occurs during the initial film shrinkage stage of drying, tuning the initial drying temperature has the potential to result in radically different electrochemical performance for aqueous processed cathodes.

## Conclusion

Benefits of using DI water rather than the conventional solvent, NMP, were investigated via an in-depth chemical engineering model and electrochemical testing. The energy input requited for DI samples was less than that of NMP samples and was more sensitive to changes in drying temperature that NMP samples as well. This suggests that DI samples could be initially dried at a temperature that maximizes the binder distribution homogeneity, here found to be 90 ℃, and then the drying conditions could be increased to maximize the efficiency of the pore emptying stage. This combination would reduce the drying time and energy input considerably compared to current NMP processing. Binder distribution information gather via ToF-SIMS confirms the optimal drying temperature for DI samples at 90 ℃ and confirms NMP samples are generally less sensitive to changes in drying temperature, provided the temperature is below the limit of binder migration occurring, which was not observed in this study for NMP samples. Electrochemically the differences in cycling between NMP based samples was minimal while the DI samples exhibited a wide range of capacity with 90 ℃ again being the optimum, which is likely a result of the more homogenous binder distribution observed at this temperature and suggests tuning of drying temperature for aqueous processed cathodes is of great importance to electrochemical performance. Overall evidence is provided suggesting DI processed cathodes can be effectively produced and can provided an economic benefit to the cell production as a whole compared to the customary solvent, NMP.

# CHAPTER VI
# TRANSISTION TO SOLID STATE ELECTROLYTES

## Background

Lithium-ion batteries (LIB) have transformed the way energy storage has been approached since their commercialization in the early 1990's. Although conventional LIBs have been the catalyst for increased energy density and cost reduction, the goals set by the DOEs Vehicle Technologies Office (VTO) and the United States Advanced Battery Consortium (USABC) may require a different type of secondary battery. All solid-state batteries (ASSB) offer increased energy density and longevity while also reducing operational safety concerns that are present in conventional LIBs. By using a solid-state electrolyte as opposed to liquid electrolytes, the systems become inherently safer, as liquid electrolytes are highly flammable and conventional LIBs tend to approach thermal runaway more easily as they are scaled up in size. [195, 196] Elimination of liquid electrolyte also removes $PF^{-6}$ anions from the cell chemistry, leading to a more environmentally benign cell. [58] The use of solid electrolyte also provides greater mechanical stability while eliminating the need for a separator material between electrodes. [197-200]

Although ASSBs offer promising advancements, they still face numerous technical challenges that prevent widespread adoption. Solid electrolytes currently used typically show optimal ion conductivity only at elevated temperatures, and even then, the ion conductivities are not on par with liquid electrolytes. [201, 202] Material sensitivity also limits production scalability as some components are sensitive to air and/or water. [198, 199, 203-205] This sensitivity requires special conditions for preparation, which are

currently cost prohibitive at large scale. [21, 199, 203, 206] Additionally, interfacial compatibility between solid electrolyte candidates and composite cathode and lithium anode materials have not been fully explored and may lead to incompatibility issues. [81, 196, 198, 199, 203, 207]

Solid state electrolytes can be grouped into two main categories, organic polymers and inorganic glasses and ceramics. [21, 199, 203, 206] Polymer electrolytes typically involve a lithium salt dispersed in a UV-curable organic polymer such as polyethylene oxide (PEO). [197-199, 208] Inorganic glassy or ceramic solid electrolytes are typically produced through high pressure formation or sintering techniques. [197-200, 202] Typically inorganic glasses and ceramics display higher ionic conductivities but may not be able to facilitate electrode expansion whereas organic polymer electrolytes can accommodate changes in cell volume well but have poor room temperature ionic conductivities.

Ceramic and polymer type electrolytes have each garnered a large amount of interest due to their mechanical and ionic transport properties. Ceramic electrolytes are able to provide much needed rigidity in thin film batteries, where polymer type electrolytes can accommodate flexibility needs to a degree. [199-201, 209] However, both types of electrolytes exhibit low ionic conductivities at room temperature, and thus need to operate at elevated temperature or sintered at high temperatures in order to achieve acceptable ionic conductivities, on the order of $10^{-4}$ S/cm, the minimum ionic conductivity for vehicle applications. [21, 83, 199, 203, 206] Increased operating temperature is in some cases

permissible, but an ideal candidate solid state electrolyte would have a room temperature ionic conductivity approaching that of liquid electrolyte. Acceptable room temperature conductivities eliminate the need for additional hardware required to maintain an elevated temperature, making these cells both more efficient and more flexible from a deployment standpoint.

Within the ceramic types of solid electrolytes, there are two general subcategories, oxide-based electrolytes and sulfide-based glassy electrolytes. [21, 199] These two types of electrolytes each have their advantages and disadvantages in that oxide-based solid electrolytes are more stable against processing environments, but require an expensive sintering step, whereas sulfide-based electrolytes can skip the costly sintering process but need to be handled in inert conditions to prevent toxic hydrogen sulfide gas generation. [198, 199, 203] These two issues are large drivers in current solid state electrolyte research, namely, how to move from laboratory scale to pilot or full-scale manufacturing without incurring prohibitively high processing costs. Oxide based electrolytes also exhibit lower ionic conductivity when compared to sulfide-based systems, necessitating thinner films to compensate for the lower ionic conductivity. [210]

Although they have been around since 1975, polymer electrolytes have experienced an increased amount of interest after successful implementation in the LIB applications. [211, 212] Although polymer electrolytes avoid many of the processing challenges associated with oxide or sulfide based electrolytes, they are plagued by low ionic conductivities at

room temperature and thus require external cell heating for optimal performance. [213] Issues regarding stability of the electrolyte upon exposure to electrode materials or metallic lithium have further complicated the future of polymer solid electrolytes. [77]

Electrode material also requires special consideration in the transition from conventional LIBs to ASSBs. Although typical graphite and silicon anode material is compatible with some solid electrolytes, some interfacial issues still exist. The most concerning interfacial incompatibility with respect to lithium anodes is the formation of dendrites. As the cell is cycled, lithium has the potential to plate or form dendrites at the electrode surface. [197-199, 203, 214-217] In conventional LIBs, dendritic growth of lithium can puncture the separator membrane and cause an internal short circuit. This not only effectively eliminates all cell capacity, but also poses an electrical and fire hazard as thermal runaway increases in probability with any internal short circuit. [82, 83] ASSBs can help mitigate risks imposed by dendritic growth by substituting a solid electrolyte for the porous separator membrane. Dendrites are somewhat less likely to pass through a dense solid electrolyte and consequently provide a much safer operation regime. [83] Although growth can be mitigated, it has been shown dendritic growth is more likely and problematic at grain boundaries of some oxide type solid electrolyte, potentially requiring single crystal growth of such electrolytes. [197] Large scale single crystal growth of oxide based solid state electrolytes with optimal thickness, on the scale of microns, is exceptionally difficult and may be prohibitive of such solutions. [206, 218]

With mitigation of dendritic growth, the use of a pure lithium metal anode becomes attainable. With a high specific capacity, 3860 $mAhg^{-1}$, and low density, 0.59 $gcm^{-3}$, the overall energy density of the cell can be increased dramatically. [81] Although lithium has some clear benefits, engineering the electrode encounters multiple hurdles. For a 50% excess lithium in cell with a 100μm cathode, approximately 60 μm of lithium is required. [206] Typical deposition techniques for such small thick- nesses require physical vapor deposition or melt processing, although in situ lithium platting by depositing excess lithium from the cathode active material is also. a promising route. [206] By using the available lithium inventory that is already in the cell, and anode can be constructed via lithium platting, resulting in a lithium metal anode that has little associated cost. [21] Although this would be cost effective, a uniform and dendrite free lithium anode would be difficult to attain.

Interfacial contact is another major concern with solid electrolytes. Electrode material expands and contracts depending on the state of charge, typically between 2-4% for intercalation cathodes and up to 10% for conventional graphite anodes. [196, 215] In liquid electrolyte cells this expansion is typically compensated by reformation of the solid electrolyte interphase layer (SEI) and will consume small amounts of electrolyte. Generally, once a stable SEI layer is formed, expansion and contraction effects can be mitigated. However, with a solid-state electrolyte, especially a garnet type, expansion and contraction of the cathode and anode leads to delamination at the interface. [196, 215] Polymer electrolytes can help ease this ohmic resistance increase due to the increased

flexibility of the material but may present other interfacial issues as a result of instability at the interface. Cathode and solid-state electrolyte interfaces can be engineered in multiple ways. Electrolyte can be cast via a stand-alone or 'green tape' method where the sintered electrolyte is completed before adhering to an existing cathode. [21, 219] Alternatively, electrolyte slurry material can be infiltrated into a cathode structure before sintering creating a composite cathode with a large interfacial surface area. [21] Although both of these methods can create an effective interface, expansion of the electrode through cycling may degrade the interface over the life of the battery. Issues also arise with sintering steps as some cathode materials are not stable at temperatures required for electrolyte sintering. [21]

Industrial scale production of solid-state electrolytes is not only difficult, but also very expensive compared to conventional LIBs and is currently not a mature process in industry. Where in a conventional LIB, 70-80% of the total cell cost is contained in materials cost, a comparable solid state battery would have 75% of the total cost associated with processing alone. [21] Current techniques for processing most oxide solid electrolytes, such as $Li_7La_3Zr_2O_{12}$ (LLZO), include a sintering step that can account for 20% of total processing cost. Eliminating this step, although cost saving, may be impossible to do without sacrificing performance or mechanical stability. Currently, studies focused on co-sintering cathode active material along with solid electrolyte precursor material are aiming to curb the total sintering steps or sinter at lower temperatures. [21] Lower temperatures would be required to perform a co-sintering step as most cathode active materials form

unwanted products at elevated temperature. [206] Sulfide based electrolytes do not require a high temperature sintering step, but they do require inert atmospheres as they will generate toxic hydrogen sulfide gas if exposed to air or water. This requires processing in a glovebox for laboratory scale, but would need a larger, more expensive processing environment for large scale production. [21, 203]

Polymer electrolytes are easier to produce from a manufacturing standpoint, but they suffer from lower room temperature ionic conductivities. Typically, combinations of polyethylene oxide and other long or short chain polymers combined with a conductive salt form the basis of polymer solid electrolytes. [21, 214] Production involves dispersion of different polymers and additives before a curing step solidifies the polymer. Solidification of the polymer can occur independent of other cell components, forming a fully solidified polymer electrolyte that can then be added to a cell assembly, referred to as green tape casting. A second technique is to coat an electrolyte slurry directly on top of an existing electrode, this allows the electrolyte to infiltrate the electrode structure before solidification, increasing the area of the contact interface. The later approach is referred to as infiltration and can create a better interface between the electrolyte and electrode active material, helping the overall conductivity. [21, 219]

Although NASICON and LiPON type electrolytes have been around since the 1960's and 1990's respectively, newer formulations and structures are quickly dominating the field.

[198] Even though these electrolytes are lower in ionic conductivity that the newer materials, further research is still warranted and should be pursued.

Regardless of solid electrolyte composition and cell design, it is clear that solid state electrolyte lithium batteries are the future of secondary batteries. The challenges posed by material limitations and production costs are not impossible, only difficult to solve. With proper investment, analysis, and development, all solid-state batteries have the potential to eclipse conventional liquid-based cells within the next decade.

## Motivation

In order to develop a more energy dense and lower cost secondary battery, interfacial and processing issues related to solid state electrolytes need to be resolved. Processing that currently requires sintering at high temperature should be reduced or, if possible, eliminated. Although multiple processing techniques are being investigated, there are still major hurdles to overcome when transitioning to industrial scale production. Improving the viability of either type of solid-state electrolyte can help increase the market adoption of all solid-state batteries. ASSBs have the potential to become the new standard for highly distributed storage devices if these major hurdles can be cleared in a cost effective and production friendly manner.

Conventional LIBs have enjoyed extensive research and development interest over the past few decades that have driven the production cost down from $1,000/kWh in 2008 to $197/kWh in 2017. [220] Along with a dramatic reduction of cost, LIBs also saw an increase in energy density from 55 Wh/L to 250 Wh/L over this same time period. [220] This simultaneous decrease in cost and rise in energy density are critical to successful adaptation to vehicle applications.

Factors responsible for cost reduction and increased energy density of LIBs are largely related to manufacturing and materials improvements. [199] Development of new materials both reduced cost and provided a higher practical capacity while maintaining the same cell format, such as the transition from pure carbon anodes to silicon graphite designs. [221] While combining new technology with more efficient manufacturing techniques has clear benefits, the marriage of these two approaches is often time consuming and labor intensive.

Some of the lessons learned from the evolving LIB studies are directly applicable to the development of all solid-state electrolyte, such as electrode architecture and porosity. Although some aspects can be directly translated to all solid-state battery production, aspects related to the electrolyte such as electrode interfaces and ion diffusion may need to be completely reinvestigated. The most challenging aspect of this transition to solid state electrolyte will be how to manufacture the electrolyte with acceptable ionic conductivities

and mechanical performance on an industrial scale. [21] It is this juncture that will foreseeably be the most costly and time consuming aspect of ASSB development.

Current approaches differ depending on the type of solid electrolyte but share some basic characteristics, turning precursor materials into a solid ionic conductor with low electronic conductivity. Typically, oxide and sulfide type solid electrolytes display higher room temperature conductivities compared to polymer type and thus have garnered substantial interest. [21, 222] These ceramic electrolytes are commonly made via conventional solid state reaction and subsequent pressing and or sintering. [214, 222] Not only is this process labor intensive, but it is also expensive. With sintering temperatures as high as 1250 ℃ and times on the order of 10 hours, this process adds considerable cost to electrolyte production. [21] As a result, a number of studies aim to reduce both the time and temperature required to engineer an electrolyte candidate, some going as far as to eliminate this process entirely. [218] Polymer solid electrolytes can omit this costly processing step, but display lower ionic conductivities at room temperature, an issue that is being addressed by creating composite polymer/ceramic electrolytes. Following are major areas of interest within the all solid-state production discussion. Each topic has seen substantial progress, but still requires improvement.

***High Temperature Materials Processing***

Oxide type solid electrolytes, namely LLZO, require high temperature sintering to achieve proper densification and sufficiently high ionic conductivity. [223] Sintering temperature

has also been linked with sufficient suppression of dendritic growth. [224] With processing temperatures in excess of 1000 ℃, sintering makes up a substantial portion of the overall production cost of such ceramics. [21] Although costly, high sintering temperatures can aid in the densification of the electrolyte, but also catalyze lithium evaporation. [225] Evaporation of lithium directly effects ionic conductivity and can be mitigated by covering the material in mother powder. [225] The constraints of temperature effects on structural formation are also important to determine. LLZO for example has been shown to take two separate crystal structures, the cubic Ia3d or tetragonal I41/acd, depending on sintering temperature and technique. [226, 227] Although this change in crystal structure is critical to the resulting ionic conductivity of the electrolyte, the mechanism by which the structure is transformed is still unknown. [228]

One of the most challenging issues surrounding high temperature production of oxide based solid electrolytes is the lack of a clearly defined protocol. [223, 225, 229, 230] This in some ways is advantageous as there is some apparent flexibility, but makes the results involving different sintering temperatures, sintering times, and techniques difficult to compare. As the number of studies increases, clear trends are emerging. The use of aluminum in order to lower the sintering temperature and promote the highly conductive cubic phase being perhaps the clearest. [79, 230] Further work on reducing sintering temperature while maintaining the highly conductive structure. Although some promising results have been reported, further research is necessary to optimize production.

***Processing of Sensitive Materials***

Sulfide based solid state electrolytes are promising candidates as they can be processed without high temperature sintering and display more flexibility than oxide based electrolytes. [200] Sulfide based systems can be fabricated through a room temperature pressing procedure where constituent powders are subjected to high pressure (20-30 GPa) in order to achieve densification. Sulfide electrolytes also exhibit higher room temperature conductivities, on the order of $10^{-4}$ $Scm^{-1}$, making them an ideal candidate. [200] Although sulfide-based electrolytes have considerable advantages, they also require special precautions, namely high reactivity in ambient conditions. Sulfide electrolytes must be fabricated and handled in inert atmospheres as generation of dangerous $H_2S$ gas can form as a result of exposure to humid air. [203] Sulfide electrolytes also present problems with interfacial stability, with a narrow stability window sulfide electrolyte can decompose at potentials typically used for LIBs. [80, 203, 204] Scaling up cold pressing techniques and associated inert processing conditions is non-trivial and remains to be resolved.

Sulfide based electrolytes are not alone in their instability in air. Some oxide based electrolytes, such as LLZO, have also demonstrated instability in air, creating a $Li_2CO_3$ insulating layer upon exposure to humid air. [83, 231] Although LLZO is typically processed and sintered in air to develop the correct crystal structure, it has been demonstrated that humid air degrades the mechanical and ionic properties of this solid electrolyte, with a pronounced effect at grain boundaries. [232] This sensitivity leads to

degradation of mechanical properties as well as a reduction of ionic conductivity, reportedly through a proton exchange mechanism between water and LLZO. [232] Polymers typically enjoy less restrictions with respect to processing conditions, in some cases being fabricated and even cycled in ambient conditions. [233]

***Ionic Conductivities***

One of main areas of improvement identified for solid electrolytes is their low ionic conductivity. Compared to conventional liquid electrolytes, typically a lithium salt such as LiPF6 in organic solution, solid electrolytes exhibit much lower ionic conductivities. [83] The highest solid state electrolyte ionic conductivity reported belongs to the sulfide based glassy electrolytes, $2 - 27 \times 10^{-3}$ $Scm^{-1}$, comparable to the ionic conductivity of the typical $LiPF_6$ in organic solution, $5 - 20 \times 10^{-3}$ $Scm^{-3}$. [21, 200, 234] However, even though sulfide electrolyte approach the range of ionic conductivities required for vehicle applications, they still have interfacial stability issues as well as processing sensitivity concerns. [80, 203]

Although promising, ionic conductivities of oxides are still limited to $0.25 - 1 \times 10^{-3}$ $Scm^{-1}$. [21] Oxide electrolytes can achieve sufficient ionic conductivities if processed correctly, but their ionic conductivities show a dependence on processing technique. Bulk ionic conductivity of ALLZTO is accepted to be $5 \times 10^{-4}$ $Scm^{-1}$, whereas ALLZTO obtained via aerosol deposition only displays room temperature ionic conductivities of 2 ×

$10^{-7}$ $Scm^{-1}$, a three orders of magnitude difference. [218] Between these values lies the ionic conductivity of screen printed LLZONb, $2 \times 10^{-6}$ $Scm^{-1}$, compared to the bulk ionic conductivity of LLZONb, $8 \times 10^{-4}$ $Scm^{-1}$, a slightly less egregious difference of two orders of magnitude. [235, 236] Sintering can help improve aerosol deposited ALLZTO, but then the expensive sintering step that had been avoided is reintroduced. Differences in ionic conductivity are attributed to film strain within the ceramic electrolyte, which can be remedied by high temperature treatment. [218]

Ionic conductivities of oxide-based systems are also highly dependent on crystal structure. For example, cubic LLZO has an ionic conductivity that is two orders of magnitude higher than tetragonal LLZO, which is achieved when doped with aluminum during the production process. [226, 227] Although the dependence on crystal structure is clear, the stable structure of some compounds are not always clear. [224] In addition to crystal structure, crystal formation is also important to consider when discussing ionic conductivity. Grain boundaries introduce resistance within the cell, therefore, attention some attention has been shifted to how grain boundaries can be optimized to exhibit minimal resistance. The addition of silicon in the preparation process has been shown to help reduce the grain boundary resistance, and subsequently improve ionic conductivity of LLZO, for example. [229]

Polymer electrolytes display the worst ionic conductivity of all solid electrolytes, $1 - 15 \times 10^{-5}$ $Scm^{-1}$. [21] Despite their low ionic conductivities, polymer electrolytes have been

implemented in vehicle batteries with some success. [21] Polymer electrolytes do exhibit higher ionic conductivities with elevated temperature, necessitating external components. Polymers also allow for increased flexibility, potentially opening the door to combinations of oxide electrolytes and polymer electrolytes, creating a composite electrolyte that maintains the higher ionic conductivity of an oxide system and mechanical properties of a polymer system. Regardless of the electrolyte type, ionic conductivities, particularly room temperature ionic conductivities, require improvement in order to compete with liquid electrolyte. Doping oxide or sulfide systems have proven to increase ionic conductivity in these systems, but further improvements are needed. [218, 235, 236]

***Aerosol Deposition***

In a typical aerosol deposition scheme, constituent ceramic powers are placed in a fluidized bed and transported by pressure difference or carrier gas to the deposition chamber. These powders pass through a nozzle above 150 m/s and subsequently collide with the substrate resulting in fragmentation of the original particle into fragments. These nano-sized fragments are subsequently compressed by incoming particles resulting in a thin film with high density. [237-241] The film is presumably formed by new interfaces creating chemical bonds upon fracture. [239] Major advantages of this process include no requirement for heating or sintering, lack of binder, and highly tunable final thickness. [238] Resulting films typically display little surface cracking and high adhesion, but deposition rates are

very low, 10 mm3/min, resulting in a far slower process compared to other techniques. [206, 239]

Aerosol deposition has seen success in deposition of cathode and anode active materials and some solid-state applications, such as LLZO. [218, 237, 239, 242-250] When applied to LLZO, this type of deposition still requires the high temperature calcination process but can forego the costly high temperature sintering step after the film has been constructed. Although thin films can be reliably constructed, the resulting ionic conductivities of these aerosol thin films is considerably lower than rated bulk ionic conductivity. [218, 239, 243] Notably, aerosol deposited cubic ALLZTO displayed an ionic conductivity before post treatment of only $2 \times 10^{-7}$ $Scm^{-1}$, three orders of magnitude lower than the accepted bulk ionic conductivity of $5 \times 10^{-4}$ $Scm^{-1}$. [218] In some cases, this low ionic conductivity can be increased with the addition of a sintering step. [218, 239] Although this step aids in increasing the ionic conductivity, the result is still an order of magnitude lower than bulk ionic conductivity and the time and energy intensive sintering step is reintroduced, adding considerable cost.

Although film thickness can be highly controlled and kept within the 10 - 100 μm range, low ionic conductivities and long deposition times make this technique difficult to scale. [206, 218, 239] At bench top scale, this approach can produce acceptable solid state electrolytes, but implementation at industrial scale will require either large deposition chambers or sacrificing quality of the thin film by increasing deposition rate. [206]

### *Lithium Metal Anode*

More things and stuff and words and information.  All solid-state LIBs make possible the implementation of lithium metal as an anode candidate. Lithium metal has a much higher theoretical specific capacity of 3860 mAh/g, an order of magnitude higher than the achievable specific capacity of graphite, 370 mAh/g. [81, 83, 199, 207, 221] The drastic increase in specific capacity makes all solid state batteries competitive with the specific energy and energy density of conventional LIBs all while eliminating safety concerns associated with liquid electrolyte. [21]

Implementation of a solid electrolyte, particularly a ceramic type electrolyte, makes possible the use of a metallic lithium anode. [21, 81, 199, 206, 207] The use of a pure lithium anode has the potential to in- crease the specific energy of a cell by up to 53% when using all solid state electrolytes and can reduce the overall anode thickness by 75%. [199] Although the specific capacity of pure lithium is an order of magnitude greater than the typically used graphite anode, pure lithium has not been used in conventional LIBs due to dendrite formation and subsequent internal short circuits. All solid-state batteries, particularly oxide-based ceramics, are able to prevent dendrites from reaching the cathode. [21, 81, 199, 206]

Although lithium metal is a promising candidate for anode active material used in all solid-state batteries, serious obstacles still need to be overcome. Sulfide based electrolytes have

displayed electrochemical instability when cycled with lithium metal anodes, suggesting an SEI type layer may be required to inhibit further decomposition. [78, 80, 199] Unlike sulfide based solid electrolytes, oxide based electrolytes have displayed resistance to decomposition when paired with metallic lithium anodes, showing stability up to 8 V. [21] Lithium anodes in polymer electrolyte cells have seen some success, but dendrites can still puncture the polymer electrolyte, requiring slow charge rates. [207] When using pure lithium in a solid state cell, the low melting temperature of lithium (180.5 °C) should also be considered, as most solid state electrolytes display best ionic conductivity at elevated temperature. [207] Although these temperatures are considerably lower than the melting point of lithium, typically under 100 °C, thermal runaway may constitute an issue. Pure lithium is also an expensive material and lithium foils suitable for anode applications must be very thin, on the order of 10 - 100 μm, a constraint that further increases the material cost associated with lithium anodes. [199, 206]

As an alternative to purchasing lithium foil directly, ideas of in-house processing or in-situ plating have been proposed as cost reducing measures. [206] In-situ construction of the anode is a promising approach that uses excess lithium from cathode active material to plate a lithium metal anode during formation cycling. Ideally resulting in a thin and uniform pure lithium anode without the need for expensive and time consuming lithium metal processing. [206] These approaches have the potential to introduce a lithium metal anode without incurring expensive processing costs, but further investigation is required to ensure

dendrite formation along grain boundaries, in the case of LLZO for example, are not detrimental to long term use and safety. [21]

In order to advance this technology, a new processing technique for obtaining oxide or sulfide solid state electrolytes is needed. Devising a technique for adhering these electrolytes to electrodes is also crucial as delamination initiated by volumetric changes within electrodes during charging and discharging is a major concern. [21, 199, 221] Ultimately this new processing technique would allow for a combination of solid-state electrolytes in a solid state composite that would likely be infiltrated into a structured high capacity cathode. A composite electrolyte would potentially provide the mechanical flexibility of a polymer electrolyte and the high ionic conductivities of oxide-based electrolytes. Infiltration could be accomplished via combining the uncured polymer gel and power solid electrolyte and coated directly onto an existing structured cathode. The use of a lithium anode would also be ideal; however, a cost effective and safe deposition technique would be required.

## Full Scale Manufacturing Methodology

Conventional LIB production utilized roll to roll manufacturing techniques, such as slot-die coating, to cast wet inks or slurries onto a current collector backing that will then be dried, calendared, and punched into final electrodes. This type of processing is fast, cost effective, and provides reliably high-quality end products. The technology is also highly

scalable, moving from doctor blade hand coatings to industrial sized slot-die coatings, the same general principle is involved. While transitioning to solid state battery production, the incorporation of roll-to-roll manufacturing can help maintain the high speed and high-quality production without having to reinvent or reacquire expensive infrastructure.

In order to maintain the roll-to-roll processing technique, solid state electrolyte either need to conform to the roll-to-roll process, as is currently under investigation with co-sintering, co-curing, and green tape casting techniques, or be incorporated in end of line assembly techniques, popular with oxide and sulfide based electrolytes. Regardless of electrolyte type, maintaining the roll-to-roll manufacturing techniques can be critical to the widespread adoption of solid-state batteries. Below are proposed full scale manufacturing techniques for each major type of solid-state electrolyte. Each methodology attempts to incorporate existing manufacturing techniques in order to minimize the need for new equipment.

***Polymer Based Electrolytes***

Polymer electrolytes are perhaps the easiest to implement in a full-scale conventional LIB manufacturing setting as they can be coated as a slurry and either thermally cured or cured via UV or e-beam techniques. This can be accomplished in either two distinct coating steps or via dual slot die coating, where the cathode and electrolyte slurry are cast and cured together. Coating the two layers separately would require two passes or two machines.

While coating the electrolyte layer, the polymer slurry ideally would be infiltrated into a structured cathode layer in order to promote a durable interface and improved contact area. Infiltration may not be optimal without adequate pressure or time to fill voids in the cathode structure before curing. If a dual slot-die approach were taken, it is unclear how the interface would cure and to what extent the two slurries would be intertwined. This a key point that needs to be investigated when considering co-sintering or co-curing of electrodes and polymer electrolytes.

When considering polymer electrolytes, a silicon graphite anode is likely to be used as polymer electrolytes have displayed limited stability against lithium metal anodes and dendrites have been shown to eventually puncture polymer electrolytes. With a conventional anode material in use, the same slot die coating technique can be employed, again in two distinct manners. First, the now cured cathode-electrolyte composite can serve as the substrate onto which an anode slurry is coated and dried, providing maximum infiltration and leaving the current collector for last. Secondly, the anode can be cast completely separate from the cathode-electrolyte composite and the resulting anode can be introduced later in the assembly process, sacrificing infiltration between the anode and electrolyte, but ensuring optimal adhesion at the anode current collector interface. In the case of polymer electrolytes, theoretically the order of operations can be reversed, first coating the anode and electrolyte and saving the cathode for the last step without sacrificing generality. However, in order to ensure no generality is lost, this claim should be tested.

The inert nature of polymer electrolytes in air allows the processing of this material in ambient, or preferably dry, conditions that already exist for electrode fabrication. This makes the transition from conventional LIB production to solid state battery production relatively straight for- ward, even enabling the continuation of current assembly methods after electrode and electrolyte preparation. However, there are downsides, none more critical than the poor room temperature ionic conductivity of polymer solid electrolytes. Industrial production of polymer electrolyte based solid state batteries is not new, the technology has already been industrialized. [21, 206] The technology does have substantial room for improvement, however.

***Oxide Based Electrolytes***

Oxide based solid electrolyte manufacturing likely cannot fully incorporate roll to roll manufacturing techniques like polymer-based electrolytes can. Due to the high temperature sintering requirements of most oxide-based electrolytes, the most likely manufacturing approach will be creating the electrolyte in a separate sintering step and then only after calcination and densification, affix the electrodes. This can happen in two general ways, full component marrying or component addition. In a full component marrying scheme, the electrode and electrolyte will be fabricated completely separate from each other and only when fully formed, will the components be assembled to produce a battery. This is indicative of current LIB production methods. In a component addition method, the electrolyte would first be produced, followed by addition of an electrode slurry. In this

case, the battery will be built up one operation at a time. This would allow for increased infiltration of the electrode slurry into the dense electrolyte, creating a superior interface.

Incorporating an oxide type solid electrolyte in a roll-to-roll methodology would be rather challenging as the resulting electrolytes are mechanically rigid. For this reason, the prospect of coating an electrode directly onto the electrolyte is not scalable to industrial techniques. More plausible is separate fabrication of each component before final assembly. Proposed is two separate lines responsible for electrode fabrication via roll to roll manufacturing and separate electrolyte synthesis. Once the electrodes and electrolyte are rendered to the final specifications, they can be combined in a cell assembly area.

It should be noted that the processing environments for both electrode and electrolyte should be low humidity as both active material particles and oxide based solid electrolytes are susceptible to humid conditions. With the inclusion of oxide based solid electrolytes, metallic lithium becomes viable as an anode option. Metallic lithium would also command a dry, potentially inert, processing environment similar to the electrolyte and active material. Depending on the choice of processing environment, the use of metallic lithium may be responsible for an overall cost increase. With some risk mitigation however, the addition of a metallic lithium anode can improve the energy density considerably and should be pursued. Thus, it is recommended that lithium metal processing capabilities be included in this manufacturing paradigm. The most reasonable method of introducing a thin, cost effective, and pure metallic lithium anode would be through melt processing.

With the low melting point of lithium, a heated surface, ideally within an inert environment, could melt lithium and the partially fabricated cell would be placed in the melted material. The result would be a thin, uniform, layer of lithium to serve as the anode.

Although these processing techniques are straightforward, they are expensive. Cost reduction centered around electrolyte sintering is imperative in order to achieve a cost-effective production technique. It is recommended that this methodology be pursued along with cost reduction studies.

***Sulfide Based Electrolytes***

Sulfide based electrolytes have the highest reported ionic conductivities and do not require high temperature sintering, making them attractive candidates for solid state batteries. Although the potential for sulfide electrolytes is clear, there are clear processing concerns that make this technology difficult to scale to industrial methods. Current sulfide electrolyte fabrication techniques require argon filled environments to avoid generation of $H_2S$ gas and maintain a pristine sample surface. This technique also requires cell assembly in the same environment, resulting in cathode, anode, and cell housing materials all being transferred into the inert environment. On a bench top scale this is easily permissible, however when the speed and size of the operation is increased, the technique quickly becomes cumbersome.

Scaling up the manufacturing techniques for sulfide-based electrolytes would require a massive shift from conventional roll to roll manufacturing. Although electrodes could still be produced via roll-to-roll techniques, the rest of the assembly and synthesis would require new infrastructure, likely in the form of dry room type space, but with an inert atmosphere rather than low humidity. Within such an environment, human intervention would unethical and impractical, thus automated assembly would be required. Automated synthesis, processing, and assembly is not impossible but could introduce exorbitant cost. From construction of a dedicated inert room to the cost of purging and maintaining the atmosphere similar to how a glove box would operate, to the procurement and implementation of a fully automated assembly line, this method would quickly add considerable cost to production. For this reason, any increases in energy density would be offset by increases in processing cost. Although possible, the implementation of a full-scale sulfide electrolyte manufacturing line is not recommended.

## Processing Considerations

Unlike conventional LIBs, processing costs comprise the bulk of expenses associated with solid state LIBs. [21] As such, reducing production cost is the most effective approach for reducing overall cell cost. With intensive electrolyte production at the heart of the issue, any attempt to reduce time and energy associated with sintering and drying can be very advantageous. Although reducing production cost is a very clear goal, the associated methods are non-trivial. Electrolyte processing is complex and any change in structural or

stoichiometric composition can drastically affect performance. As a result, various aspects of production should be identified for improvement and investigated individually.

Improving processing of solid-state electrodes is critical to reducing cost while increasing quality. Several techniques have been investigated in some detail but warrant a full investigation. Improvement in one area would significantly impact how solid electrolytes are produced, but improvements in multiple area could be transformative. Each area of investigation could be framed into individual studies within a broader deep dive investigation and lead to multiple potential publication opportunities. In the following subsections various aspects of solid-state electrolytes are outlined and potential methods of improvement are described.

Proposed are several studies that can be undertaken independent of each other, but when evaluated together provide a comprehensive understanding of processing parameters. Each study aims at improving or implementing a specific aspect of the overall processing regime and will be investigated with bench top and pilot scale processing equipment. A timeline of twenty months is recommended, allowing four months for each individual study and four additional months for manuscript preparation.

***Low Temperature Sintering***

With much of the associated cost in solid electrolytes related to the processing and not the materials themselves, any reduction in sintering temperature or time would prove

economically beneficial. [21] Currently temperature as high as 1250 ℃ are used but preliminary success in lowering this temperature has been reported. [222] Reported is a technique to lower the treatment temperature of the solid-state reaction to 950 ℃ for 30 hours using $B_2O_3$ as an additive. Reducing the temperature may have detrimental effects on phase formation or structure as solid state synthesis is sensitive to changes in temperature. [226, 227] Alternatively, substitution of aluminum doping with the addition of tantalum has been shown to successfully produce LLZTO at a sintering temperature of 1000 ℃. [226] LLZTO also exhibits an impressive room temperature ionic conductivity of $3 \times 10^{-4}$ $Scm^{-1}$. [226] Before altering any parameter related to sintering temperature or time, a clearly defined processing technique should be established. Many similar techniques have been reported but comparing results from differing techniques adds in an unnecessary layer of complexity.

Along with temperature considerations, evaluating pressure changes on formation may also be beneficial. Varying pressures during synthesis may be able to effectively lower sintering temperature considerably while maintaining proper structural formation. Achieving the correct reaction energy via a combination of temperature and pressure can potentially reduce the required temperature for the reaction to proceed. An autoclave can be used to control both pressure and temperature on an industrial scale. Identifying the effect of pressure on phase formation and crystallinity can lead to cost savings if increased pressure results in an accompanying decrease in processing temperature.

Varying the temperature and pressure will impact the stoichiometry as well as the structure of the resulting ceramic and thus would need to be evaluated for proper composition. A variety of temperature and pressure combinations, with grounding in theory, should provide insight into the lowest cost sintering conditions that produce high quality solid electrolytes. Performing tests in an autoclave on a pilot scale can easily be scaled up to industrial autoclaves.

***Polymer and Ceramic Composite Electrolytes***

Polymer and ceramic type solid electrolytes have very different mechanical properties while maintaining small differences in ionic conductivities when operated at optimal conditions. Ceramic type electrolytes typically have greater ionic conductivities, whereas polymer type electrolytes have superior flexibility, combining these characteristics through a composite structure can leverage both qualities. [83] Polymer type electrolytes are also easier to infiltrate into electrode material due to the lack of a sintering step. Because the two types of electrolytes each have notable strengths in different areas, it is only natural to attempt to combine them in a way that exploits each strength. Combinations of these two electrolytes can take multiple forms, but they all have the same goal of maintaining flexibility while increasing ionic conductivity.

The appropriate approach for optimizing the combination of ceramic and polymer electrolytes goes far beyond simply grinding ceramic electrolytes and dispersing them in

polymer before curing. Although there is some evidence suggesting nano-sized particles are effective, the optimal processing conditions are not fully investigated but have been tied to particle size and concentration, suggesting both an optimal concentration and optimal particle size. [83, 251] Further, these two optimal parameters are not independent of each other, suggesting a family of particle sizes and concentrations that would be suitable. Regardless of particle size, compatibility with the electrode surface is required. With a fixed particle size for each electrode that differ between cathode and anode, compatibility with each particle may vary, finding an electrolyte particle size that is compatible with both cathode and anode structures will likely be non-trivial. This is further complicated when a lithium metal anode is introduced as some polymer electrolytes are not stable against lithium. [83]

Production method is also important when considering combining different types of electrolytes. Creating a free-standing electrolyte via tape casting, making what is known as a green tape, allows subsequent assembly of individual layers. Although straight forward, this method can potentially lead to interfacial issues when cycled as the electrodes will vary in size during cycling and may delaminate from the electrolyte. Introducing the electrolyte during electrode coating via dual slot die can create intimate contact as the two media will cure together creating intimate contact. Similarly, each slurry mixture can be coated separately, first coating the electrode and once cured, coating the electrolyte. This infiltration technique allows the electrolyte to penetrate the cathode structure creating a network within the electrode, improving ionic conductivity.

### *UV and E-Beam Curing*

When considering the cost of thermal drying for electrolyte and electrode material, a less expensive and more targeted technology can be used to speed the drying process. UV-curable polymers can be used in either electrode slurries or polymer electrolyte formulations and subsequently exposed to UV light to photo-initiate the curing process. [252] Not only does this technology remove the need for costly thermal heating, but it also speeds the drying process considerably, allowing for high throughput of material. Although this technology has obvious benefits, it also has major consequences. The use of UV light is non-trivial and demands increased safety precautions and equipment, which is followed by related expenses. This technique is also only practical with select binders, the binder in question must contain a photo-initiator in order to be compatible with UV-curing. Along with containing a photo-initiator, the binder must also be compatible with the respective medium it will be dispersed in. Solvent and active material considerations dominate the choice of binder in most cases and the selection of useable binders diminishes when more constraints are added to the system.

The use of UV curable binders is already prevalent in polymer electrolyte manufacturing and can easily be scaled for industrial purposes. However, some aspects of UV curing have been left unanswered. Proposed is an in-depth study aimed at determining optimal curing time and bean energy. Determining how effective co-curing can be is also an area of elevated interest. If both electrolyte and electrode could be cured at the same time, the

interfacial contact should be much greater. A systematic study answering some of these questions would help round out the understanding of UV- curable binders for use in lithium ion and solid-state batteries.

Although previously used in manufacturing applications, electron beam (e-beam) curing of materials is cost effective and fast technique for curing some polymer materials. This technique has proven useful in areas such as aerospace applications and can effectively replace thermal curing. [253] E-beam curing applications in LIBs have also shown success, replacing conventional binding agents with e-beam curable counterparts. [254] A common approach for manufacturing polymer electrolytes is UV-curing, requiring a photo-initiator. Using e-beam curable binders would eliminate the need for these materials and would allow for composite cathode- electrolyte structure to cured together as the penetration depth of e-beams exceeds that of UV techniques. Experiments focused on the infiltration and curing of polymer electrolytes in structured cathode materials can provide insight into how fast curing methods can be implemented in solid state manufacturing.

***Lithium Metal Anodes***

Lithium metal anodes have received a large amount of attention due to the potential energy density increases resulting from implementation. With a theoretical specific capacity of 3860 mAh/g, lithium metal has an entire order of magnitude greater capacity when compared to conventional graphite anodes. [199] Lithium metal can also solve the

volumetric changes and subsequent interfacial delamination that effects graphite and silicon anodes during cycling. With the promise of increased cell capacity also comes the reality of interfacial stability. Both sulfide and polymer electrolytes have exhibited interfacial instability when paired with lithium metal anodes. Some oxide electrolytes, such as LLZO doped with silicon or aluminum, have demonstrated better stability against lithium metal, but grain boundaries have been shown to be susceptible to dendritic formations. [21]

Deposition technique is also a major concern for lithium metal anodes. As lithium is sensitive to air and water, deposition of pure metallic lithium needs to be performed under inert conditions. Deposition techniques such as melt processing have created sufficient interfaces, but scalability is questionable. Physical Vapor Deposition (PVD) can be effective on small scale, but it's expensive and time-consuming nature make it incompatible with large scale applications. In situ formation, where excess lithium in the cell is used to plate a metallic lithium anode, is promising but it is unclear how uniform the resulting electrode is and if it is stable throughout the life span of the cell. Required is a deep dive into metallic lithium anodes for each solid electrolyte candidate. Combinations of electrolyte or surface treatments may prove beneficial to abate interface instability for sulfides and polymers and should be pursued.

## Evaluation Techniques

As improvements to processing are pursued, evaluation of these improvements needs to be quantitatively assessed. Determining what effects any individual change has on the production of solid-state electrolyte is critical to determining which changes to institute. Following are a series of techniques that can be used to evaluate various aspects of performance, from ion conductivity to structural formation. Employed together, this suite of tests can effectively determine superior production methods for solid state electrolytes. Each method does not specifically apply to every varied parameter of production, rather, the tests mentioned are applicable to the specific aspects of production and can be combined to provide a comprehensive understanding of the effects of changing processing parameters.

***Electrochemical Impedance Spectroscopy***

Interfacial and charge transfer resistance are crucial to the performance of any LIB, but for solid state cells in particular. Introducing a solid interface between the electrodes creates two additional interfaces that can increase overall cell resistance. Electrical Impedance Spectroscopy (EIS) can be used to determine the interfacial and charge transfer resistances within a cell. EIS is a non-destructive evaluation technique that can easily determine how additional interfaces lead to increased overall cell resistance, a critical issue associated with all solid-state electrolytes. As new formulations or constructions are pursued, evaluation of the internal resistance is vital to determining which configurations will be useful.

Ionic conductivity of solid electrolytes is temperature dependent and typically display higher values at elevated temperatures. Some electrolytes may exhibit lower ionic conductivities at room temperature than they would at an elevated temperature. An ideal electrolyte candidate would maintain a high room temperature ionic conductivity, removing the need for external heat sources to achieve optimal ionic conductivity. Combining EIS testing with variable temperature climate chambers provides an understanding of how each candidate electrolyte performs as a function of temperature.

***X-Ray Diffraction Analysis***

When manufacturing a solid electrolyte, confirmation of the structure is important to ensure proper formation. XRD gathers structural formation by using diffraction to determine interatomic distances. By comparing these recorded distances to empirical spectra, the structure of the material can be determined. When producing solid electrolytes such as LLZO, the ionic and electronic conductivity depend on the phase formation of the garnet type electrolyte. As temperature varies, structural formation also changes, making XRD an important qualifier of production technique. When altering sintering parameters for oxide based solid electrolytes, the use of XRD to monitor the structure will allow for optimization of processing parameters.

As temperature and pressure are varied during solid state reactions, reaction energies will differ and result in an alteration of structure or purity. As each temperature and pressure

are tested, XRD should be used to determine the phase purity of each sample. Once all samples have been tested, overall trends in phase purity can determine the optimal temperature and pressure parameters for producing oxide based solid electrolytes, such as LLZO.

***Neutron Scattering***

XRD can effectively determine most of the structural parameters of oxide or sulfide based solid electrolytes, but light elements, such as lithium, pose a challenge for this technique. [228] In order to determine the position of lithium in these structures a more sophisticated technique is required. Neutron scattering has a finer resolution when compared to XRD and thus can effectively identify lithium in the structure. These experiments can also be applied *in situ*, in order to understand ionic transport pathways. This technique, although not critical, can provide some valuable insight and should be performed if possible.

***Rate Capability***

For use in vehicle applications, solid state batteries must display acceptable high-rate discharge capacity. Cells are likely to experience discharge rates in excess of 2C-3C during acceleration and should also be compatible with fast charging currents in order to reduce overall charge time. By preforming rate capability testing, where the cell is subjected to increasing discharge rates as the charge rate is held constant, helps characterize each cells

ability to provide power when needed. After high-rate cycling, recovery cycles at a lower discharge rate can show to what extent irreversible reactions or mechanical degradation occurred.

***Long Term Cycling***

Solid state batteries may have the advantage of skipping a costly formation process depending on construction, however, this does not mean they are immune to side reactions or mechanical degradation. Particularly in the case of LLZO and lithium metal combinations, LLZO has been shown to be stable against metallic lithium anodes, but dendrites can still propagate along grain boundaries, typically rich in aluminum or silicon from processing techniques. Side reactions such as this do not compromise a cell immediately, rather it takes a sufficient number of cycles for the dendrite or other side product to form. Long term cycling coupled with postmortem assessment can determine what, if any, side reactions were present and how they contributed to cell failure.

Long term cycling is time consuming and requires both space and energy to conduct, however, it can provide insight in cell failure modes and determine an expected cycle life. By cycling cells to failure and subsequently analyzing reaction products and mechanical properties of the electrolyte and electrodes, the specific failure mode and contributing factors can be determined and lead to a better understanding of chemistry within the cell. Long term cycling should be complimented with techniques such as XPS and Raman in

order to determine chemical composition at each interface. Mechanical properties, such as adhesion and tensile strength of the electrolyte may also be insightful.

## Three Year Assessment

The field of solid-state lithium batteries is a quickly evolving and deeply dynamic field. Changes in any part of the state of the art can prove transformative of the area as a whole. If the recommended studies above are undertaken and have any success in furthering the implementation of solid-state lithium batteries, the impacts would be wide ranging. Within three years it is anticipated that lithium metal anodes can be successfully implemented with oxide solid electrolytes in order to improve energy density and safety of lithium based secondary storage batteries. It is also anticipated that the overall processing temperature, and subsequently cost, of oxide based solid electrolytes is considerably reduced. Although it is unlikely that one type of solid electrolyte will have a complete market share of the solid-state battery industry, it is likely that one will have a majority share of the marketplace. In three years' time it is likely that oxide based solid electrolytes, namely LLZO and closely related formulations, will comprise much of the research interest. Although oxide-based electrolytes will likely comprise a large percentage of the solid-state market, other types of solid electrolyte should still be investigated.

In three years, the aim of these prosed studies is to have optimized the anodic and cathodic structure and formulation for use in solid LIBs. Optimization of the electrolyte is a much

more arduous task that will unlikely be complete in three years. However, the implementation of solid electrolyte will likely be commonplace and have electrochemical results rivaling todays conventional LIB results. With current advancements in the state of the art, this goal is likely achievable, but it will require a concerted effort by multiple teams and sufficient funding to be successful.

# CHAPTER VII
# BENEFITS OF SOLVENT REPLACEMENT IN PEO BASED SOLID POLYMER ELECTROLYTES CONTAINING LITFSI

A version of this chapter will be submitted for publication by Alexander J. Kukay, Charl Jafta, Marm Dixit, Georgios Polizos, and Jianlin Li:

My contributions to this paper were 1) investigation design, 2) sample preparation, 3) data collection and analysis, and 4) writing. Charl Jafta provided research support and collected XPS data. Marm Dixit assisted in analysis of electrochemical results. Georgios Polizos provided significant research and analysis support and assisted in writing. Jianlin Li provided funding and assisted in the writing process.

## Abstract

Solid state electrolytes are gaining significant interest as the dangers of LIBs have become clear. This has resulted in a large shift of research interest to the production and optimization of various types of solid electrolytes, including solid polymer electrolytes. As these materials are typically produced using toxic solvents, there is a large potential to investigate the use of benign processing techniques developed initially for LIB applications. This study investigates the potential of aqueous processing or solvent free processing to replace the typically electrolyte production technique involving acetonitrile. Presented are comparable mechanical and electrochemical performance while also realizing a significant reduction in processing time and cost.

## Introduction

Lithium-ion batteries (LIBs) have become critical to every day operation and a major driver in the transformation of mobility in the past few decades. [1] With the prominence of electrified mobility and quickly developing applications of LIBs, safety of operation has become a major concern after several high-profile incidents in the past few years. [255-258] These risks are attributed to the flammability and potential for fire events associated with the liquid electrolyte that is typically employed in LIBs. Cells typically fail either due to manufacturing defects or dendritic growth causing separator breakthrough as the cell ages. The electrolyte has the potential to make a short-circuit failure into a much larger safety concern. [82] These safety concerns only increase as the size of the battery increases and as the vehicle market for LIBs in increasing at an astonishing rate, the need for energy storage technology that is intrinsically safe is clear. [195, 196]

As the risks associated with liquid electrolytes have become apparent, solid-state electrolytes have come back into favor for vehicle applications. Transitioning to solid-state electrolytes removes the risk of potential fire events associated with liquid electrolytes and can potentially lead to more environmentally benign cells by eliminating $LiPF_6$. [58, 259] Although solid-state electrolytes provide improve safety and mechanical properties and eliminate the need for a separator layer, they have yet to match the conductivity and electrochemical performance of liquid electrolytes. [197-202] Optimizing the electrochemical properties of solid-state electrolytes is crucial for implementation in

automotive applications and widespread adoption. Various types of solid electrolytes are currently under investigation for vehicle applications, some of which have already been commercialized. The three main types of solid electrolytes that are widely regarded as the most promising are polymer type electrolytes, solid garnet type electrolytes, and sulfur based solid electrolytes. [199, 203]

Polymer electrolytes are generally easier to produce and provide relatively high ionic conductivities. Typically, they are comprised of an ionically conductive lithium salt in an electronically insulating polymer matrix, such a polyethylene-oxide (PEO). [208, 214] This makes them a suitable candidate for replacing the conventional liquid electrolytes used today. Polymer electrolytes, however, have an increased susceptibility to dendritic breakthrough as they are amorphous in nature. [77] Although such breakthroughs would lead to safe failures, they pose an issue from a reliability standpoint. Polymer electrolytes also only exhibit ionic conductivities on the order of liquid electrolytes at elevated temperatures, which would be difficult to maintain in a package appropriately sized for vehicle use. [83, 201, 202, 213]

Garnet type solid electrolytes and sulfur based electrolytes are both dense electrolytes that are capable of withstanding dendritic breakthrough and as a result are areas of high research activity. [83] Although mechanically attractive, these electrolytes do not yet exhibit ionic conductivities that are competitive with polymer electrolytes. They require much more energy intensive processes to produce due to high temperature processing requirements

and material sensitivities. [21, 198, 199, 203-206] These are the main areas of research interest for lithium lanthanum zirconate $Li_7La_3Zr_2O_{12}$ (LLZO) type and sulfur-based electrolytes and have recently seen great improvements in both ionic conduction as well as processing optimization. Interfacial instability between the electrolyte and electrodes, either a lithium metal anode for maximum energy density or nickel rich transition metal oxide cathode have also proved difficult to mitigate for all three types of solid electrolytes. [198, 199, 203, 207, 260] The most likely solution to the solid-state electrolyte problems posed by polymer and ceramic types of electrolytes is a composite electrolyte that seeks to leverage the benefits of each electrolyte type while minimizing their detriments.

With polymer electrolytes readily producible, they are poised to play a large role in solid state batteries for the foreseeable future. These types of electrolytes however are typically produced using acetonitrile (ACN), a toxic substance that can be metabolized into cyanide among other hazard concerns. [261, 262] Not only are there safety risks associated with ACN, but there are also clear cost advantages as well. ACN based electrolytes are typically cast and allowed to cure for multiple days or weeks until fully set. [263, 264] This time-consuming process is not industrially viable on a large scale.

In an effort to both optimize the bis(trifluoromethanesulfonyl)imide (LiTFSI) content for increased ionic conductivity and implement a benign processing solvent, three different processing techniques are investigated in this work. First, the typical solvent, ACN, is used to cast electrolytes and is used for a baseline comparison. Second, deionized (DI) water as

a solvent coupled with freeze tape casting and hot pressing is utilized to obtain a benign electrolyte system as both PEO and the lithium salt lithium LiTFSI are miscible in water. [265] Freeze tape casting was employed to quickly and effectively sublimate the water out of the polymer matrix. Hot pressing was used to obtain a sufficiently dense electrolyte. Third, solvent is omitted entirely to determine if solvent free techniques are viable. Eliminating solvent entirely not only has the potential to reduce material cost, but also reduce processing time considerably. In all three cases, the lithium salt concentration was varied from 0 to 80 wt% while the PEO concentration in solvent was kept constant at 5 wt% to determine an optimum concentration for use in solid state batteries. As the choice of solvent has been shown to impact ionic mobility in the polymer electrolyte, the effects of solvent replacement on not only the mechanical but also electrochemical performance is of interest. [266] PEO and LiTFSI were chosen as the model system as PEO readily conducts metal ions and the lithium salt LiTFSI has been shown to be highly conductive ($10^{-3}$ S/cm$^2$ at 90 ℃) and stable against lithium metal. [267]

## Methods

### *Electrolyte Preparation*

Electrolyte solutions were prepared by mixing PEO (400,000 MW, Sigma Aldrich) with LiTFSI (99.95%, Sigma Aldrich) powders with the appropriate solvent. Both the PEO and LiTFSI powders were dried at 50 ℃ for 24 hours to ensure minimal excess water was

present before use in electrolytes. Either DI water (purified to 18 MΩ cm using a Milli-Q Direct 8 purifier) or acetonitrile (ACN, 99.999%, Sigma Aldrich) were added to the mixture. All samples had a fixed weight percentage of PEO at 5 wt%. Samples were then mixed overnight on a rolling mill to ensure homogenous distribution of the components. For solvent free samples, the dry powders were mixed for 5 minutes using a high-performance mixer (Retsch MM400). Acetonitrile samples were mixed with solvent and cast in a Teflon lined dish before being allowed to cure entirely at room temperature in a fume hood. This curing process took approximately two weeks in some cases. DI based samples were cast on Teflon in a freeze tape cast system (Glacigen) with a freeze bed temperature of -10 ℃. After two hours on the freeze bed, the samples were sublimated for 24 hours to ensure all water in the system was removed. This however left a porous electrolyte network which is not ideal for polymer electrolytes. To remedy this, DI samples were hot pressed at 100 ℃ using 5 kN of force, resulting in dense electrolyte approximately 100 μm thick in all cases. Solvent free samples were only hot pressed at 100 ℃ with 5 kN of force, skipping any curing or freeze tape casting procedure entirely. All samples were produced and stored in a dryroom with relative humidity 0.01% and dew point of -50 ℃.

***FTIR Characterization***

Chemical composition and bond formation was investigated using Fourier Transform Infrared Spectroscopy (FTIR, Bruker Alpha II). A wavenumber range of 4000 to 400 and

an average of 24 sweeps was used to obtain a single spectrum for each electrolyte sample. All samples were tested in a dry room to minimize water adsorption during testing.

***Cell Assembly and Ionic Conductivity Measurements***

Symmetric lithium|electrolyte|lithium coin cells were constructed for all samples to test the electrochemical performance of each electrolyte. Electrolytes were punched using an 18 mm punch and assembled between two 16 mm diameter lithium chips (MTI) and placed between two stainless steel spaces with a spring to apply even stack pressure. Since the electrolyte was larger in area than the lithium electrodes, the electroactive area used in later analysis was taken to be that of the lithium chips. The electrolyte was oversized to reduce the risk of edge contact between the metallic electrodes. Cells were assembled in an argon filled glovebox to preserve the lithium electrodes. Electrochemical impedance spectra from each cell were obtained from 300 kHz to 10 mHz with a 10 mV perturbation voltage using a VSP (Biologic, USA). All cells were tested at 65 ℃ after being allowed to acclimate for 6 hours. The ionic conductivity of each sample was calculated using the charge transfer resistance ($R_0$), the electroactive area ($A$), and electrolyte thickness ($l$) as shown in Figure 31. The resistance of the cell was determined via Electrochemical Impedance Spectroscopy (EIS) and subsequent fitting using a model cell, presented in Figure 31. Cells were allowed to acclimate at the given test temperature for at least two hours before EIS testing was performed. The electroactive area for each sample was taken to be the area of the lithium chip (16 mm diameter punch). The thickness of each sample was measured with a

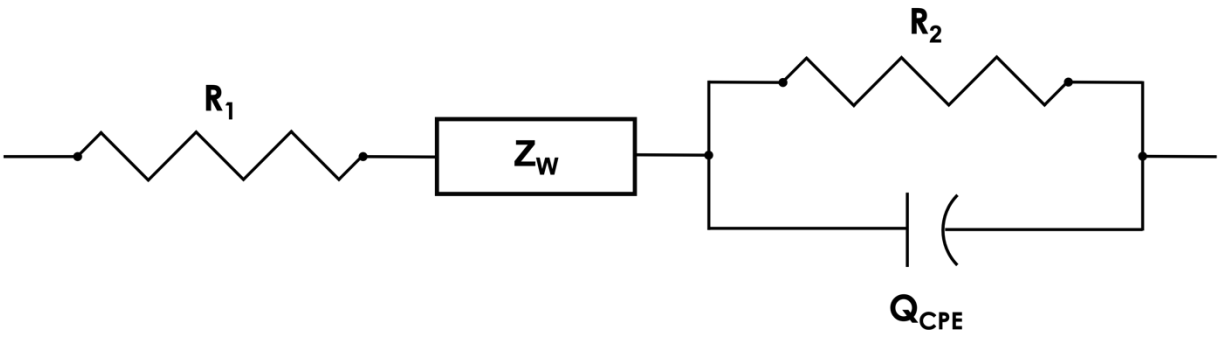


Figure 31: The model cell used to evaluate EIS spectra in order to calculate cell resistance for use in calculating transference numbers for each electrolyte.

micrometer. Conductivity was also measured via a permittivity analysis and is described in detail below.

***Dielectric Relaxation Spectroscopy***

Dielectric permittivity and conductivity values were calculated from EIS spectra obtained previously. Impedance values were used to calculate the real and imaginary components of the dielectric permittivity independently as given in Equation 16 and Equation 17 respectively. [268] Here $\omega$ is the angular angular frequency and is derived from the measured frequency ( $\omega = 2\pi\nu$) where $\nu$ is the frequency. Vacuum permittivity is represented by $\varepsilon_0$ and has a value of 8.85419 x $10^{-12}$ F/m. The real and imaginary components of the electrolyte impedance are given by $Z'$ and $Z''$ respectively and were obtained from the collected EIS data. The thickness and area of the electrolyte are represented by $l$ and $A$. As previously described, the thickness was measured with a micrometer and the electroactive area was calculated for the lithium chip with a radius of 8 mm. The dielectric loss tangent as also calculated and is given in Equation 18. [269]

Equation 16: $$\varepsilon' = \frac{l}{\omega\varepsilon_0 A}\frac{Z''}{(Z'^2+Z''^2)}$$

Equation 17: $$\varepsilon'' = \frac{l}{\omega\varepsilon_0 A}\frac{Z'}{(Z'^2+Z''^2)}$$

Equation 18: $$tan(\delta) = \frac{\varepsilon''(\omega)}{\varepsilon'(\omega)}$$

Real and imaginary components of conductivity as a function of the angular frequency $(\omega)$ of the films was similarly calculated via Equation 19 and Equation 20 respectively. [270]

Equation 19: $$\sigma'(\omega) = \omega\varepsilon_0\varepsilon''(\omega)$$

Equation 20: $$\sigma''(\omega) = \omega\varepsilon_0\varepsilon'(\omega)$$

***Stripping Platting Measurements***

Stripping and platting measurements were performed current densities 5, 10, 20, 50, 100, 200, and 500 μA/cm$^2$, with each current density being applied for 1 hour alternating 5 positive and 5 negative pulses for a total of 10 total pulses per current density. Each current density was applied for 1 hour each and all samples were tested at 65 ℃. Only samples with a molar ratio of 29:1 EO:Li was used for the stripping platting measurements as the conductivities of these samples was determined not only to be the highest regardless of preparation technique, but are also comparable in magnitude to each other.

Additionally, long term stripping platting measurements were performed at 50 μA/cm$^2$ to monitor the increase in polarization as the electrolytes continue to cycle. Cells were tested for 100 total hours. 50 μA/cm$^2$ was chosen as polarization differences were observed between electrolyte preparation technique beginning at this current density. Similarly, all long term testing was performed at 65 ℃.

## Results and Discussion

### *FTIR Characterization*

Measured FTIR spectra for each sample are shown in Figure 32 (a)-(c). A sample spectrum for pure PEO powder and pure LiTFSI powder are also provided in at the bottom of each pane. For each preparation method the LiTFSI signal gradually increases as the weight ratio of LiTFSI is increased. This is expected as the relative signal will reflect the relative composition. Provided at the top and bottom of each cluster of signals are reported peak positions for PEO and LiTFSI respectively. The dotted lines at 840 cm$^{-1}$, 960 cm$^{-1}$, 1074 cm$^{-1}$, 1102 cm$^{-1}$, 1233 cm$^{-1}$, and 1342 cm$^{-1}$ represent the C-O stretching, $CH_2$ asymmetric stretching, C-O-C asymmetric, C-O-O symmetric stretching, $CH_2$ symmetric, and CH2

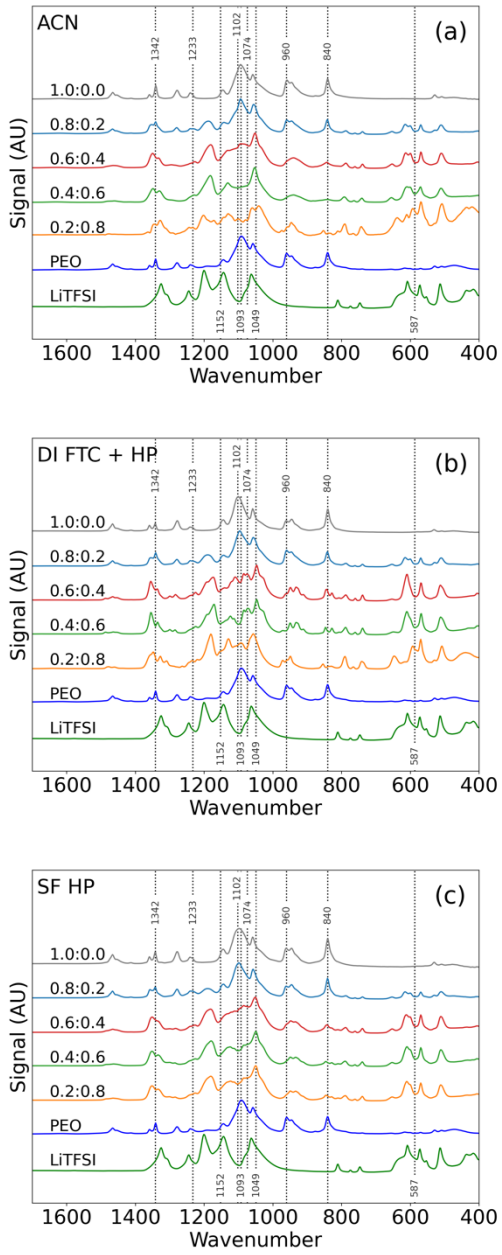


Figure 32. FTIR spectra of a) acetonitrile processed samples, b) DI freeze tape cast and hot-pressed samples, and c) solvent free hot-pressed samples.

bending modes respectively as reported in literature. [271-275] Below the spectra are similar characteristic peaks for LiTFSI. These peaks are denoted by dotted lines as well at wavenumbers of 587 $cm^{-1}$, 1049 $cm^{-1}$, 1093 $cm^{-1}$, and 1152 $cm^{-1}$ for the $CF_3$ asymmetric bending, S-N-S asymmetric stretching, S=O bonding, and C-$SO_2$-N bonding modes of LiTFSI. [276] The spectra obtained are not only in good agreement with previously reported values, but they are also unaffected by either the change in salt concentration or the change of processing methodology. The bending, stretching, and bonding modes of both the polymer host and lithium salt being unaffected is expected as there is no evidence for an adverse reaction or deterioration at the composition is varied. However, these peaks demonstrate that the mechanical properties of both PEO and LiTFSI are not affected by processing methodology and is a promising result.

The ability of PEO and LiTFSI to be processed in water without sacrificing mechanical properties provides evidence that commonly used toxic ACN can be replaced in favor of a benign processing solvent. Furthermore, samples processed with no solvent at all display comparable mechanical properties to those processed with solvent. This suggest that hot pressing is sufficient to lead to desirable polymer behavior. Considering typical ACN based processing can take multiple weeks to produce a thin film, transitioning to a DI based processes with freeze tape casting to ensure adequate water removal can save considerable amounts of time. [264] More time can be saved by eliminating solvent entirely as solvent free samples were produced in under 5 minutes and can be readily scaled to a roll-to-roll application through the use of hot calendering. From a mechanical standpoint, a strong

argument exists for replacement of ACN. This assumes adequate or improved electrochemical performance follows and is investigated in the following sections.

### *Ionic Conductivity Measurements*

Ionic conductivity increases considerably when small amounts of lithium salt are added as the charge carrier concentration becomes higher. This is shown in Figure 33, as the LiTFSI concentration is increased from 0 wt% to 20 wt%, the ionic conductivity increases from below $10^{-6}$ S/cm to more than $10^{-4}$ S/cm at 65 °C for all preparation techniques. Although the ionic conductivity increases with increasing salt concentration initially, the ionic transport in polymer electrolytes is a function of segmental motion of the polymer and this mechanism is slowed at higher salt concentrations. [277] This results in a reduction in ionic conductivity as the salt concentration is increased. This decrease is also an effect driven by the ion pairing effect that occurs at higher salt, and consequently ion, concentrations. [271] This is observed as the ionic conductivity steadily decreases from the maximum of $10^{-4}$ S/cm at an EO:Li ratio of 26:1 to less $10^{-5}$ S/cm above EO:Li ratios of 4:1. This trend is consistent across all preparation techniques, suggesting the interactions between ether oxygens and lithium ions is not affected by solvent choice or preparation method. As trends in the conductivity appear to be agnostic of preparation technique, the argument for solvent replacement in favor of dry mixing and hot pressing becomes stronger. Not only do samples produced without solvent show comparable ionic conductivities across a wide range of salt

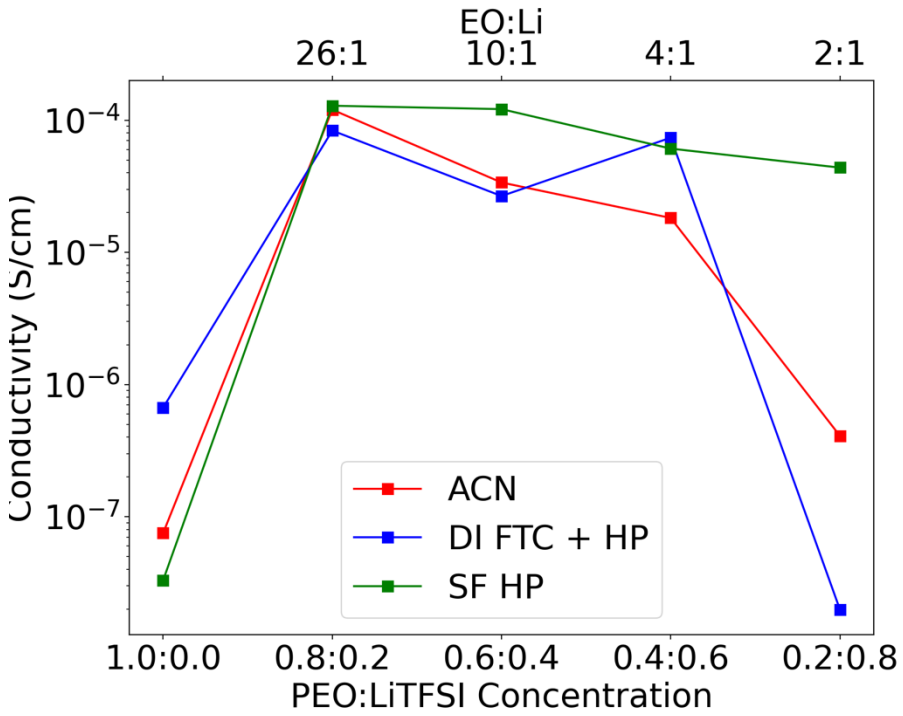


Figure 33. Calculated ionic conductivities for each solvent presented as a function of salt concentration and EO:Li.

concentrations, but they also show improved performance in most cases. Since ionic conductivity is not the only concern when investigating conduction methods in solid polymer electrolytes, the performance of all samples is further investigated via dielectric relaxation spectroscopy (DRS).

***Dielectric Relaxation Spectroscopy***

The real and imaginary components of dielectric permittivity along with dielectric loss are shown in Figure 34. It can be seen from the imaginary component of permittivity that all samples are dominated by conduction, which is expected at the tested temperature. Within the frequency range investigated, the only identifiable relaxation mode is the Maxwell-Wagner-Sillars (MWS) polarization. At the temperatures tested, the high frequency response did not contain alpha or beta relaxation modes and was not successfully fit using the Debye, Cole and Cole, Cole and Davidson, or Havriliak-Negami methods. [278-280] Varying the test temperature to obtain an Arrhenius response and extending the frequency range beyond the 300 kHz limit investigated here would assist in accurately modeling the relaxation response. The limitations of the frequency analyzer used did not allow for higher frequencies to be investigated and consequently the relaxation was not able to be fully modeled.

A power law relation was applied to conductivity data within a range of 50 Hz to 8 kHz for most cases. In two cases (ACN 0.6:0.4 and CAN 0.4:0.6) slightly more constrictive bounds

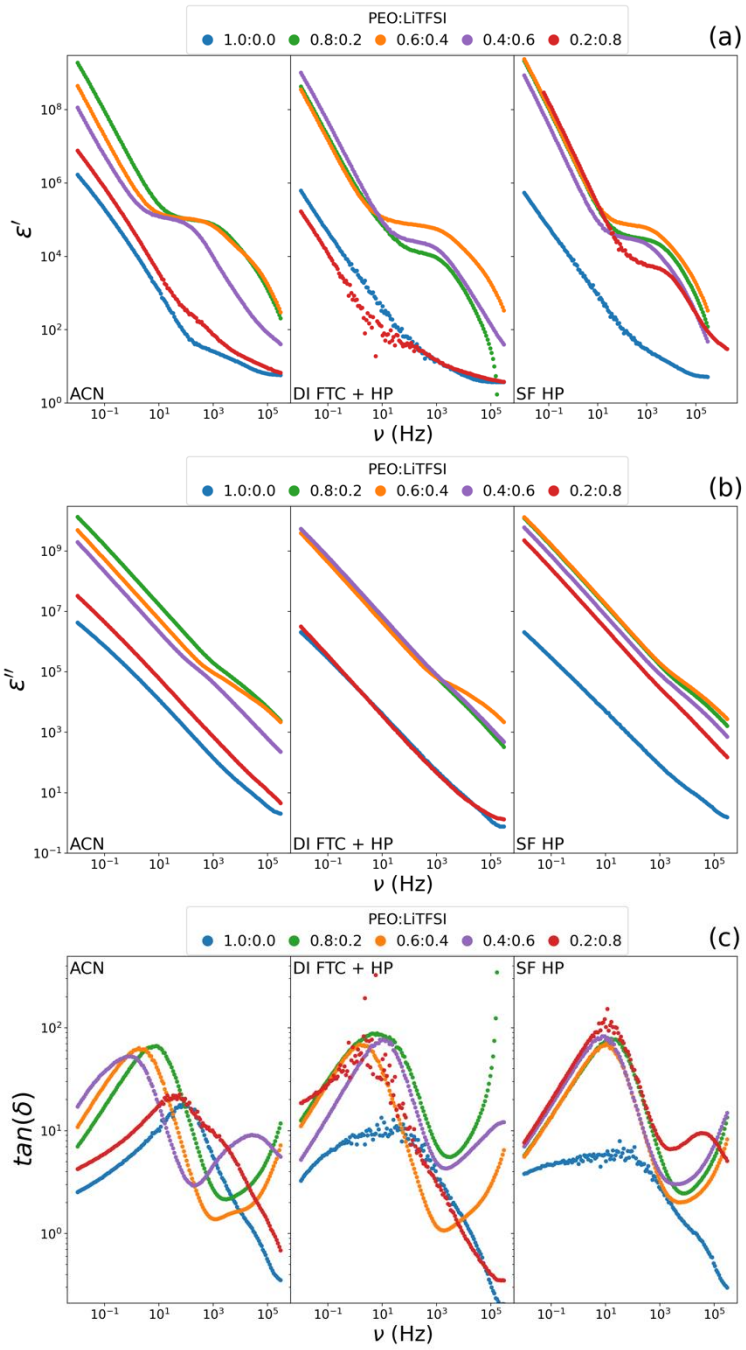


Figure 34. Calculated trends for (a) the real component of dielectric permittivity, (b) the imaginary component of dielectric permittivity, and (c) the calculated dielectric loss tangent for all samples.

were applied. High and low frequency bounds were applied to avoid high and low frequency regions where the power law relation is not entirely valid. This relation is given in Equation 21. [281-283] Where is the $\sigma_{dc}$ dc ionic conductivity, $A$ is an arbitrary perfector, and $n$ is the fractional exponent. In all cases the data is accurately modeled by the low frequency conductivity response ($\nu < 20$ x $10^3$ Hz) that is independent of frequency and a frequency dependent contribution at higher frequencies. This model is commonly referred to as so called universal dynamic response (UDR) of the system. [283]

Equation 21: $$\sigma'(\omega) = \sigma_{dc} + A\omega^n$$

Results from this model fit as well as the calculated real component of the conductivity as a function of frequency is show in Figure 35 (a). Parameters for the fits applied are shown in Figure 35 (b) as well as in Table 10. The calculated dc conductivity is in good agreement with conductivity measurements calculated previously using charge transfer resistance as shown in Figure 33. Furthermore, although the dc conductivity calculated for the 0.8:0.2 PEO: LiTFSI samples for ACN and SF HP preparations are nearly identical, the highest dc conductivity calculated was actually for the 0.6:0.4 SF HP sample. Solvent free samples also have the lowest range of dc ionic conductivities compared to both the ACN and DI FTC HP samples.

A clear frequency independent dc conductivity signal can be seen for all samples showing a wide operating range that is frequency independent. The ionic conductivity at high

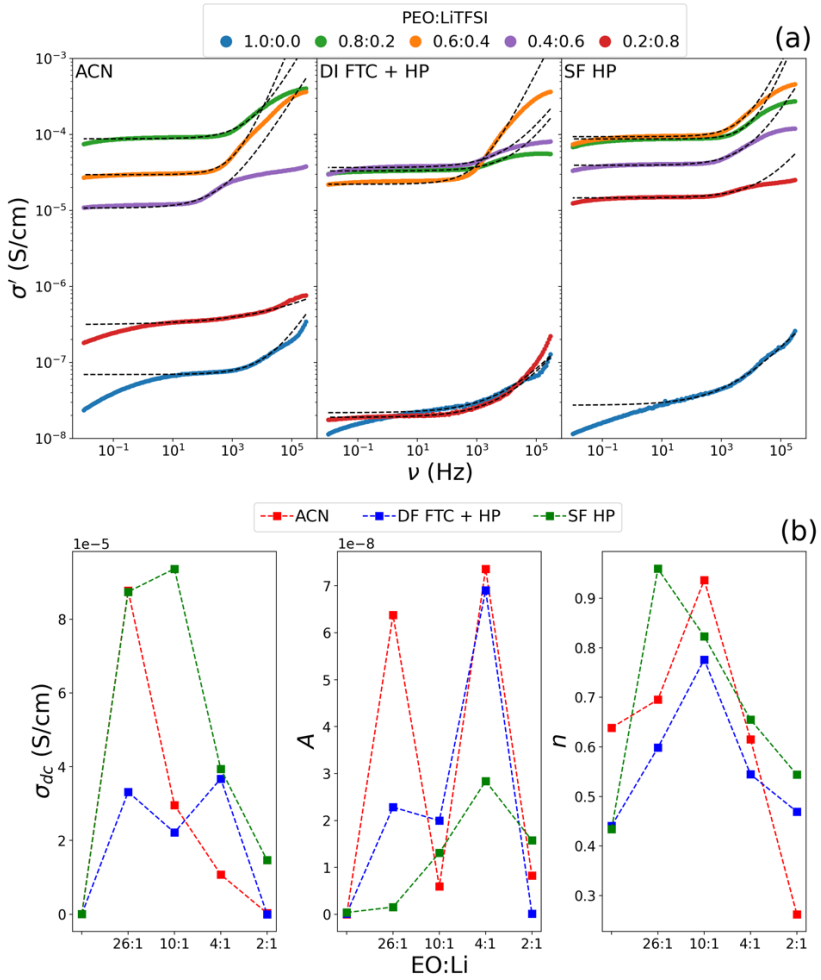


Figure 35. Plots showing (a) derived conductivity as a function of frequency with a fit applied along with (b) calculated fit parameters applied to the derived conductivity data.

Table 10: Calculated conductivity power law fit parameters.

| Preparation | PEO:LiTFSI Weight Ratio | EO:Li Ratio | $\sigma_{dc}$ (S/cm) | $A$ | $n$ |
|---|---|---|---|---|---|
| ACN | 1.0:0.0 | - | 6.94E-08 | 3.55E-11 | 6.39E-01 |
| | 0.8:0.2 | 29:1 | 8.77E-05 | 6.38E-08 | 6.95E-01 |
| | 0.6:0.4 | 10:1 | 2.96E-05 | 5.96E-09 | 9.37E-01 |
| | 0.4:0.6 | 4:1 | 1.08E-05 | 7.36E-08 | 6.16E-01 |
| | 0.2:0.8 | 2:1 | 3.13E-07 | 8.26E-09 | 2.62E-01 |
| DI FTC + HP | 1.0:0.0 | - | 2.18E-08 | 1.72E-10 | 4.41E-01 |
| | 0.8:0.2 | 29:1 | 3.32E-05 | 2.28E-08 | 5.98E-01 |
| | 0.6:0.4 | 10:1 | 2.22E-05 | 2.00E-08 | 7.76E-01 |
| | 0.4:0.6 | 4:1 | 3.68E-05 | 6.90E-08 | 5.45E-01 |
| | 0.2:0.8 | 2:1 | 1.90E-08 | 1.10E-10 | 4.69E-01 |
| SF HP | 1.0:0.0 | - | 2.74E-08 | 4.01E-10 | 4.34E-01 |
| | 0.8:0.2 | 29:1 | 8.74E-05 | 1.55E-09 | 9.59E-01 |
| | 0.6:0.4 | 10:1 | 9.37E-05 | 1.31E-08 | 8.23E-01 |
| | 0.4:0.6 | 4:1 | 3.94E-05 | 2.84E-08 | 6.55E-01 |
| | 0.2:0.8 | 2:1 | 1.47E-05 | 1.57E-08 | 5.44E-01 |

frequency ($\nu > 10$ x $10^3$ Hz) for all samples exhibits an upward trend, modeled by the power law portion of Equation 21. The fit parameter $n$ exceeds 0.5 for almost all samples, suggesting the concentration of mobile ions is moderate to high in all samples. [282] This also suggests that ion-hopping becomes more prominent in various samples as $n$ approaches unity. [271] Maximum values of $n$ are observed at EO:Li ratios of 26:1 for the solvent free samples and 10:1 for samples produced with either ACN or DI as the solvent. This is in good agreement with the ion-hopping mechanism as the salt concentrations will directly impact the sites available for ion interactions. Interestingly the maximum $n$ does not occur at the same EO:Li ratio for all preparation techniques, suggesting increased interaction sites when solvent is used to produce these electrolytes.

Furthermore, the onset of the upward trend occurs at different frequencies for various samples. As seen in Figure 35 ACN based samples display a consistent increase in onset frequency, increasing from 27 Hz to 220 Hz to 500 Hz for 0.4:0.6 (purple), 0.6:0.4 (orange), and 0.8:0.2 (green) PEO:LiTFSI ratios respectively. A similar trend is observed for DI samples, however in this case the onset frequency of the 0.8:0.2 PEO:LiTFSI composition is considerably lower than that of the 0.4:0.6 and 0.6:0.4 compositions, 127 Hz compared to 400 Hz and 350 Hz respectively. Solvent free samples exhibit generally high onset frequencies with the 0.8:0.2 (green) PEO:LiTFSI concentration being upwards of 1600 Hz. This implies the dc conduction mechanism is active over a wide range of frequencies and ion-hopping is not as easily induced in the solvent free samples as compared to the other two preparation techniques.

***Stripping Platting Measurements***

Stripping and platting results shown in Figure 36 indicate that below a current density of 50 μm/cm$^2$ the polarization of all cells is similar across perpetration techniques. Only when the current density is increased to 50 μm/cm$^2$ and beyond differences in polarization at noticed. The solvent free SF HP (green) sample displays a polarization that is larger than that of the samples produced with solvent. Samples produced with either solvent show comparable polarization at all current densities, suggesting a better degree of salt dispersion with samples that utilize solvent as a means of distribution. The voltage profiles in all cases and at all current densities is symmetric, a dotted line at 0 mV has been added to aid the reader in observing the symmetry. This indicates that the ion transfer through each sample is reversable. At a current density of 500 μm/cm$^2$ the solvent free sample displays a lower polarization, but closer inspection suggests the cell is beginning to fail via dendritic breakthrough. The noisy signal and reduction in polarization are clear indicators the cell is no longer functioning as intended. Thus, this decrease in polarization is not thought to be real. What is clear, is that at all current densities each preparation technique results in highly comparable performance. Even though the solvent free (green) trend is shown to slightly underperform the samples prepared with either ACN or DI, the time and equipment cost savings realized by eliminating solvent from the production method provide a strong argument for pursuing and further optimizing such a technique.

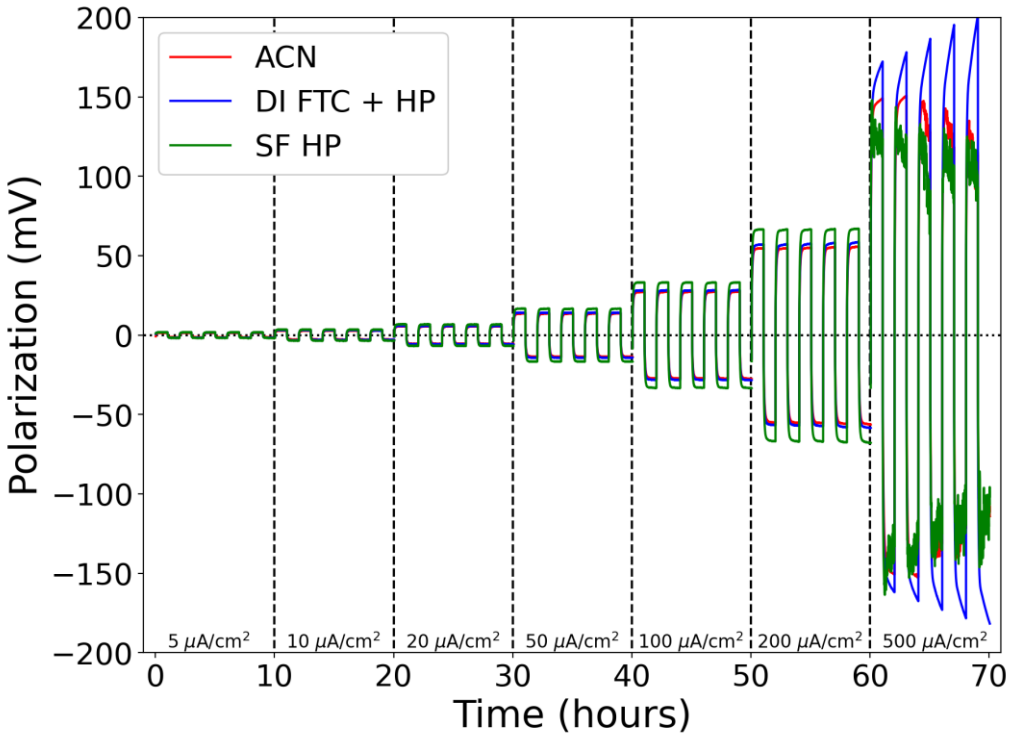


Figure 36. Striping and plating data at various current densities. Each current density is separated by a dashed vertical line and the corresponding current density is listed near the bottom of the figure.

Long term stripping and platting is shown in Figure 37. Here each sample is tested with a current density of 50 $\mu A/cm^2$ to observe the response over a wide time range. Initially all three samples exhibit similar polarizations with the DI sample (blue) having a larger polarization compared to either the solvent free (green) or ACN (red) based samples. The polarization of both the solvent free and ACN based samples remains relatively constant as the cells continue to cycle, occasionally developing soft shorts that lead to a reduction in polarization. These soft shorts appear to heal themselves as the cell continues to age. In the case of the DI based sample however, the polarization steadily increases as the cell ages, indicating an unstable interface between the lithium metal and electrolyte film. This is likely due to excess residual water that is potentially present in this sample. Although sublimation experienced during the freeze tape casting process removed most of the water, there is likely tightly bound water that has remained. This leads to interfacial instability and subsequent increases in polarization. This indicates the film drying process could be further optimized to avoid this side reaction but remains a promising technique and a good candidate for further development.

## Conclusions

Three different preparation techniques for PEO and LiFTSI containing electrolytes were investigated for mechanical and electrochemical performance. These three preparation techniques were the typical two-week ACN based casting and curing approach, a DI based freeze tape cast and hot press technique, and a solvent free hot press only technique. Each

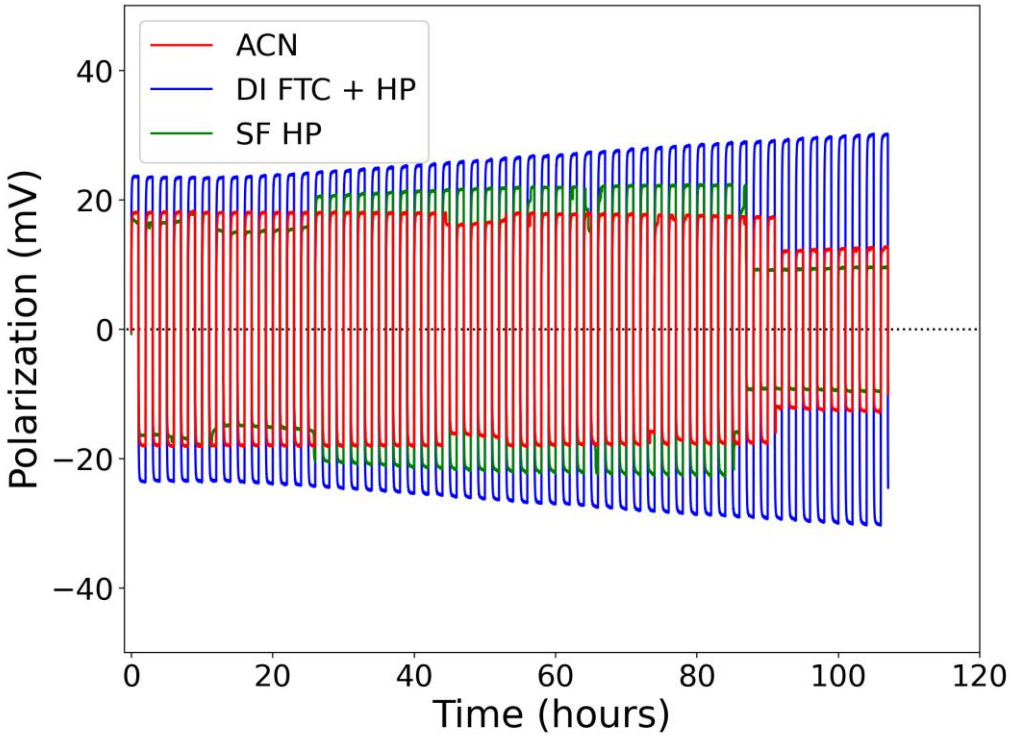


Figure 37. Striping and plating at 50 μA/cm$^2$ for the first 100 hours for each electrolyte film preparation technique.

technique was evaluated across a wide range of salt concentrations. FTIR results show a minimal impact on bond formation between each preparation technique as well as a similar response to increasing salt concentrations across all solvents.

Electrochemically each preparation technique resulted in comparable performance. Ionic conductivities followed an expected trend with an initial increase in ionic conductivity as salt is added in small amounts, followed by a decrease in conductivity as the salt concentration is further increased. This decrease is due to ion paring that limit the efficiency of the conduction and is a function of the dispersion of the lithium salt. Further investigating the permittivity and ionic conductivity as a function of frequency via DRS confirms the superior ionic conductivity of solvent free samples.

Finally, stripping and platting measurements across a wide range for current densities show comparable performance across all preparation techniques for the sample with the highest ionic conductivity, which was found to be the same salt concentration for each preparation technique. Both the DI and solvent free samples exhibited poorer performance at the highest current density, suggesting the cells were deteriorating as dendritic growth progressed.

Evidence has been provided making a case for replacing ACN with either DI as the solvent or eliminating the solvent entirely. The economic and environmental benefit for solvent replacement is clear and the mechanical and electrochemical performance of samples

produced via these techniques has been demonstrated. With solid polymer electrolytes set to become a significant part of the energy storage market, transitioning to environmentally benign processing techniques can save a considerable amount of time and energy without sacrificing performance.

# CONCLUSION

This dissertation explores the development and optimization of aqueous processing as applied to ultra-thick electrodes made with nickel rich cathode active material. As the battery community continually strives for increased performance through material improvements and novel electrode structures, the need for a benign processing methodology should not be overlooked. As the typically solvent (NMP) is quickly being revaluated in terms of legality and is slated to be banned in various countries, exploring the relationship between DI water and electrode processing is an area of research that is quickly expanding and can revolutionize the field of electrode processing. Further, with more batteries in production that ever before, the environmental footprint of battery manufacturing has the potential to negate all environmental benefits realized from the technology if the manufacturing processes are not set up in an environmentally conscious manner.

Chapter 3 explored the ability to produce ultra-thick electrodes produced with nickel-rich cathode active material (NMC 811). The addition of small amounts of mild acid (phosphoric acid) was able to reduce a well-known corrosion reaction and lead to improved mechanical and electrochemical performance. Although electrochemical performance was still poor compared to NMP processed counterparts, mechanically robust electrodes on the order of 8 $mAh/cm^2$ had never before been practical to produce via aqueous processing due to the severe side reactions that had limited electrode thickness. Presenting a cost effective, in-line solution enables continued evaluation of such thick electrodes and paving the way to increased adoption of this processing technique.

With ultra-thick aqueous processed cathodes now achievable from the results of Chapter 3, the improvement of performance for these electrodes was investigated in Chapter 4. The performance of LIBs has long been dependent on the energy density of the cell. The simplest way to increase the energy density of a battery pack is to increase the thickness of the electrode and reducing the number of inactive components required. This however leads to mass-transport limitations throughout the electrode and quickly leads to diminishing returns. Chapter 4 investigated the use of various electrode architectures to determine the optimal configuration for improved high discharge capacity. Not only was an optimal structure identified, but the impact of particle size distribution on solid and liquid phase ionic diffusion was identified. Results show that a mixture of small and large active material particles near the current collector surface and only small active material particles near the separator result in the best balance of available electro-active surface area and non-constrictive pores. This result shows a potential for improved discharge capacities utilizing the same techniques that are currently in place.

Chapter 5 investigated electrode performance for NMP and DI samples dried at various temperatures. Inhomogeneous binder distributions have long plagued electrode processing techniques, especially aqueous processed variants. Electrochemical performance and binder distribution were investigated as a function of drying temperature. A chemical engineering model was applied to data collected during the drying process and a strong temperature dependance on the drying mechanics of DI processed samples was identified. This dependence was much less significant for the NMP processed samples, suggesting a

tunable drying regime exists for aqueous processed cathodes. This dependance resulted in vastly different heat transfer rates from the environment to the electrode and explains the impact of drying temperature on binder distribution in aqueous processed cathodes. Results indicate that a two-stage drying regime consisting of a carefully selected initial drying temperature followed by a high temperature would lead to optimized binder distribution and large cost savings for electrode drying. The initial drying stage would facilitate the optimal distribution of the polymetric binder while the second stage would quickly remove excess solvent after the critical pore network has been established. Implementing such a technique would not only reduce energy cost associated with electrode drying, but also lead to direct capital equipment savings through the reduction of drying time and equipment required.

Chapter 7 is a departure from aqueous processing as applied to LIBs and focuses on applying benign processing to solid state electrolytes. As the safety issues related to LIBs are abundantly clear, the research interest in solid electrolytes is at the forefront of energy storage research. Replacing toxic solvents used in the production of polymer electrolytes not only reduces potential adverse effects of working with ACN but leads to significant time and cost savings. The mechanical and electrochemical properties of solid polymer electrolytes processed with benign solvents were compared to the conventional production technique. Not only were samples generally comparable in performance, but samples also processed with no solvent outperformed the baseline technique in many cases. These results all suggest the state of the art of solid polymer electrolytes is a prime candidate for

optimization. As the field of solid-state electrolytes continues to grow at an extreme rate, transitioning to a benign processing method can result in a vast reduction in production cost and toxic solvent use.

Overall, this dissertation has made several arguments for the benefits of aqueous processing while addressing concerns associated with the technique. Advancements have been demonstrated and challenges identified. As the fields of LIB and solid-state electrolyte production continue to be relevant, the need for benign processing approaches will be high. As the transition from ICEs to electric vehicles is only expected to increase in speed, the need to address the environmental and economic impact of production is paramount. It is shown in this dissertation that the way forward can and should be aqueous based.

# REFERENCES


1. Li, J.L., C. Daniel, and D. Wood, *Materials processing for lithium-ion batteries.* Journal of Power Sources, 2011. **196**(5): p. 2452-2460.
2. Hawley, W.B. and J.L. Li, *Electrode manufacturing for lithium-ion batteries-Analysis of current and next generation processing.* Journal of Energy Storage, 2019. **25**: p. 100862.
3. Scott Oldham, A.I. *Here's Every New Electric Vehicle Model for Sale in the U.S.* 2021; Available from: https://www.caranddriver.com/shopping-advice/g32463239/new-ev-models-us/.
4. Emily A. Shrider, M.K., Frances Chen, Jessica Semega. *Income and Poverty in the United States: 2020*. 2021; Available from: https://www.census.gov/library/publications/2021/demo/p60-273.html.
5. House, T.W. *FACT SHEET: President Biden Announces Steps to Drive American Leadership Forward on Clean Cars and Trucks*. 2021 [cited 2021 August, 14]; https://www.whitehouse.gov/briefing-room/statements-releases/2021/08/05/fact-sheet-president-biden-announces-steps-to-drive-american-leadership-forward-on-clean-cars-and-trucks/].
6. Hawkins, T.R., et al., *Comparative environmental life cycle assessment of conventional and electric vehicles.* Journal of industrial ecology, 2013. **17**(1): p. 53-64.
7. Howell, D., *Fiscal Year 2019 Annual Progress Report for Energy Stroage R&D.* U.S. Department of Energy, Office of Energy Efficiency and Renewable Energy, Vehicle Technologies Office, 2019.
8. Ellingsen, L.A.W., et al., *Life cycle assessment of a lithium-ion battery vehicle pack.* Journal of Industrial Ecology, 2014. **18**(1): p. 113-124.
9. Curry, C., *Lithium-ion battery costs and market.* Bloomberg New Energy Finance, 2017. **5**: p. 4-6.
10. Wood, D.L., et al., *Technical and economic analysis of solvent-based lithium-ion electrode drying with water and NMP*. Drying Technology, 2018. **36**(2): p. 234-244.
11. Bai, Y.C., et al., *Sustainable recycling of cathode scraps via Cyrene-based separation.* Sustainable Materials and Technologies, 2020. **25**: p. e00202.
12. Wood Iii, D.L., J. Li, and C. Daniel, *Prospects for reducing the processing cost of lithium ion batteries.* Journal of Power Sources, 2015. **275**: p. 234--242.
13. Wood, M., et al., *Chemical stability and long-term cell performance of low-cobalt, Ni-Rich cathodes prepared by aqueous processing for high-energy Li-Ion batteries.* Energy Storage Materials, 2020. **24**: p. 188-197.
14. Kukay, A., et al., *Aqueous Ni-rich-cathode dispersions processed with phosphoric acid for lithium-ion batteries with ultra-thick electrodes.* J Colloid Interface Sci, 2021. **581**(Pt B): p. 635-643.
15. Sahore, R., et al., *Towards Understanding of Cracking during Drying of Thick Aqueous-Processed LiNi0.8Mn0.1Co0.1O2 Cathodes.* Acs Sustainable Chemistry & Engineering, 2020. **8**(8): p. 3162-3169.

16. Carvalho, D.V., et al., *Study of Water-Based Lithium Titanate Electrode Processing: The Role of pH and Binder Molecular Structure.* Polymers (Basel), 2016. **8**(8): p. 276.
17. Liang, Y.H., et al., *Life cycle assessment of lithium-ion batteries for greenhouse gas emissions.* Resources Conservation and Recycling, 2017. **117**: p. 285-293.
18. Zackrisson, M., L. Avellan, and J. Orlenius, *Life cycle assessment of lithium-ion batteries for plug-in hybrid electric vehicles - Critical issues.* Journal of Cleaner Production, 2010. **18**(15): p. 1519-1529.
19. Tolomeo, R., et al., *Application of Life Cycle Assessment to Lithium Ion Batteries in the Automotive Sector.* Sustainability, 2020. **12**(11): p. 4628.
20. Gastol, D., et al., *Microstructural design of printed graphite electrodes for lithium-ion batteries.* Materials & Design, 2021. **205**: p. 109720.
21. Schnell, J., et al., *Prospects of production technologies and manufacturing costs of oxide-based all-solid-state lithium batteries.* Energy & Environmental Science, 2019. **12**(6): p. 1818-1833.
22. Li, J.L., et al., *Superior Performance of LiFePO4 Aqueous Dispersions via Corona Treatment and Surface Energy Optimization.* Journal of the Electrochemical Society, 2012. **159**(8): p. A1152-A1157.
23. An, S.J., et al., *Fast formation cycling for lithium ion batteries.* Journal of Power Sources, 2017. **342**: p. 846--852.
24. Zhao, H., et al., *Cobalt-Free Cathode Materials: Families and their Prospects.* Advanced Energy Materials, 2022: p. 2103894.
25. Hays, K.A., et al., *Si Oxidation and H2 Gassing During Aqueous Slurry Preparation for Li-Ion Battery Anodes.* The Journal of Physical Chemistry C, 2018. **122**(18): p. 9746--9754.
26. Buqa, H., et al., *Study of styrene butadiene rubber and sodium methyl cellulose as binder for negative electrodes in lithium-ion batteries.* Journal of Power Sources, 2006. **161**(1): p. 617-622.
27. Lux, S.F., et al., *Low Cost, Environmentally Benign Binders for Lithium-Ion Batteries.* Journal of the Electrochemical Society, 2010. **157**(3): p. A320-A325.
28. Bauer, W., et al., *Effects of pH control by acid addition at the aqueous processing of cathodes for lithium ion batteries.* Electrochimica Acta, 2019. **317**: p. 112-119.
29. Maleki, H., et al., *Thermal Stability Studies of Binder Materials in Anodes for Lithium-Ion Batteries.* Journal of the Electrochemical Society, 2000. **147**(12): p. 4470.
30. Du Pasquier, A., et al., *Differential scanning calorimetry study of the reactivity of carbon anodes in plastic Li-ion batteries.* Journal of the Electrochemical Society, 1998. **145**(2): p. 472.
31. Chen, H., et al., *Exploring Chemical, Mechanical, and Electrical Functionalities of Binders for Advanced Energy-Storage Devices.* Chem Rev, 2018. **118**(18): p. 8936-8982.
32. Duan, J., et al., *Building Safe Lithium-Ion Batteries for Electric Vehicles: A Review.* Electrochemical Energy Reviews, 2020. **3**(1): p. 1-42.

33. Courtel, F.M., et al., *Water-soluble binders for MCMB carbon anodes for lithium-ion batteries.* Journal of Power Sources, 2011. **196**(4): p. 2128-2134.
34. Doberdò, I., et al., *Enabling aqueous binders for lithium battery cathodes--Carbon coating of aluminum current collector.* Journal of power sources, 2014. **248**: p. 1000--1006.
35. Kim, K., et al., *Elucidating the Polymeric Binder Distribution within Lithium-Ion Battery Electrodes Using SAICAS.* Chemphyschem, 2018. **19**(13): p. 1627-1634.
36. Loeffler, N., et al., *Polyurethane Binder for Aqueous Processing of Li-Ion Battery Electrodes.* Journal of the Electrochemical Society, 2015. **162**(14): p. A2692-A2698.
37. Li, J., et al., *Water-Based Electrode Manufacturing and Direct Recycling of Lithium-Ion Battery Electrodes-A Green and Sustainable Manufacturing System.* iScience, 2020. **23**(5): p. 101081.
38. Sitarek, K. and J. Stetkiewicz, *Assessment of reproductive toxicity and gonadotoxic potential of N-methyl-2-pyrrolidone in male rats.* Int J Occup Med Environ Health, 2008. **21**(1): p. 73-80.
39. Sitarek, K., J. Stetkiewicz, and W. Wasowicz, *Evaluation of reproductive disorders in female rats exposed to N-methyl-2-pyrrolidone.* Birth Defects Res B Dev Reprod Toxicol, 2012. **95**(3): p. 195-201.
40. Gaines, L. and R. Cuenca, *Costs of lithium-ion batteries for vehicles*. 2000.
41. Li, J., et al., *From Materials to Cell: State-of-the-Art and Prospective Technologies for Lithium-Ion Battery Electrode Processing.* Chem Rev, 2022. **122**(1): p. 903-956.
42. Hawley, W.B. and J.L. Li, *Beneficial rheological properties of lithium-ion battery cathode slurries from elevated mixing and coating temperatures.* Journal of Energy Storage, 2019. **26**: p. 100994.
43. Kim, K.M., et al., *Effect of mixing sequences on the electrode characteristics of lithium-ion rechargeable batteries.* Journal of Power Sources, 1999. **83**(1-2): p. 108-113.
44. Liu, Z., V. Battaglia, and P.P. Mukherjee, *Mesoscale elucidation of the influence of mixing sequence in electrode processing.* Langmuir, 2014. **30**(50): p. 15102-13.
45. Diehm, R., et al., *High-Speed Coating of Primer Layer for Li-Ion Battery Electrodes by Using Slot-Die Coating.* Energy Technology, 2020. **8**(9): p. 2000259.
46. Creel, E.B., et al., *Slot-die-coating operability windows for polymer electrolyte membrane fuel cell cathode catalyst layers.* J Colloid Interface Sci, 2022. **610**: p. 474-485.
47. Loeffler, N., et al., *In situ coating of Li [Ni0. 33Mn0. 33Co0. 33] O2 particles to enable aqueous electrode processing.* ChemSusChem, 2016. **9**(10): p. 1112--1117.
48. Du, Z.J., et al., *Enabling aqueous processing for crack-free thick electrodes.* Journal of Power Sources, 2017. **354**: p. 200-206.

49. Dong, Q., et al., *Insights into the Dual Role of Lithium Difluoro (oxalato) borate Additive in Improving the Electrochemical Performance of NMC811|| Graphite Cells.* ACS Applied Energy Materials, 2019. **3**(1): p. 695-704.
50. Memm, M., A. Hoffmann, and M. Wohlfahrt-Mehrens, *Water-based LiNi1/3Mn1/3Co1/3O2-cathodes with good electrochemical performance by use of additives.* Electrochimica Acta, 2018. **260**: p. 664-673.
51. Wood III, D.L., et al., *Perspectives on the relationship between materials chemistry and roll-to-roll electrode manufacturing for high-energy lithium-ion batteries.* Energy Storage Materials, 2020. **29**: p. 254-265.
52. Schmitt, M., et al., *Slot-die processing of lithium-ion battery electrodes-Coating window characterization.* Chemical Engineering and Processing-Process Intensification, 2013. **68**: p. 32-37.
53. Lee, S.H., et al., *Operability coating windows and frequency response in slot coating flows from a viscocapillary model.* Chemical Engineering Science, 2011. **66**(21): p. 4653-4659.
54. Schweizer, P.M. and S. Kistler, *Liquid Film Coating: Scientific principles and their technological implications*. 2012: Springer Science & Business Media.
55. Sun, C., et al., *3D printing nanocomposite gel-based thick electrode enabling both high areal capacity and rate performance for lithium-ion battery.* Chemical Engineering Journal, 2020. **381**: p. 122641.
56. Pang, Y., et al., *Additive manufacturing of batteries.* Advanced Functional Materials, 2020. **30**(1): p. 1906244.
57. Gu, Y., et al., *Fabrication of rechargeable lithium ion batteries using water-based inkjet printed cathodes.* Journal of Manufacturing Processes, 2015. **20**: p. 198-205.
58. Larcher, D. and J.M. Tarascon, *Towards greener and more sustainable batteries for electrical energy storage.* Nat Chem, 2015. **7**(1): p. 19-29.
59. Susarla, N., S. Ahmed, and D.W. Dees, *Modeling and analysis of solvent removal during Li-ion battery electrode drying.* Journal of Power Sources, 2018. **378**: p. 660-670.
60. Bae, C.J., et al., *Design of battery electrodes with dual-scale porosity to minimize tortuosity and maximize performance.* Adv Mater, 2013. **25**(9): p. 1254-8.
61. Dai, Y. and V. Srinivasan, *On graded electrode porosity as a design tool for improving the energy density of batteries.* Journal of The Electrochemical Society, 2015. **163**(3): p. A406.
62. Liu, L., P.J. Guan, and C.H. Liu, *Experimental and Simulation Investigations of Porosity Graded Cathodes in Mitigating Battery Degradation of High Voltage Lithium-Ion Batteries.* Journal of the Electrochemical Society, 2017. **164**(13): p. A3163-A3173.
63. Parikh, D., T. Christensen, and J.L. Li, *Correlating the influence of porosity, tortuosity, and mass loading on the energy density of LiNi0.6Mn0.2Co0.2O2 cathodes under extreme fast charging (XFC) conditions.* Journal of Power Sources, 2020. **474**: p. 228601.

64. Rupnowski, P., et al., *In-line monitoring of Li-ion battery electrode porosity and areal loading using active thermal scanning - modeling and initial experiment.* Journal of Power Sources, 2018. **375**: p. 138-148.
65. Strmcnik, D., et al., *Electrocatalytic transformation of HF impurity to H-2 and LiF in lithium-ion batteries.* Nature Catalysis, 2018. **1**(4): p. 255-262.
66. Huang, X.S., *Separator technologies for lithium-ion batteries.* Journal of Solid State Electrochemistry, 2011. **15**(4): p. 649-662.
67. Mao, C.Y., et al., *Balancing formation time and electrochemical performance of high energy lithium-ion batteries.* Journal of Power Sources, 2018. **402**: p. 107-115.
68. An, S.J., et al., *Electrolyte Volume Effects on Electrochemical Performance and Solid Electrolyte Interphase in Si-Graphite/NMC Lithium-Ion Pouch Cells.* ACS Appl Mater Interfaces, 2017. **9**(22): p. 18799-18808.
69. An, S.J., et al., *The state of understanding of the lithium-ion-battery graphite solid electrolyte interphase (SEI) and its relationship to formation cycling.* Carbon, 2016. **105**: p. 52-76.
70. An, S.J., et al., *Correlation of Electrolyte Volume and Electrochemical Performance in Lithium-Ion Pouch Cells with Graphite Anodes and NMC532 Cathodes.* Journal of the Electrochemical Society, 2017. **164**(6): p. A1195-A1202.
71. Loeffler, N., et al., *Performance of LiNi1/3Mn1/3Co1/3O2/graphite batteries based on aqueous binder.* Journal of Power Sources, 2014. **248**: p. 915-922.
72. Li, J.L., et al., *Toward Low-Cost, High-Energy Density, and High-Power Density Lithium-Ion Batteries.* Jom, 2017. **69**(9): p. 1484-1496.
73. Bottino, A., et al., *Solubility Parameters of Poly(Vinylidene Fluoride).* Journal of Polymer Science Part B-Polymer Physics, 1988. **26**(4): p. 785-794.
74. Zou, F. and A. Manthiram, *A Review of the Design of Advanced Binders for High-Performance Batteries.* Advanced Energy Materials, 2020. **10**(45): p. 2002508.
75. Hays, K.A., et al., *What makes lithium substituted polyacrylic acid a better binder than polyacrylic acid for silicon-graphite composite anodes?* Journal of Power Sources, 2018. **384**: p. 136--144.
76. Wang, Y., et al., *Tailoring the Interplay between Ternary Composite Binder and Graphite Anodes toward High-Rate and Long-Life Li-Ion Batteries.* Electrochimica Acta, 2016. **191**: p. 70-80.
77. Hatzell, K.B., et al., *Challenges in Lithium Metal Anodes for Solid-State Batteries.* Acs Energy Letters, 2020. **5**(3): p. 922-934.
78. Wenzel, S., et al., *Direct Observation of the Interfacial Instability of the Fast Ionic Conductor Li10GeP2S12 at the Lithium Metal Anode.* Chemistry of Materials, 2016. **28**(7): p. 2400-2407.
79. Kotobuki, M., et al., *Fabrication of all-solid-state lithium battery with lithium metal anode using Al2O3-added Li7La3Zr2O12 solid electrolyte.* Journal of Power Sources, 2011. **196**(18): p. 7750-7754.
80. Wenzel, S., et al., *Interphase formation and degradation of charge transfer kinetics between a lithium metal anode and highly crystalline Li7P3S11 solid electrolyte.* Solid State Ionics, 2016. **286**: p. 24-33.

81. Xu, W., et al., *Lithium metal anodes for rechargeable batteries.* Energy & Environmental Science, 2014. **7**(2): p. 513-537.
82. Lin, D., Y. Liu, and Y. Cui, *Reviving the lithium metal anode for high-energy batteries.* Nat Nanotechnol, 2017. **12**(3): p. 194-206.
83. Cheng, X.B., et al., *Toward Safe Lithium Metal Anode in Rechargeable Batteries: A Review.* Chem Rev, 2017. **117**(15): p. 10403-10473.
84. Yoo, M., et al., *Effect of poly(vinylidene fluoride) binder crystallinity and graphite structure on the mechanical strength of the composite anode in a lithium ion battery.* Polymer, 2003. **44**(15): p. 4197-4204.
85. Kovalenko, I., et al., *A Major Constituent of Brown Algae for Use in High-Capacity Li-Ion Batteries.* Science, 2011. **334**(6052): p. 75-79.
86. Komaba, S., T. Ozeki, and K. Okushi, *Functional interface of polymer modified graphite anode.* Journal of Power Sources, 2009. **189**(1): p. 197-203.
87. Drofenik, J., et al., *Cellulose as a binding material in graphitic anodes for Li ion batteries: a performance and degradation study.* Electrochimica Acta, 2003. **48**(7): p. 883-889.
88. Li, J., et al., *Investigations on cellulose-based high voltage composite cathodes for lithium ion batteries.* Journal of Power Sources, 2011. **196**(18): p. 7687-7691.
89. Lee, J.H., et al., *Aqueous processing of natural graphite particulates for lithium-ion battery anode's and their electrochemical performance.* Journal of Power Sources, 2005. **147**(1-2): p. 249-255.
90. El Ouatani, L., et al., *Surface film formation on a carbonaceous electrode: Influence of the binder chemistry.* Journal of Power Sources, 2009. **189**(1): p. 72-80.
91. Yen, J.P., et al., *Enhanced High-Temperature Cycle-Life of Mesophase Graphite Anode with Styrene-Butadiene Rubber/Carboxymethyl Cellulose Binder.* Ecs Electrochemistry Letters, 2012. **1**(6): p. A80-A82.
92. Gordon, R., R. Orias, and N. Willenbacher, *Effect of carboxymethyl cellulose on the flow behavior of lithium-ion battery anode slurries and the electrical as well as mechanical properties of corresponding dry layers.* Journal of Materials Science, 2020. **55**(33): p. 15867-15881.
93. Notake, K., et al., *The application of a water-based hybrid polymer binder to a high-voltage and high-capacity Li-rich solid-solution cathode and its performance in Li-ion batteries.* Journal of Applied Electrochemistry, 2016. **46**(3): p. 267-278.
94. Wu, Q.L., et al., *Investigations on high energy lithium-ion batteries with aqueous binder.* Electrochimica Acta, 2013. **114**: p. 1-6.
95. Li, C.C. and Y.W. Wang, *Binder Distributions in Water-Based and Organic-Based LiCoO2 Electrode Sheets and Their Effects on Cell Performance.* Journal of the Electrochemical Society, 2011. **158**(12): p. A1361-A1370.
96. Baunach, M., et al., *Delamination behavior of lithium-ion battery anodes: Influence of drying temperature during electrode processing.* Drying Technology, 2016. **34**(4): p. 462-473.

97. Jaiser, S., et al., *Experimental investigation into battery electrode surfaces: The distribution of liquid at the surface and the emptying of pores during drying.* Journal of Colloid and Interface Science, 2017. **494**: p. 22-31.
98. Jaiser, S., et al., *Microstructure formation of lithium-ion battery electrodes during drying An - ex-situ study using cryogenic broad ion beam slope cutting and scanning electron microscopy (Cryo-BIB-SEM).* Journal of Power Sources, 2017. **345**: p. 97-107.
99. Jaiser, S., et al., *Investigation of film solidification and binder migration during drying of Li-Ion battery anodes.* Journal of Power Sources, 2016. **318**: p. 210-219.
100. Jaiser, S., et al., *Impact of drying conditions and wet film properties on adhesion and film solidification of lithium-ion battery anodes.* Drying Technology, 2017. **35**(15): p. 1807-1817.
101. Font, F., et al., *Binder migration during drying of lithium-ion battery electrodes: Modelling and comparison to experiment.* Journal of Power Sources, 2018. **393**: p. 177-185.
102. Stein IV, M., A. Mistry, and P.P. Mukherjee, *Mechanistic understanding of the role of evaporation in electrode processing.* Journal of The Electrochemical Society, 2017. **164**(7): p. A1616.
103. Cardinal, C.M., et al., *Drying Regime Maps for Particulate Coatings.* Aiche Journal, 2010. **56**(11): p. 2769-2780.
104. Forouzan, M.M., et al., *Experiment and simulation of the fabrication process of lithium-ion battery cathodes for determining microstructure and mechanical properties.* Journal of Power Sources, 2016. **312**: p. 172-183.
105. Zhu, M., J. Park, and A.M. Sastry, *Particle Interaction and Aggregation in Cathode Material of Li-Ion Batteries: A Numerical Study.* Journal of the Electrochemical Society, 2011. **158**(10): p. A1155-A1159.
106. Hagiwara, H., W.J. Suszynski, and L.F. Francis, *A Raman spectroscopic method to find binder distribution in electrodes during drying.* Journal of Coatings Technology and Research, 2014. **11**(1): p. 11-17.
107. Müller, M., et al., *Investigation of binder distribution in graphite anodes for lithium-ion batteries.* Journal of Power Sources, 2017. **340**: p. 1-5.
108. Church, B.C., D.T. Kaminski, and J.W. Jiang, *Corrosion of aluminum electrodes in aqueous slurries for lithium-ion batteries.* Journal of Materials Science, 2014. **49**(8): p. 3234-3241.
109. Li, S.Y. and B.C. Church, *Effect of aqueous-based cathode slurry pH and immersion time on corrosion of aluminum current collector in lithium-ion batteries.* Materials and Corrosion-Werkstoffe Und Korrosion, 2016. **67**(9): p. 978-987.
110. Xin, F., et al., *Li-Nb-O Coating/Substitution Enhances the Electrochemical Performance of the LiNi0.8Mn0.1Co0.1O2 (NMC 811) Cathode.* ACS Appl Mater Interfaces, 2019. **11**(38): p. 34889-34894.
111. Orlenius, J., et al., *Water based processing of LiFePO4/C cathode material for Li-ion batteries utilizing freeze granulation.* Journal of Power Sources, 2012. **213**: p. 119-127.

112. Bichon, M., et al., *Performance and ageing behavior of water-processed LiNi0.5Mn0.3Co0.2O2/Graphite lithium-ion cells.* Journal of Power Sources, 2021. **483**: p. 229097.
113. Dienwiebel, I., et al., *Enabling Aqueous Processing for LiNi0. 5Mn1. 5O4-Based Positive Electrodes in Lithium-Ion Batteries by Applying Lithium-Based Processing Additives.* Advanced Energy and Sustainability Research, 2021. **2**(11): p. 2100075.
114. Kuenzel, M., et al., *Complementary Strategies Toward the Aqueous Processing of High-Voltage LiNi0.5Mn1.5O4 Lithium-Ion Cathodes.* Chemsuschem, 2018. **11**(3): p. 562-573.
115. Jow, T.R., et al., *Factors Limiting Li+ Charge Transfer Kinetics in Li-Ion Batteries.* Journal of the Electrochemical Society, 2018. **165**(2): p. A361-A367.
116. Singh, K.B. and M.S. Tirumkudulu, *Cracking in drying colloidal films.* Phys Rev Lett, 2007. **98**(21): p. 218302.
117. Routh, A.F. and W.B. Russel, *A process model for latex film formation: Limiting regimes for individual driving forces.* Langmuir, 1999. **15**(22): p. 7762-7773.
118. Koos, E. and N. Willenbacher, *Capillary forces in suspension rheology.* Science, 2011. **331**(6019): p. 897-900.
119. Mayyas, A., D. Steward, and M. Mann, *The case for recycling: Overview and challenges in the material supply chain for automotive li-ion batteries.* Sustainable Materials and Technologies, 2019. **19**: p. e00087.
120. Zhang, X., et al., *Toward sustainable and systematic recycling of spent rechargeable batteries.* Chem Soc Rev, 2018. **47**(19): p. 7239-7302.
121. Sommerville, R., et al., *A review of physical processes used in the safe recycling of lithium ion batteries.* Sustainable Materials and Technologies, 2020. **25**: p. e00197.
122. Lv, W.G., et al., *A Critical Review and Analysis on the Recycling of Spent Lithium-Ion Batteries.* Acs Sustainable Chemistry & Engineering, 2018. **6**(2): p. 1504-1521.
123. Geller, B., T. Ohno, and C. Howell, *Comparative study of recycling lithium-ion and lead-acid batteries, A.* Colorado School of Mines. Arthur Lakes Library.
124. Gaines, L., *The future of automotive lithium-ion battery recycling: Charting a sustainable course.* Sustainable Materials and Technologies, 2014. **1**: p. 2-7.
125. Ellis, T.W. and A.H. Mirza, *Battery recycling: defining the market and identifying the technology required to keep high value materials in the economy and out of the waste dump*. 2014.
126. Ordoñez, J., E.J. Gago, and A. Girard, *Processes and technologies for the recycling and recovery of spent lithium-ion batteries.* Renewable and Sustainable Energy Reviews, 2016. **60**: p. 195-205.
127. Sonoc, A., J. Jeswiet, and V.K. Soo, *Opportunities to Improve Recycling of Automotive Lithium Ion Batteries.* 22nd Cirp Conference on Life Cycle Engineering, 2015. **29**: p. 752-757.
128. Kushnir, D., *lithium ion battery recycling technology 2015.* Current State and Future Prospects; ESAReport, 2015. **18**.

129. Tan, D.H.S., P.P. Xu, and Z. Chen, *Enabling sustainable critical materials for battery storage through efficient recycling and improved design: A perspective.* Mrs Energy & Sustainability, 2020. **7**.
130. Li, L., et al., *The Recycling of Spent Lithium-Ion Batteries: a Review of Current Processes and Technologies.* Electrochemical Energy Reviews, 2018. **1**(4): p. 461-482.
131. He, L.P., et al., *Recovery of cathode materials and Al from spent lithium-ion batteries by ultrasonic cleaning.* Waste Manag, 2015. **46**: p. 523-8.
132. Contestabile, M., S. Panero, and B. Scrosati, *A laboratory-scale lithium-ion battery recycling process.* Journal of Power Sources, 2001. **92**(1-2): p. 65-69.
133. Zeng, X. and J. Li, *Innovative application of ionic liquid to separate Al and cathode materials from spent high-power lithium-ion batteries.* J Hazard Mater, 2014. **271**: p. 50-6.
134. Fan, E., et al., *Sustainable Recycling Technology for Li-Ion Batteries and Beyond: Challenges and Future Prospects.* Chem Rev, 2020. **120**(14): p. 7020-7063.
135. Bai, Y.C., et al., *Energy and environmental aspects in recycling lithium-ion batteries: Concept of Battery Identity Global Passport.* Materials Today, 2020. **41**: p. 304-315.
136. Or, T., et al., *Recycling of mixed cathode lithium-ion batteries for electric vehicles: Current status and future outlook.* Carbon Energy, 2020. **2**(1): p. 6-43.
137. Yang, S., et al., *Determination of the chemical diffusion coefficient of lithium ions in spherical Li [Ni0. 5Mn0. 3Co0. 2] O2.* Electrochimica Acta, 2012. **66**: p. 88-93.
138. Weppner, W. and R. Huggins, *Electrochemical investigation of the chemical diffusion, partial ionic conductivities, and other kinetic parameters in Li3Sb and Li3Bi.* Journal of Solid State Chemistry, 1977. **22**(3): p. 297-308.
139. Mewis, J. and N.J. Wagner, *Colloidal suspension rheology*. 2012: Cambridge University Press.
140. Thommes, M., et al., *Physisorption of gases, with special reference to the evaluation of surface area and pore size distribution (IUPAC Technical Report).* Pure and Applied Chemistry, 2015. **87**(9-10): p. 1051-1069.
141. Li, J., et al., *Optimization of LiFePO4 nanoparticle suspensions with polyethyleneimine for aqueous processing.* Langmuir, 2012. **28**(8): p. 3783-90.
142. Tarascon, J.M. and M. Armand, *Issues and challenges facing rechargeable lithium batteries*, in *Materials for sustainable energy: a collection of peer-reviewed research and review articles from Nature Publishing Group*. 2011, World Scientific. p. 171--179.
143. Mao, C.Y., et al., *Identifying the limiting electrode in lithium ion batteries for extreme fast charging.* Electrochemistry Communications, 2018. **97**: p. 37-41.
144. Li, J., et al., *Lithium ion cell performance enhancement using aqueous LiFePO4 cathode dispersions and polyethyleneimine dispersant.* Journal of the Electrochemical Society, 2012. **160**(2): p. A201.

145. Li, J., et al., *Optimization of multicomponent aqueous suspensions of lithium iron phosphate (LiFePO4) nanoparticles and carbon black for lithium-ion battery cathodes.* J Colloid Interface Sci, 2013. **405**: p. 118-24.
146. Li, C.C., J.T. Lee, and X.W. Peng, *Improvements of dispersion homogeneity and cell performance of aqueous-processed LiCoO2 cathodes by using dispersant of PAA-NH4.* Journal of the Electrochemical Society, 2006. **153**(5): p. A809-A815.
147. Li, C.C., et al., *Using Poly(4-Styrene Sulfonic Acid) to Improve the Dispersion Homogeneity of Aqueous-Processed LiFePO4 Cathodes.* Journal of the Electrochemical Society, 2010. **157**(4): p. A517-A520.
148. Porcher, W., et al., *Optimizing the surfactant for the aqueous processing of LiFePO4 composite electrodes.* Journal of Power Sources, 2010. **195**(9): p. 2835-2843.
149. Lee, J.H., et al., *Effect of poly(acrylic acid) on adhesion strength and electrochemical performance of natural graphite negative electrode for lithium-ion batteries.* Journal of Power Sources, 2006. **161**(1): p. 612-616.
150. Hawley, W.B., et al., *Lithium and transition metal dissolution due to aqueous processing in lithium-ion battery cathode active materials.* Journal of Power Sources, 2020. **466**: p. 228315.
151. Kimura, K., et al., *Improvement of the Cyclability and Coulombic Efficiency of Li-Ion Batteries Using Li [Ni0. 8Co0. 15Al0. 05] O2 Cathode Containing an Aqueous Binder with Pressurized CO2 Gas Treatment.* Journal of The Electrochemical Society, 2018. **165**(2): p. A16--A20.
152. Li, C.-C., et al., *Effects of pH on the dispersion and cell performance of LiCoO 2 cathodes based on the aqueous process.* Journal of materials science, 2007. **42**(14): p. 5773--5777.
153. An, S.J., et al., *Design and Demonstration of Three-Electrode Pouch Cells for Lithium-Ion Batteries.* Journal of the Electrochemical Society, 2017. **164**(7): p. A1755-A1764.
154. Bauer, W. and D. Notzel, *Rheological properties and stability of NMP based cathode slurries for lithium ion batteries.* Ceramics International, 2014. **40**(3): p. 4591-4598.
155. Bitsch, B., et al., *A novel slurry concept for the fabrication of lithium-ion battery electrodes with beneficial properties.* Journal of Power Sources, 2014. **265**: p. 81-90.
156. Loeffler, N., et al., *In0.25emSitu Coating of Li[Ni0.33Mn0.33Co0.33]O2Particles to Enable Aqueous Electrode Processing.* ChemSusChem, 2016. **9**(10): p. 1112--1117.
157. Zhang, J.S., M. Klasky, and B.C. Letellier, *The aluminum chemistry and corrosion in alkaline solutions.* Journal of Nuclear Materials, 2009. **384**(2): p. 175-189.
158. Lu, W.Q., et al., *High-energy electrode investigation for plug-in hybrid electric vehicles.* Journal of Power Sources, 2011. **196**(3): p. 1537-1540.

159. Kalnaus, S., et al., *Design and processing for high performance Li ion battery electrodes with double-layer structure.* Journal of Energy Storage, 2021. **44**: p. 103582.
160. Du, Z., et al., *Understanding limiting factors in thick electrode performance as applied to high energy density Li-ion batteries.* Journal of Applied Electrochemistry, 2017. **47**(3): p. 405--415.
161. Yu, D.Y.W., et al., *Effect of Electrode Parameters on LiFePO[sub 4] Cathodes.* Journal of The Electrochemical Society, 2006. **153**(5): p. A835.
162. Golmon, S., K. Maute, and M.L. Dunn, *Multiscale design optimization of lithium ion batteries using adjoint sensitivity analysis.* International Journal for Numerical Methods in Engineering, 2012. **92**(5): p. 475-494.
163. Li, J., et al., *Toward Low-Cost, High-Energy Density, and High-Power Density Lithium-Ion Batteries.* JOM, 2017. **69**(9): p. 1484--1496.
164. Ogihara, N., et al., *Impedance Spectroscopy Characterization of Porous Electrodes under Different Electrode Thickness Using a Symmetric Cell for High-Performance Lithium-Ion Batteries.* Journal of Physical Chemistry C, 2015. **119**(9): p. 4612-4619.
165. Zheng, H.H., et al., *A comprehensive understanding of electrode thickness effects on the electrochemical performances of Li-ion battery cathodes.* Electrochimica Acta, 2012. **71**: p. 258-265.
166. Du, Z.J., et al., *Understanding limiting factors in thick electrode performance as applied to high energy density Li-ion batteries.* Journal of Applied Electrochemistry, 2017. **47**(3): p. 405-415.
167. Tran, H.Y., et al., *Influence of electrode preparation on the electrochemical performance of LiNi0.8Co0.15Al0.05O2 composite electrodes for lithium-ion batteries.* Journal of Power Sources, 2012. **210**: p. 276-285.
168. Tjaden, B., et al., *On the origin and application of the Bruggeman correlation for analysing transport phenomena in electrochemical systems.* Current Opinion in Chemical Engineering, 2016. **12**: p. 44-51.
169. Gallagher, K.G., et al., *Optimizing areal capacities through understanding the limitations of lithium-ion electrodes.* Journal of The Electrochemical Society, 2015. **163**(2): p. A138.
170. Appiah, W.A., et al., *Design optimization of LiNi0.6Co0.2Mn0.2O2/graphite lithium-ion cells based on simulation and experimental data.* Journal of Power Sources, 2016. **319**: p. 147-158.
171. Choi, J., et al., *Effect of LiCoO 2 cathode density and thickness on electrochemical performance of lithium-ion batteries.* Journal of Electrochemical Science and Technology, 2013. **4**(1): p. 27--33.
172. Albertus, P., J. Christensen, and J. Newman, *Experiments on and Modeling of Positive Electrodes with Multiple Active Materials for Lithium-Ion Batteries.* Journal of the Electrochemical Society, 2009. **156**(7): p. A606-A618.
173. Billaud, J., et al., *Magnetically aligned graphite electrodes for high-rate performance Li-ion batteries.* Nature Energy, 2016. **1**(8): p. 1--6.

174. Behr, S., et al. *Highly-structured, additive-free lithium-ion cathodes by freeze-casting technology*. in *Ceram. forum int*. 2015.
175. Huang, C., et al., *A two layer electrode structure for improved Li Ion diffusion and volumetric capacity in Li Ion batteries.* Nano Energy, 2017. **31**: p. 377-385.
176. Xue, L., et al., *Effect of particle size on rate capability and cyclic stability of LiNi0.5Mn1.5O4 cathode for high-voltage lithium ion battery.* Journal of Solid State Electrochemistry, 2014. **19**(2): p. 569--576.
177. Wood, M., et al., *Impact of secondary particle size and two-layer architectures on the high-rate performance of thick electrodes in lithium-ion battery pouch cells.* Journal of Power Sources, 2021. **515**.
178. Liu, C.F., Z.G. Neale, and G.Z. Cao, *Understanding electrochemical potentials of cathode materials in rechargeable batteries.* Materials Today, 2016. **19**(2): p. 109-123.
179. An, S.J., et al., *Correlation of electrolyte volume and electrochemical performance in lithium-ion pouch cells with graphite anodes and NMC532 cathodes.* Journal of The Electrochemical Society, 2017. **164**(6): p. A1195--A1202.
180. Weppner, W. and R.A. Huggins, *Determination of the kinetic parameters of mixed-conducting electrodes and application to the system Li3Sb.* Journal of The Electrochemical Society, 1977. **124**(10): p. 1569.
181. Ho, C., I. Raistrick, and R. Huggins, *Application of A-C techniques to the study of lithium diffusion in tungsten trioxide thin films.* Journal of the Electrochemical Society, 1980. **127**(2): p. 343.
182. Wang, Q., et al., *Determination of chemical diffusion coefficient of lithium ion in graphitized mesocarbon microbeads with potential relaxation technique.* Journal of the Electrochemical Society, 2001. **148**(7): p. A737-A741.
183. Kang, S.D. and W.C. Chueh, *Galvanostatic Intermittent Titration Technique Reinvented: Part I. A Critical Review.* Journal of the Electrochemical Society, 2021. **168**(12): p. 120504.
184. Aurbach, D., *Review of selected electrode-solution interactions which determine the performance of Li and Li ion batteries.* Journal of Power Sources, 2000. **89**(2): p. 206-218.
185. Chen, C.H., J. Liu, and K. Amine, *Symmetric cell approach and impedance spectroscopy of high power lithium-ion batteries.* Journal of Power Sources, 2001. **96**(2): p. 321-328.
186. Chen, C.H., J. Liu, and K. Amine, *Symmetric cell approach towards simplified study of cathode and anode behavior in lithium ion batteries.* Electrochemistry Communications, 2001. **3**(1): p. 44-47.
187. Ogihara, N., et al., *Theoretical and Experimental Analysis of Porous Electrodes for Lithium-Ion Batteries by Electrochemical Impedance Spectroscopy Using a Symmetric Cell.* Journal of the Electrochemical Society, 2012. **159**(7): p. A1034-A1039.

188. Ma, L., et al., *A systematic study on the reactivity of different grades of charged Li [NixMnyCoz] O2 with electrolyte at elevated temperatures using accelerating rate calorimetry.* Journal of Power Sources, 2016. **327**: p. 145-150.
189. Zhang, Y.S., et al., *A Review of Lithium-Ion Battery Electrode Drying: Mechanisms and Metrology.* Advanced Energy Materials, 2021: p. 2102233.
190. Lee, G.W., et al., *Effect of slurry preparation process on electrochemical performances of LiCoO2 composite electrode.* Journal of Power Sources, 2010. **195**(18): p. 6049-6054.
191. Hawley, W.B., H.M. Meyer, and J.L. Li, *Enabling aqueous processing for LiNi0.80Co0.15Al0.05O2 (NCA)-based lithium-ion battery cathodes using polyacrylic acid.* Electrochimica Acta, 2021. **380**: p. 138203.
192. Incropera, F.P., et al., *Fundamentals of heat and mass transfer*. Vol. 6. 1996: Wiley New York.
193. Neidhart, L., et al., *Aqueous Manufacturing of Defect-Free Thick Multi-Layer NMC811 Electrodes.* Nanomaterials (Basel), 2022. **12**(3): p. 317.
194. Heist, A. and S.H. Lee, *Improved Stability and Rate Capability of Ionic Liquid Electrolyte with High Concentration of LiFSI.* Journal of the Electrochemical Society, 2019. **166**(10): p. A1860-A1866.
195. Hu, Y.-S., *Batteries: getting solid.* Nature Energy, 2016. **1**(4): p. 1--2.
196. Takada, K., *Progress and prospective of solid-state lithium batteries.* Acta Materialia, 2013. **61**(3): p. 759-770.
197. Janek, J. and W.G. Zeier, *A solid future for battery development.* Nature Energy, 2016. **1**(400): p. 300.
198. Manthiram, A., X.W. Yu, and S.F. Wang, *Lithium battery chemistries enabled by solid-state electrolytes.* Nature Reviews Materials, 2017. **2**(4): p. 1--16.
199. Placke, T., et al., *Lithium ion, lithium metal, and alternative rechargeable battery technologies: the odyssey for high energy density.* Journal of Solid State Electrochemistry, 2017. **21**(7): p. 1939-1964.
200. Sakuda, A., A. Hayashi, and M. Tatsumisago, *Sulfide solid electrolyte with favorable mechanical property for all-solid-state lithium battery.* Sci Rep, 2013. **3**: p. 2261.
201. Fergus, J.W., *Ceramic and polymeric solid electrolytes for lithium-ion batteries.* Journal of Power Sources, 2010. **195**(15): p. 4554-4569.
202. Kamaya, N., et al., *A lithium superionic conductor.* Nat Mater, 2011. **10**(9): p. 682-6.
203. Schnell, J., et al., *All-solid-state lithium-ion and lithium metal batteries - paving the way to large-scale production.* Journal of Power Sources, 2018. **382**: p. 160-175.
204. Nagao, M., et al., *In situ SEM study of a lithium deposition and dissolution mechanism in a bulk-type solid-state cell with a Li 2 S--P 2 S 5 solid electrolyte.* Physical Chemistry Chemical Physics, 2013. **15**(42): p. 18600--18606.
205. Ren, Y.Y., et al., *Direct observation of lithium dendrites inside garnet-type lithium-ion solid electrolyte.* Electrochemistry Communications, 2015. **57**: p. 27-30.

206. Schnell, J., et al., *Solid versus Liquid---A Bottom-Up Calculation Model to Analyze the Manufacturing Cost of Future High-Energy Batteries.* Energy Technology, 2020: p. 1901237.
207. Hovington, P., et al., *New Lithium Metal Polymer Solid State Battery for an Ultrahigh Energy: Nano C-LiFePO4 versus Nano Li1.2V3O8.* Nano Letters, 2015. **15**(4): p. 2671-2678.
208. Baril, D., C. Michot, and M. Armand, *Electrochemistry of liquids vs. solids: Polymer electrolytes.* Solid State Ionics, 1997. **94**(1-4): p. 35-47.
209. Zhou, G.M., F. Li, and H.M. Cheng, *Progress in flexible lithium batteries and future prospects.* Energy & Environmental Science, 2014. **7**(4): p. 1307-1338.
210. Mizuno, F., et al., *New, highly ion-conductive crystals precipitated from Li2S-P2S5 glasses.* Advanced Materials, 2005. **17**(7): p. 918-+.
211. Armand, M., *Polymer Solid Electrolytes - an Overview.* Solid State Ionics, 1983. **9-10**(Dec): p. 745-754.
212. Murata, K., S. Izuchi, and Y. Yoshihisa, *An overview of the research and development of solid polymer electrolyte batteries.* Electrochimica Acta, 2000. **45**(8-9): p. 1501-1508.
213. Armand, M., *The History of Polymer Electrolytes.* Solid State Ionics, 1994. **69**(3-4): p. 309-319.
214. Chen, L., et al., *PEO/garnet composite electrolytes for solid-state lithium batteries: From "ceramic-in-polymer" to "polymer-in-ceramic".* Nano Energy, 2018. **46**: p. 176-184.
215. Kerman, K., et al., *Review-Practical Challenges Hindering the Development of Solid State Li Ion Batteries.* Journal of the Electrochemical Society, 2017. **164**(7): p. A1731-A1744.
216. Kim, J.G., et al., *A review of lithium and non-lithium based solid state batteries.* Journal of Power Sources, 2015. **282**: p. 299-322.
217. Li, Y., et al., *Hybrid Polymer/Garnet Electrolyte with a Small Interfacial Resistance for Lithium-Ion Batteries.* Angew Chem Int Ed Engl, 2017. **56**(3): p. 753-756.
218. Hanft, D., J. Exner, and R. Moos, *Thick-films of garnet-type lithium ion conductor prepared by the Aerosol Deposition Method: The role of morphology and annealing treatment on the ionic conductivity.* Journal of Power Sources, 2017. **361**: p. 61-69.
219. Troy, S., et al., *Life Cycle Assessment and resource analysis of all-solid-state batteries.* Applied Energy, 2016. **169**: p. 757-767.
220. Howell, D., *Vehicle Technologies Office Electrohemical Energy Storage R&D Overview.* 2017.
221. Ruther, R.E., et al., *Chemical Evolution in Silicon-Graphite Composite Anodes Investigated by Vibrational Spectroscopy.* ACS Appl Mater Interfaces, 2018. **10**(22): p. 18641-18649.
222. Feng, L.L., et al., *Low temperature synthesis and ion conductivity of Li7La3Zr2O12 garnets for solid state Li ion batteries.* Solid State Ionics, 2017. **310**: p. 129-133.

223. Murugan, R., V. Thangadurai, and W. Weppner, *Fast lithium ion conduction in garnet-type Li7La3Zr2O12.* Angewandte Chemie-International Edition, 2007. **46**(41): p. 7778-7781.
224. Shen, F.Y., et al., *Effect of Pore Connectivity on Li Dendrite Propagation within LLZO Electrolytes Observed with Synchrotron X-ray Tomography.* Acs Energy Letters, 2018. **3**(4): p. 1056-1061.
225. Xue, W., et al., *The effect of sintering process on lithium ionic conductivity of Li 6.4 Al 0.2 La 3 Zr 2 O 12 garnet produced by solid-state synthesis.* RSC Advances, 2018. **8**(24): p. 13083--13088.
226. Buschmann, H., et al., *Structure and dynamics of the fast lithium ion conductor ``Li 7 La 3 Zr 2 O 12''.* Physical Chemistry Chemical Physics, 2011. **13**(43): p. 19378--19392.
227. Awaka, J., et al., *Synthesis and structure analysis of tetragonal Li7La3Zr2O12 with the garnet-related type structure.* Journal of Solid State Chemistry, 2009. **182**(8): p. 2046-2052.
228. Geiger, C.A., et al., *Crystal Chemistry and Stability of "Li7La3Zr2O12" Garnet: A Fast Lithium-Ion Conductor.* Inorganic Chemistry, 2011. **50**(3): p. 1089-1097.
229. Kumazaki, S., et al., *High lithium ion conductive Li7La3Zr2O12 by inclusion of both Al and Si.* Electrochemistry Communications, 2011. **13**(5): p. 509-512.
230. Jin, Y. and P. McGinn, *Al-doped Li7La3Zr2O12 synthesized by a polymerized complex method.* Journal of Power Sources, 2011. **196**(20): p. 8683-8687.
231. Sharafi, A., et al., *Impact of air exposure and surface chemistry on Li--Li 7 La 3 Zr 2 O 12 interfacial resistance.* Journal of Materials Chemistry A, 2017. **5**(26): p. 13475--13487.
232. Jin, Y. and P.J. McGinn, *Li7La3Zr2O12 electrolyte stability in air and fabrication of a Li/Li7La3Zr2O12/Cu0.1V2O5 solid-state battery.* Journal of Power Sources, 2013. **239**: p. 326-331.
233. Langevin, S.A., et al., *UV-cured gel polymer electrolytes with improved stability for advanced aqueous Li-ion batteries.* Chem Commun (Camb), 2019. **55**(87): p. 13085-13088.
234. Seino, Y., et al., *A sulphide lithium super ion conductor is superior to liquid ion conductors for use in rechargeable batteries.* Energy & Environmental Science, 2014. **7**(2): p. 627-631.
235. Ohta, S., et al., *All-solid-state lithium ion battery using garnet-type oxide and Li3BO3 solid electrolytes fabricated by screen-printing.* Journal of Power Sources, 2013. **238**: p. 53-56.
236. Ohta, S., et al., *Electrochemical performance of an all-solid-state lithium ion battery with garnet-type oxide electrolyte.* Journal of Power Sources, 2012. **202**: p. 332-335.
237. Usui, H., et al., *Anode properties of thick-film electrodes prepared by gas deposition of Ni-coated Si particles.* Journal of Power Sources, 2011. **196**(4): p. 2143-2148.

238. Kato, T., et al., *Preparation of thick-film electrode-solid electrolyte composites on Li7La3Zr2O12 and their electrochemical properties.* Journal of Power Sources, 2016. **303**: p. 65--72.
239. Exner, J., P. Fuierer, and R. Moos, *Aerosol deposition of (Cu,Ti) substituted bismuth vanadate films.* Thin Solid Films, 2014. **573**: p. 185-190.
240. Akedo, J., *Aerosol deposition of ceramic thick films at room temperature: Densification mechanism of ceramic layers.* Journal of the American Ceramic Society, 2006. **89**(6): p. 1834-1839.
241. Sahner, K., M. Kaspar, and R. Moos, *Assessment of the novel aerosol deposition method for room temperature preparation of metal oxide gas sensor films.* Sensors and Actuators B-Chemical, 2009. **139**(2): p. 394-399.
242. Ahn, C.W., et al., *Microstructure and electrochemical properties of graphite and C-coated LiFePO4 films fabricated by aerosol deposition method for Li ion battery.* Carbon, 2015. **82**: p. 135-142.
243. Ahn, C.W., et al., *Microstructure and Ionic Conductivity in Li7La3Zr2O12 Film Prepared by Aerosol Deposition Method.* Journal of the Electrochemical Society, 2015. **162**(1): p. A60-A63.
244. Kim, I., et al., *Electrochemical properties of an as-deposited LiFePO4 thin film electrode prepared by aerosol deposition.* Journal of Power Sources, 2013. **244**: p. 646-651.
245. Popovici, D., et al., *Preparation of Lithium Aluminum Titanium Phosphate Electrolytes Thick Films by Aerosol Deposition Method.* Journal of the American Ceramic Society, 2011. **94**(11): p. 3847-3850.
246. Inada, R., et al., *Properties of aerosol deposited NASICON-type Li1.5Al0.5Ge1.5(PO4)(3) solid electrolyte thin films.* Ceramics International, 2015. **41**(9): p. 11136-11142.
247. Inada, R., et al., *Characterization of as-deposited Li4Ti5O12 thin film electrode prepared by aerosol deposition method.* Journal of Power Sources, 2014. **253**: p. 181-186.
248. Usui, H., Y. Kiri, and H. Sakaguchi, *Effect of carrier gas on anode performance of Si thick-film electrodes prepared by gas-deposition method.* Thin Solid Films, 2012. **520**(23): p. 7006-7010.
249. Ahn, C.W., et al., *Electrochemical properties of Li7La3Zr2O12-based solid state battery.* Journal of Power Sources, 2014. **272**: p. 554-558.
250. Iwasaki, S., et al., *Preparation of thick-film LiNi1/3Co1/3Mn1/3O2 electrodes by aerosol deposition and its application to all-solid-state batteries.* Journal of Power Sources, 2014. **272**: p. 1086-1090.
251. Scrosati, B., F. Croce, and L. Persi, *Impedance spectroscopy study of PEO-based nanocomposite polymer electrolytes.* Journal of The Electrochemical Society, 2000. **147**(5): p. 1718--1721.
252. Ha, H.J., et al., *UV-curable semi-interpenetrating polymer network-integrated, highly bendable plastic crystal composite electrolytes for shape-conformable all-solid-state lithium ion batteries.* Energy & Environmental Science, 2012. **5**(4): p. 6491-6499.

253. Saunders, C., et al., *Electron beam curing - taking good ideas to the manufacturing floor.* Radiation Physics and Chemistry, 2000. **57**(3-6): p. 441-445.
254. Du, Z., et al., *Electron Beam Curing of Composite Positive Electrode for Li-Ion Battery.* Journal of the Electrochemical Society, 2016. **163**(13): p. A2776-A2780.
255. Lee, P.M.a.S.-H., *Samsung to Recall 2.5 Million Galaxy Note 7s Over Battery Fires.* 2016.
256. Markoff, J., *Designing a Safer Battery for Smartphones (That Won't Catch Fire)*, in *The New York Times*. 2016.
257. Selyukh, A., *As Batteries Keep Catching Fire, U.S. Safety Agency Prepares For Change*, in *NPR*. 2016.
258. Joyce, C., *Powerful But Fragile: The Challenge Of Lithium Batteries*, in *NPR*. 2013.
259. Lisbona, D. and T. Snee, *A review of hazards associated with primary lithium and lithium-ion batteries.* Process Safety and Environmental Protection, 2011. **89**(6): p. 434-442.
260. Takada, K., N. Aotani, and S. Kondo, *Electrochemical Behaviors of Li+ Ion Conductor, Li3po4-Li2s-Sis2.* Journal of Power Sources, 1993. **43**(1-3): p. 135-141.
261. Caravati, E.M. and T.L. Litovitz, *Pediatric cyanide intoxication and death from an acetonitrile-containing cosmetic.* JAMA, 1988. **260**(23): p. 3470-3.
262. Wexler, P., et al., *Encyclopedia of toxicology*. Vol. 1. 2005: Academic Press.
263. Zhao, Y.R., et al., *A promising PEO/LAGP. hybrid electrolyte prepared by a simple method for all-solid-state lithium batteries.* Solid State Ionics, 2016. **295**: p. 65-71.
264. Pożyczka, K., et al., *Ionic conductivity and lithium transference number of poly (ethylene oxide): LiTFSI system.* Electrochimica Acta, 2017. **227**: p. 127-135.
265. Lux, S.F., et al., *LiTFSI Stability in Water and Its Possible Use in Aqueous Lithium-Ion Batteries: pH Dependency, Electrochemical Window and Temperature Stability.* Journal of the Electrochemical Society, 2013. **160**(10): p. A1694-A1700.
266. Foran, G., et al., *The Impact of Absorbed Solvent on the Performance of Solid Polymer Electrolytes for Use in Solid-State Lithium Batteries.* Iscience, 2020. **23**(10): p. 101597.
267. Pesko, D., *Complete Electrochemical Characterization of Ion Transport in Polymer Electrolytes*. 2018: University of California, Berkeley.
268. Moon, Y.I., et al., *Observation of the relaxation process in fluoroelastomers by dielectric relaxation spectroscopy.* Physica B-Condensed Matter, 2021. **608**: p. 412870.
269. Kremer, F. and A. Schönhals, *Broadband dielectric spectroscopy*. 2002: Springer Science & Business Media.
270. Pissis, P. and G. Polizos, *Molecular dynamics and ionic conductivity studies in polyurethane thermoplastic elastomers.* Handbook of condensation thermoplastic elastomers, 2005: p. 381-434.

271. Sengwa, R.J. and P. Dhatarwal, *Predominantly chain segmental relaxation dependent ionic conductivity of multiphase semicrystalline PVDF/PEO/LiClO4 solid polymer electrolytes.* Electrochimica Acta, 2020. **338**: p. 135890.
272. Choudhary, S. and R.J. Sengwa, *Effects of different inorganic nanoparticles on the structural, dielectric and ion transportation properties of polymers blend based nanocomposite solid polymer electrolytes.* Electrochimica Acta, 2017. **247**: p. 924-941.
273. Morsi, M.A., S.A. El-Khodary, and A. Rajeh, *Enhancement of the optical, thermal and electrical properties of PEO/PAM:Li polymer electrolyte films doped with Ag nanoparticles.* Physica B-Condensed Matter, 2018. **539**: p. 88-96.
274. Dhatarwal, P. and R.J. Sengwa, *Polymer Compositional Ratio-Dependent Morphology, Crystallinity, Dielectric Dispersion, Structural Dynamics, and Electrical Conductivity of PVDF/PEO Blend Films.* Macromolecular Research, 2019. **27**(10): p. 1009-1023.
275. Rathika, R., O. Padmaraj, and S.A. Suthanthiraraj, *Electrical conductivity and dielectric relaxation behaviour of PEO/PVdF-based solid polymer blend electrolytes for zinc battery applications.* Ionics, 2018. **24**(1): p. 243-255.
276. Ramesh, S. and C.W. Liew, *Dielectric and FTIR studies on blending of [xPMMA-(1-x)PVC] with LiTFSI.* Measurement, 2013. **46**(5): p. 1650-1656.
277. Pesko, D.M., et al., *Negative Transference Numbers in Poly(ethylene oxide)-Based Electrolytes.* Journal of the Electrochemical Society, 2017. **164**(11): p. E3569-E3575.
278. Volkov, A.S., et al., *Analysis of Experimental Results by the Havriliak-Negami Model in Dielectric Spectroscopy.* Optics and Spectroscopy, 2018. **124**(2): p. 202-205.
279. Havriliak, S. and S. Negami, *A Complex Plane Analysis of Alpha-Dispersions in Some Polymer Systems.* Journal of Polymer Science Part C-Polymer Symposium, 1966. **14**(14pc): p. 99-+.
280. Santos, S., A. Cedeño, and C. Gómez, *DC conductivity and dielectric response in amorphous polycarbonate of Bisphenol-A.* Polymer Engineering & Science, 1999. **39**(9): p. 1752-1756.
281. Jonscher, A.K., *Dielectric relaxation in solids.* Journal of Physics D-Applied Physics, 1999. **32**(14): p. R57-R70.
282. Jain, H. and S. Krishnaswami, *Composition dependence of frequency power law of ionic conductivity of glasses.* Solid State Ionics, 1998. **105**(1-4): p. 129-137.
283. Jonscher, A.K., *The 'universal' dielectric response.* nature, 1977. **267**(5613): p. 673-679.

# PUBLICATION LIST

***First Author:***

**Alexander Kukay**, Ritu Sahore, Anand Parejiya, W. Blake Hawley, Jianlin Li, David L. Wood, *Aqueous Ni-rich-cathode dispersions processed with phosphoric acid for lithium-ion batteries with ultra-thick electrodes*, Journal of Colloid and Interface Science, Volume 581, Part B, 2021, 635-643, DOI: 10.1016/j.jcis.2020.07.144.

**Alexander Kukay**, Ritu Sahore, Anand Parejiya, W. B. Hawley, Jianlin Li, and David Wood, III, *Corrosion Mitigation and Increased Discharge Capacity in Aqueous Processed Thick Cathodes Using Phosphoric Acid Additives*, ECSarXiv, May 5 2020, DOI: 10.1149/osf.io/jwymp.

**Alexander Kukay**, *Chromium Selenide Synthesis and Characterization* (2019), Theses and Dissertations, 2467

***Co-Author:***

W. Blake Hawley, Zhijia Du, **Alexander J. Kukay**, Nancy J. Dudney, Andrew S. Westover, Jianlin Li, *Deconvoluting sources of failure in lithium metal batteries containing NMC and PEO-based electrolytes*, Electrochimica Acta, November 25 2021, DOI: 10.1016/j.electacta.2021.139579.

Georgios Polizos, Jaswinder Sharma, Charl J. Jafta, Nitin Muralidharan, Gabriel M. Veith, Jong K. Keum, **Alexander Kukay**, Ritu Sahore, David L. Wood III, *Nanostructured ligament and fiber Al doped Li7La3Zr2O12 scaffolds to mediate cathode-electrolyte interface chemistry*, J. Power Sources, 513, 2021, DOI: https://doi.org/10.1016/j.jpowsour.2021.230551

Ritu Sahore, David L. Wood, **Alexander Kukay**, Kelsey M. Grady, Jianlin Li, and Ilias Belharouak, *Towards Understanding of Cracking during Drying of Thick Aqueous-Processed LiNi*0.8*Mn*0.1*Co*0.1*O*2 *Cathodes*, ACS Sustainable Chemistry & Engineering 2020 8 (8), 3162-3169, DOI: 10.1021/acssuschemeng.9b06363

Hyeonseok Lee, Nuri Oncel, Bo Liu, **Alexander Kukay**, Furkan Altincicek, Rajender S. Varma, Mohammadreza Shokouhimehr, and Mehdi Ostadhassan, *Structural Evolution of Organic Matter in Deep Shales by Spectroscopy (1H and 13C Nuclear Magnetic Resonance, X-ray Photoelectron Spectroscopy, and Fourier Transform Infrared) Analysis*, Energy & Fuels 2020 34 (3), 2807-2815, DOI: 10.1021/acs.energyfuels.9b03851

Kevin A. Hays, Rose E. Ruther, **Alexander J. Kukay**, Pengfei Cao, Tomonori Saito, David L Wood III, Jianlin Li, *What makes lithium substituted polyacrylic acid a better binder than polyacrylic acid for silicon-graphite composite anodes?,* J. Power Sources, 384 136-144 2018, DOI: 10.1016/j.jpowsour.2018.02.085

***In Preparation:***

**Alexander Kukay**, Kelsey Livingston, W. Blake Hawley, Charl Jafta, Mengya Li, Harry Meyer, David Wood III, Jianlin Li, *Structured Bi-Layer Aqueous Processed Ultra-Thick Electrodes for Lithium-Ion Batteries*

**Alexander Kukay**, Emily Bott, Anton Ievlev, Georgios Polyzos, Jianlin Li, *Mechanical and Electrochemical Implications of Drying Temperature on Lithium-Ion Battery Electrodes*

**Alexander Kukay**, Charl Jafta, Marm Dixit, Georgios Polyzos, Jianlin Li, *Benefits of Solvent Replacement in PEO Based Solid Polymer Electrolytes with LiTFSI*

**Alexander Kukay**, David Wood III, Jianlin Li, *Aqueous Processing in Lithium-Ion Battery Electrodes: A Review*

# VITA

Alexander J. Kukay was born in Green Bay, Wisconsin in 1995 to loving parents Patrick and Peggy Kukay. He completed his undergraduate studies at the University of Wisconsin-Eau Claire in Applied Physics in 2017. He then completed his degree of Master of Science in Physics at the University of North Dakota. Upon completion of this degree, he attended The University of Tennessee, Knoxville in The Bredesen Center for Interdisciplinary Research and Graduate Education. Under the direction of Dr. David L. Wood III and Dr. Jianlin Li, he joined the Energy Storage and Conversion Manufacturing group at Oak Ridge National Laboratory. Here he investigated improvements in manufacturing techniques with an emphasis on aqueous processing methods. Though this program he was able to utilize the equipment and expertise present at the Battery Manufacturing Facility at Oak Ridge National Laboratory to further his education and contribute to the state of the art of lithium-ion battery production.